The Thesis Committee for Albert Aquvannoa Limantono
Certifies that this is the approved version of the following thesis:

MODELING STRAIN DEMANDS IN LONGITUDINAL STEEL BARS OF CONCRETE COLUMNS

APPROVED BY
SUPERVISING COMMITTEE:

Supervisor: Wassim M. Ghannoum

Trevor D. Hrynyk

MODELING STRAIN DEMANDS IN LONGITUDINAL STEEL BARS OF CONCRETE COLUMNS

by

Albert Aquvannoa Limantono, B.S

Thesis

Presented to the Faculty of the Graduate School of

The University of Texas at Austin

in Partial Fulfillment

of the Requirements

for the Degree of

Master of Science in Engineering

The University of Texas at Austin

December 2016

Dedication

To my parents, my country Indonesia, and the Great Shepherd

Acknowledgements

I would like to express my sincerest and deepest gratitude to my advisor, Dr. Wassim Ghannoum. Since the day I first started working with him, he has provided continuous guidance, while always being patient and showing limitless support. While working with him I have seen myself grow in more than one perspective. His experience and knowledge of the field gave the shape to this thesis. Special thanks go to Dr. Trevor Hrynyk for taking his time to provide invaluable quality review and suggestions for the material.

This study was made possible from funding and assistance provided by the Charles Pankow Foundation, the Concrete Reinforcing Steel Institute, The American Concrete Institute's Foundation, Nucor Inc. Seattle, CMC, and MMFX steel. I thank them for always being cooperative and helpful. I also want to thank my beloved country, Indonesia and LPDP scholarship program for supporting me financially throughout my master degree in University of Texas at Austin.

There are countless of people, without them the successful completion of this project would have been impossible. I would like to thank the dedicated laboratory personnel of FSEL: Michelle Damvar, Deanna Mueller, Blake Stasney, David Braley, and Dennis Fillip. Drit Sokoli as PhD student in this project has guided me and has been a reliable colleague throughout the project – many of his work also included in this Thesis. Chase Slavin and Stephen Zhao have been continuous supports, but their dedication towards work made their contribution invaluable. William Shekarchi has been an irreplaceable mentor and always took time when Drit was unavailable in the laboratory. Andri Setiawan always took time for insightful discussion and for being a good friend supporting me mentally for completing this Thesis. Several students have assisted at different times in the fabrication and testing of the specimens, and I am grateful to each and every

of them: Laith Quntar, Colter Roskos, Nawaf Alotaibi, Gloriana Arrieta Martinez, Jongkwon Choi, Sean Donahue, Douglas Pudleiner, Alex Katz, Graham Hogsett, and Gabriel Polo.

Above all, I thank my parents, my brother and my sister gave me. Words cannot express my gratitude for their love, prayers and supports.

ABSTRACT

MODELING STRAIN DEMANDS IN LONGITUDINAL STEEL BARS OF CONCRETE COLUMNS

Albert Aquvannoa Limantono, M.S.E

The University of Texas at Austin, 2016

Supervisor: Wassim M. Ghannoum

Fracture of longitudinal bars, due to high-strain low-cycle fatigue, is a common failure mode in seismically detailed reinforced concrete columns. The issue has recently attracted increased scrutiny due the national push to introduce high-strength reinforcing bars with yield strengths exceeding 80 or 100 ksi in concrete construction. Recent tests on columns with high-strength reinforcement have indicated that high-strength bars can experience significantly larger strain demands than their lower strength counterparts, and therefore may be more susceptible to low-cycle fatigue failures. A computational model coupled with empirical relations are proposed to estimate the global deformation behavior of reinforced concrete columns and provide reliable estimates of the strain demands on longitudinal bars through the full range of expected inelastic deformations during seismic demands. The model was calibrated using data from experiments conducted on seven concrete columns reinforced with bars having yield strengths from 64 ksi to

106 ksi. The columns were pushed to large damage states and monitored using a high-resolution optical strain measurement system. The computational model consists of a distributed plasticity fiber-section element with five Gauss-Lobatto integration points, and is bounded by zero-length elastic shear and rotational springs that simulate shear and bar slip deformations, respectively. The fiber-section computational model was found to provide reliable strain estimates for longitudinal bars up to the initiation of cover spalling. Two equations are proposed, one to estimate the lateral drift at first spalling and the associated bar debonding, and the other to adjust longitudinal-bar strains obtained from the fiber-section element after bar debonding. Critical parameters that affect strain demands were found to be the reinforcement tensile to yield strength ratio, the maximum applied shear stress, the axial load, the reinforcement yield strength, and reinforcement bond demand.

TABLE OF CONTENTS

LIST OF TABLES

LIST OF FIGURES

1. INTRODUCTION AND RESEARCH MOTIVATION

1.1. Motivation

The increase in demand for higher grade reinforcing steel in seismic and non-seismic applications has risen in U.S and worldwide recently. This demand is driven by the desire to reduce material quantities and the need to reduce bar congestion, particularly in seismic designs. The reduction of quantities of reinforcing steel in turn delivers more economic and environmentally friendly buildings.

Recently, the reinforcing bar industry adopted a grade 80 steel that satisfies the ASTM A706 standard (ASTM A706/A706M-16, 2016). Several steel mills across the United States are capable of producing the grade 80 A706 steel making it available the construction industry. Steel grades higher than grade 80 and having relatively high ductility (>10% fracture strains) are just emerging in the construction industry. However, the steel industries are producing the high-strength steels with various mechanical properties. None of the higher steel grades higher are able to meet the benchmark mechanical properties of grade 60 A706 steel. The variant of each different higher steel grade are diverging from benchmark behavior in different ways. Currently, structural engineers and steel mills are trying to obtain the best balance between demands on bars and feasible properties for high-strength steel.

However, current code limits on the strength of reinforcing steel, combined with a lack of understanding of the effects of higher strength steel on the performance of concrete members, are hindering the progress in structural designs with high strength steel. The available code limits on strength of the reinforcing steel have been in the code for decades. The last code which offered the increasing steel yield strength limit from 40 ksi to 60 ksi happened in 1956, the ACI 318 building code (ACI 318 1956). In the 1970s, newer version of ACI 318 code (1971) included the

limit of 80 ksi to be used only for non-seismic systems. To this date, this limit remains at 80 ksi for non-seismic systems except for shear design, which has to be designed using a maximum yield strength of transverse reinforcement of 60 ksi. For seismic design, the limit currently remains at 60 ksi (ACI 318 2014). Grade 100 steel was recently allowed in the ACI building code but only for designing confinement reinforcement of concrete members.

Performance concerns of reinforced concrete members have maintained the code limits on the strength of reinforcing steel. The performance considerations span in a wide range of behavioral aspects. In general, the use of high-strength reinforcement reduces member stiffness and increases elastic deformations before the onset of yielding, as less steel is utilized compared with lower strength alternatives. An increase in steel strength in reinforcing bars is associated with an increase in the strain at yield, and often with a reduction in the fracture strain, the tensile to yield strength ratio (T/Y ratio), and the length and presence of the yield plateau. In general, for a given bar size, higher strength implies larger tensile and compressive forces. Larger tensile forces for the same bar size result in an increase in bond demands and the forces at bar hooks or heads. On the other hand, larger compressive forces for the same bar size can increase bar buckling susceptibility given the same lateral bracing which is provided by the stirrups and ties. The larger strain at yielding in higher-strength steel will cause larger strains at service loads and therefore increase the crack widths and deflections. Larger crack widths in return can lead to the weakening of the concrete shear-transfer mechanisms and lower shear strengths. Additionally, the lower ductility of high-strength steel may affect seismic design, member deformation capacity, as well as bar-bend performance. There is also evidence that the tensile to yield strength ratio affects the spread of plasticity in reinforced concrete members and low value of the ratio can produce higher strain concentrations in bars at cracks (Macchi et al., 1996, Aoyama, H, 2001). Strain concentrations in the longitudinal reinforcement in return can reduce member ductility and cause

premature bar fracture. Potentially larger strain demands on high-strength reinforcing bars (HRSB) coupled with the lower fracture strain of HSRB compared with regular strength grade 60 bars, have also raised concerns about their cyclic fatigue performance in concrete structures subjected to seismic demands. All of these concerns highlight the need for accurately modeling the behavior of concrete members reinforced with HSRB, particularly the strain demands on HSRB to accurately predict both their global deformations and cyclic life.

1.2. Objectives and Scope

The primary objective of this work was to develop an analytical model capable of estimating the global deformation behavior of reinforced concrete columns and providing reliable strain demands on longitudinal bars through the full range of expected inelastic deformations during seismic demands. The model was calibrated based on seven cyclic experimental tests conducted on columns pushed to large damage states and monitored using a high-resolution optical strain measurement system (Sokoli et al., 2014). Parameters extracted from those tests were examined for trends between strain demands on reinforcing bars and influential parameters. The proposed model utilizes a force-formulation fiber-section element to which a scaling relation is applied to correct steel fiber strains to match experimental results.

The research objective was supported by three series of experimental tests of concrete columns with total of seven columns. Series 1 was conducted by LeBorgne (2012) which focused on understanding of the fundamental changes in column behavior that accompany shear and axial failure. The columns in Series 1 were designed identically and reinforced with grade 60 ASTM A615 but loaded with different axial load (ASTM A615/A615M-16, 2016). Series 2 was conducted by Sokoli (2014) and focused on investigating the shear performance of columns reinforced with high-strength steel. Three columns were designed to impart large demands on the transverse

reinforcement and achieve the same flexural strength but were constructed using different reinforcing bar strengths; grade 60 ASTM A706 bars, grade 80 ASTM A706 bars and newly-developed grade 100 bars. The data for newly-developed grade 100 bars column from Series 2 was not included in this study because the column sustained bond failure. Four columns were tested in Series 3, which focused on the effects of the bar T/Y ratios and ultimate elongations on the plasticity spread and deformation capacity of concrete columns. Three tests in Series 3 were conducted with grade 100 longitudinal and transverse bars obtained from three steel manufacturers using the main three production techniques in the United States for HSRB. The fourth specimen was reinforced with the benchmark grade 60 A706 bars. Columns were designed to impart large tensile strains and a large number cycles on longitudinal bars.

1.3. Organization

Details of the work completed to meet the previously described objectives are presented in the following chapters. Chapter 2 provides relevant background information related to high strength reinforcing steel in concrete columns and strain demands on longitudinal reinforcement in concrete columns. Chapter 3 describes relevant experimental test results, particularly pertaining to global deformation and strain demands on longitudinal reinforcement. Chapter 4 describes the modeling strategy and calibration of the proposed relations. Chapter 5 summarizes the modeling procedure, research findings, and conclusions, along with recommendations for future research. In addition to the main body of this thesis, appendices providing additional data and details about the calculated mean bar strains, column global deformations, and regression analyses are attached.

2. BACKGROUND

2.1 High-Strength Steel Reinforcement

2.1.1 PRODUCTION METHODS

Earlier attempts at increasing the yield strength of reinforcing bars focused on increasing the carbon and manganese content in steel alloys. These methods can successfully increase the yield strength of steel bars but have the drawback of reducing the elongations at fracture. The four main methods of strengthening steel reinforcing bars that are currently used in the industry are: cold working, micro-alloying, quenching and tempering, and a proprietary combination of alloying and micro structure manipulation.

2.1.1.1 Cold Working

Cold working is the method used to strengthen metal by enforcing plastic deformation. The strengthening occurs due to additional dislocations and movements generated within the crystal structure of the material. When two or more of these internal dislocations meet, increased resistance to plastic deformations occurs, which contributes to the gain in strength. However, this method reduces the ductility of the material. Cold working also eliminates the yield plateau. This method may result in an increase in the yield strength, but it reduces both ductility and the ratio of tensile-to-yield (T/Y) strength. For these reasons, this method is not used in producing high-strength steel bars for seismic applications.

2.1.1.2 Micro-Alloying

Micro-alloying is the process of producing high-strength steel by adding small amounts of vanadium (V), titanium (Ti), or niobium (N) to form a “solid solution”. The micro-alloying method consists of two strengthening mechanisms: grain refinement and precipitation. Grain refinement strengthening occurs by producing a very fine grain size generated by pinning the planar defects

(grain boundaries) through thermos-mechanical processing (rolling). Furthermore, the pinning of planar defects causes the intermetallic carbides to be dispersed through the ferrite grains, which further raises the yield strength of the material. This mechanism is called precipitation strengthening.

Titanium micro-alloying contributes to precipitation strengthening. However, titanium has a strong tendency to combine with oxygen, sulfur, and nitrogen, which makes it difficult to control the strengthening effects. Niobium micro-alloying in reinforcement production requires a high degree of control on rolling temperatures, which makes it more challenging to use for high-strength reinforcement production.

Vanadium is a strong carbide former and vanadium carbides precipitates have the highest austenite solubility compared to niobium and titanium (Gladman, 1997). Adding vanadium increase yield strength due to grain size refinement and precipitation of carbides and nitrides. Precipitation of second phase particles within the grain's crystal lattices impedes the movement of dislocations throughout the grain. This process makes the resulting dislocations move around the precipitates or through them. Enhancing nitrogen in vanadium-contained bars increases the precipitation of particles, which produces higher yield strength. Furthermore, the advantage of vanadium-nitrogen micro-alloying as it eliminates the adverse effects of strain aging on properties of steel (Caifu, 2010; Erasmus and Pussegoda, 1978; Restrepo-Posada et al., 1994).

Alloyed bars, particularly those produced with Vanadium, have a relatively large T/Y ratio, on the order of 1.2 to 1.4 for grade 100 bars. However, at grade 100, the fracture elongation of alloyed bars currently ranges from 9 to 14% and can be lower than that of tempered and quenched bars.

2.1.1.3 Quenching and Tempering

Quenching produces high-strength bars from inexpensive carbon steel. This process consists of rapid cooling of the steel after it had been heated to the austenitic phase, which results in a hard and brittle material. The quenched steel is then allowed to reheat from its core heat, which modifies the microstructure and decreases the hardness while increasing the ductility of the material. This process is called tempering. As a result, quenched and tempered bars have a softer more ductile center and a harder brittle shell. Tempering and quenching typically produces large gains in yield strength but relatively modest gains in tensile strength. Therefore, the T/Y ratio of such bars can be relatively low and on the order of 1.10 to 1.15 for grade 100 bars. On the other hand, fracture elongation of tempered and quenched bars tends to be larger than that of micro-alloyed bars.

2.1.1.4 Proprietary Combination of Alloying and Micro Structure Manipulation

The proprietary combination of alloying and micro structure manipulation method has been patented by MMFX (MMFX Technologies Corporation, 2012). This process involves manipulating the microstructure of steel to obtain the desired mechanical properties and strength. The process generates bars with stress-stain relations that do not have a well-defined yield point, exhibit a relatively high T/Y ratio, but have relatively low fracture elongations. The MMFX steel bars satisfy the ASTM A1035 specifications (ASTM A1035/A1035M-16a, 2016). ACI 318-14 (2014) allows the use of A1035 grade 100 bars in confinement applications.

2.1.2 STRUCTURAL CONSIDERATION

2.1.2.1 Ductility and Plasticity Spread

Increasing the yield strength of steel often results in a loss of fracture elongation and ductility. The loss is more pronounced when techniques for achieving higher strengths rely on the addition of carbon to the chemistry. Replacing carbon and manganese with vanadium results in higher strengths being achieved and limits the reduction in fracture elongations.

In general, the use of high-strength reinforcement reduces member stiffness and increases elastic deformations before the onset of yielding, as less steel is utilized compared with lower strength alternatives. Moreover, the shape of a reinforcement's stress-strain curve influences the spread of plasticity within a plastic hinge region. The presence of a yield plateau, the ratio of tensile-to-yield strength, and the total elongation at fracture are all important properties that promote the spread of plasticity and maintain strength through large inelastic rotations (Macchi et al., 1996; Aoyama, 2001; Rautenberg, 2011; Rautenber et al.,2012, 2013; Sokoli and Ghannoum, 2016).

Ductility capacity is a major concern in seismic applications. The ultimate lateral drift, Δ_u, defines the ductility of a concrete member. Δ_u depends on the type of failure experience by a member (i.e., hoop fracture, bar buckling, bar fracture, etc). Typically, inelastic deformations are estimated through rotational deformations of idealized plastic hinges that are given a length (l_p^*) and ultimate curvature (Ψ_u^*) at which failure is considered to occur. Often, the behavior of plastic hinges is also idealized as a plastic hinge length with constant inelastic curvature over the plastic hinge length. Failure occurs when an associated limiting ultimate curvature is reached. Member drift capacity is then estimated by adding inelastic lateral drifts to elastic drifts (Δ_y) by integrating a constant curvature (difference between curvature at elastic limit and the ultimate curvature = $\Psi_u^* - \Psi_y$) over the specified plastic hinge length (l_p^*) (Eq. 2-1 for a cantilever member).

$$\Delta_u = \Delta_y + l_p^*(\Psi_u^* - \Psi_y)(l - \frac{l_p^*}{2}) \quad (2\text{-}1)$$

Several models have been proposed to estimate plastic hinge length and the associated ultimate curvature at failure (e.g., Corley, 1966; Qi and Moehle, 1991; Priestley et al., 1996; Mendis, 2001). Some models specify an ultimate concrete compressive strain from which an ultimate curvature can be calculated based on sectional analysis (e.g., Baker and Amarakone; 1965, Corley, 1966; Priestley et al., 1996). Later research introduced that plastic hinge length dependence of bond strength of reinforcement and concrete into the foundation not just from the strain penetration (Berry et al., 2008). However, none of these models associated the T/Y ratio of longitudinal bars to the plastic hinge length although several previous research concluded that the T/Y ratio influenced the plasticity spread and strain concentrations (Macchi et al., 1996; Aoyama, 2001; Rautenberg, 2011; Rautenber et al.,2012, 2013; Sokoli and Ghannoum, 2016). In addition, previous models have been calibrated with tests carried-out on concrete members reinforced mostly with conventional grade 60 bars. Therefore, it is uncertain if the general behavior remains the same or if the equation introduced in past plasticity models can be applied to members reinforced with high-strength steel that typically exhibits a relatively low T/Y ratio compared with grade 60 steel.

Relatively few tests have been carried out to assess plasticity spread in members reinforced with high-strength steel. Twenty-seven small-scale columns with two different reinforcing steel properties were tested cyclically in single curvature by Macchi et al. (1996). The first type of steel used, named A8, had a yield strength of 87 ksi, a T/Y ratio of 1.1, and a uniform elongation of 0.08. Uniform elongation is the strain at peak stress. The second type of steel used was Fe steel, with a yield strength of 86 ksi, a T/Y ratio of 1.4, and a uniform elongation of 0.11. Specimens with varying cross sections and longitudinal and transverse reinforcement amounts were tested under

three different loading protocols. Applied axial loads varied from 0 to 16% $A_g f'_c$ (where A_g = gross sectional area; f'_c = concrete compressive strength). In all cases, failure was observed due to longitudinal bar fracture. Specimens reinforced with A8 steel failed before completing the target loading protocols. In contrast, concrete columns reinforced with Fe steel failed past the loading protocols in all cases. The authors concluded that premature failure of columns reinforced with A8 steel was mainly attributed to strain concentrations in longitudinal reinforcement and limited plasticity spread. They found strain hardening, or the T/Y ratio, to have a larger effect on the overall behavior of the members than bar fracture elongation values.

Similar tests were reported by Aoyama (2001) on beams. Two different types of reinforcing steel were used in the study. The R90 steel had a relatively low T/Y ratio of 1.1 and the CR75 steel a higher T/Y ratio of 1.33. Conclusions of this study were similar to those delivered by Macchi et al.. Failure occurred at an earlier loading stage in the beams with the steel having a low T/Y ratio due to bar fracture. These failures were again attributed to strain concentrations. Bars fractured at a 5% lateral drift ratio, while reversing into tension. The authors concluded that a lower tensile to yield ratio results in a substantially larger bar strain for the same deflection.

Rautenberg (2011, 2012, 2013) reported tests on columns reinforced with steel satisfying ASTM A1035. The steel used had a yield strength around 120 ksi but no defined yield point, thus no yield plateau. These columns lost significant lateral-load capacity at a drift ratio of 4%. Rautenberg (2011) concluded that tests reinforced with high-strength steel without a yield plateau “have smaller drift capacities than columns reinforced with A706 60-ksi steel reinforcement with a yield plateau”. The difference in drift capacity is attributed to the difference in the shape of the stress-strain curves, which leads to differences in the distribution of curvature”. Additional comparative tests were reported in 2013 (Rautenberg et al., 2012, 2013). The type of high-strength steel used

in this study was again A1035 for the longitudinal reinforcement. It was found that a decrease in drift capacity of 10-50% occurred when A1035 grade 100 or 120 reinforcement was used compared with when A706 grade 60 steel was used.

Tavallali et al. (2014) concluded from beam tests using SAS 670 longitudinal bars: “Replacing conventional grade 60 longitudinal steel bars with reduced amounts of grade 97 high-strength steel bars provided nearly identical flexural strength and did not decrease the usable deformation capacity.”

In conclusion, the available experimental data have demonstrated that reinforcing steel bars with higher values of the T/Y ratio are preferred in seismic applications. Longitudinal bars with a relatively high T/Y ratio allow plasticity to spread farther in regions of yielding, which in turn reduces significantly the elongation demands on bars. The presence of a yield plateau remains a significant issue as some research shows that its absence could result in decreasing drift capacity. Data is mixed on whether higher strength reinforcement reduces or maintains ductility capacity of concrete flexural members compared with grade 60 A706 steel.

2.2 Longitudinal Bar Strain Demands

2.2.1 CONCRETE COLUMN

Recent reversed cyclic tests were conducted on three columns designed with the same flexural strength but with different grades of reinforcing bars (grade 60, grade 80 and grade 100) (Sokoli and Ghannoum, 2016). Except for the bar strength, all other parameters were kept nominally identical for all columns. Those columns demonstrated different strain demands in the longitudinal bars at the same drift level. Grade 80 longitudinal bars sustained about 65% larger strains at all drift levels than those of the grade 60 longitudinal bars. The column reinforced with grade 100 bars sustained bond splitting failure. However, maximum strains in the grade 100

longitudinal bars were found to be 25% higher than in grade 80 bars and 100% higher than in the grade 60 bars at a given drift level prior to bond degradation.

2.2.2 LOW-CYCLE FATIGUE

Brown and Kunnath (2004) performed low-cycle fatigue test on typical longitudinal-bar sizes; #6, #7, #8, and #9. All the bar tested satisfied ASTM A615 grade 60 specifications. All bars were cycled at constant strain amplitudes varying between 1.5% to 3.0%. The strains were measured over the full lengths of the coupons which was selected as 6 times the bar –diameter (d_b). The strain amplitudes measured were based on the average strains across the entire clear length. The test concluded that the number of half cycles to failure of the reinforcing bars decreases exponentially as the strain amplitude increased (Figure 2.1a). The bars of larger diameters also appeared prone to failure at fewer half cycles than smaller bars.

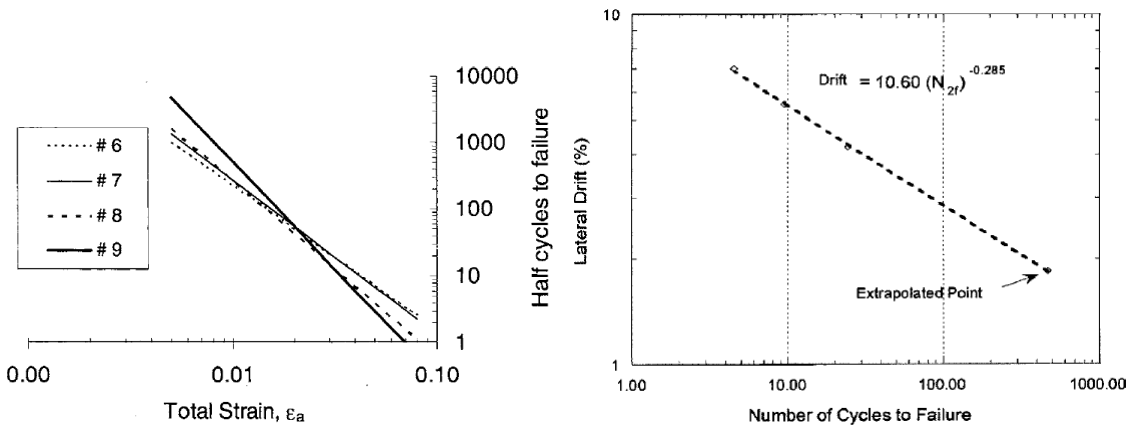

(a) (b)

Figure 2.1 Number of cycles to failure with:
(a) total strain (Kunnath et al., 2004); (b) lateral drift ratio (Kunnath et al., 1999)

Previous research on cumulative seismic damage of circular bridge columns (Kunnath et al., 1999) also focused on fatigue life of the columns. Four quarter-scale circular columns were tested in constant drift cycles of 2%, 4%, 5.5%, and 7% lateral drift ratio respectively until failure. The test

results demonstrated that the number of half cycles to failure decreased exponentially as in Figure 2.1b.

Recent tests on low-cycle fatigue tests for newly developed high-strength reinforcing bars were conducted by Slavin and Ghannoum, 2015. The reinforcing bars tested were classified as grade 60 ASTM A706, grade 80 ASTM A706, grade 80 ASTM A615, and grade 100 (without specification). The test also concluded similar result to previous research (Kunnath, 2004) that half-cycles to failure decreases exponentially as the total strain range increasing. Equations for assessing the fatigue of bars given a strain were proposed (Eq. 2-2 and 2-3 and Table 2-1). The "a", "b", "c", "d" parameters are summarized in Table 2-1 for #8 reinforcing bars of varying grades, specifications, and clear-span gripping lengths. Comparison of bar testing results for grade 60 #8 bars to previous research by Brown and Kunnath (2004) was also demonstrated in the sample plot in Figure 2.2. Slavin and Ghannoum (2015) concluded that the fatigue performance, defined in terms of the number of half-cycles to failure and the total strain energy dissipation, was marginally poorer for HSRB than for grade 60 bars. However, high variability of fatigue performance was observed for HSRB, some fractured at significantly fewer numbers of half-cycles than their grade 60 counterparts and some fractured at much higher numbers. Overall from the tests performed by Slavin and Ghannoum (2015), the average number of half-cycles to failure of the grade 100 bars was 91% of that for the grade 60 A706 bars.

$$Total\ Strain\ Range = a * (Half\text{–}Cycles\ to\ Failure)_b \quad (2\text{-}2)$$

$$Half\text{–}Cycles\ to\ Failure = c * (Total\ Strain\ Range)_d \quad (2\text{-}3)$$

Table 2-1 Summary of material coefficients for fatigue life equations for #8 bars (Slavin and Ghannoum, 2015)

Manufacturer	Grade	Clear Span	c	d
1	60	4db	5.14E-03	-2.87
		5db	5.92E-03	-2.77
		6db	7.92E-03	-2.59
	80	4db	2.48E-03	-2.97
		6db	6.60E-03	-2.43
	100	4db	2.40E-05	-4.62
		5db	8.14E-05	-4.06
		6db	1.49E-04	-3.77
2	60	4db	3.59E-04	-3.75
		5db	8.49E-04	-3.31
		6db	1.49E-03	-3.03
	100	4db	1.90E-06	-5.42
		5db	2.60E-06	-5.25
		6db	1.65E-05	-4.46

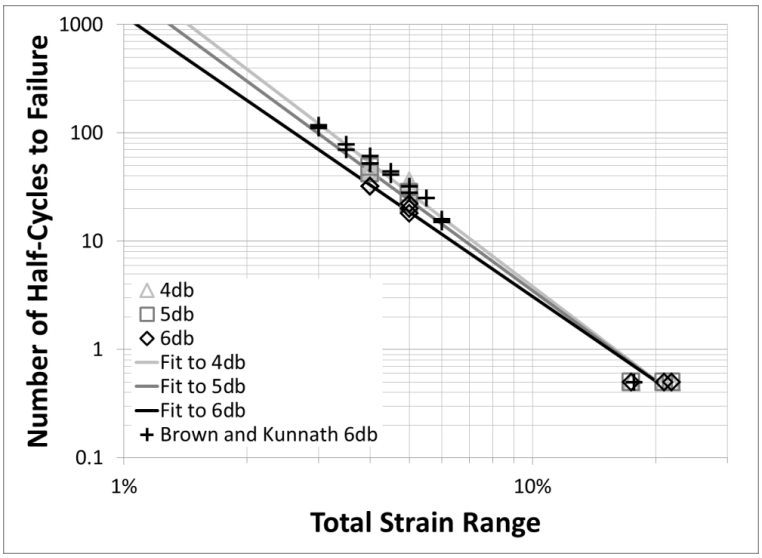

Figure 2.2 Results from Brown and Kunnath (2004) overlaid with data from grade 60 #8 bars produced by Manufacturer 1 (Slavin and Ghannoum, 2015)

2.2.3 DEBONDING OF LONGITUDINAL REINFORCEMENT

Previous research (Berry and Eberhard, 2007) attempted to predict average strains in longitudinal bars of circular bridge columns within a distance of D/2 from column base (0-D/2) and between

D/2 and D from column base (D/2-D) (Figure 2.3); with D being the column section diameter. Berry and Eberhard (2007) stated that their model accurately predicted the strains at low levels of column deformation, but was less accurate at the higher levels as shown in Figure 2.3. It is also stated that the discrepancy was likely caused by debonding of the longitudinal reinforcement up the height of the column. It is shown that the strain at D/2-D increased rapidly while the strain at 0-D/2 dipped below the calculated values and begin approaching the strains at D/2-D after the onset of spalling. Berry and Eberhard (2007) concluded that after the spalling and debonding of the longitudinal reinforcement occurred, the strains tended to spread along column height rather than concentrated in the highest moment section.

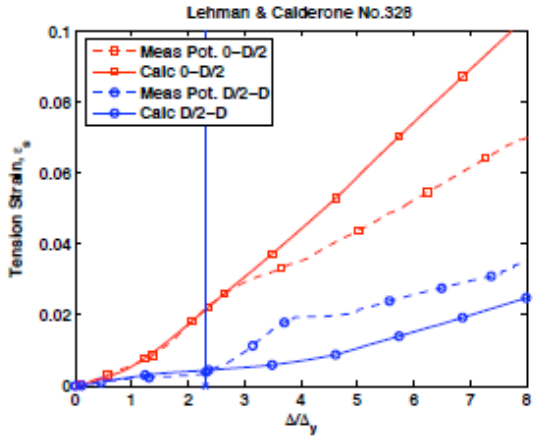

Figure 2.3 Debonding of longitudinal reinforcement effect on strain in longitudinal bars (Berry and Eberhard, 2007)

2.2.4 TENSION SHIFT DUE TO SHEAR/INCLINED CRACKS

Shear stresses leading to inclined cracking have been demonstrated to shift the location of maximum tension force in longitudinal bars away from the point of peak flexural demand. Park and Paulay (1975) explained that shear/inclined crack near the end region of concrete member could potentially spread the yielding of longitudinal bar over considerable length of the member. When the flexural reinforcement has yielded, shear/inclined cracks increase in width and less

shear can be transferred by aggregate interlock and dowel action. As a result, a larger portion of the shear force will have to be transferred across the compression zone. The idealized situation appears in Figure 2.4a. Each of the radiating cracks with minimum slope of 1:1.5 may be assumed to form the boundary of an inclined strut (Figure 2.4b). Park and Paulay (1975) made the assumption that the total shear force is transferred across the compression zone between the last stirrup and the highest moment section. From the equilibrium of Figure 2.4b, the tension force (T_x) was calculated and plotted in Figure 2.4c depending on the value of η (V_s/V_u). These findings were corroborated experimentally with strain gauge readings (Wight, 2016). Therefore, large shear forces can potentially shift the maximum tension force further from the end of a column, which possibly can lead to less strain concentrations at the highest moment section.

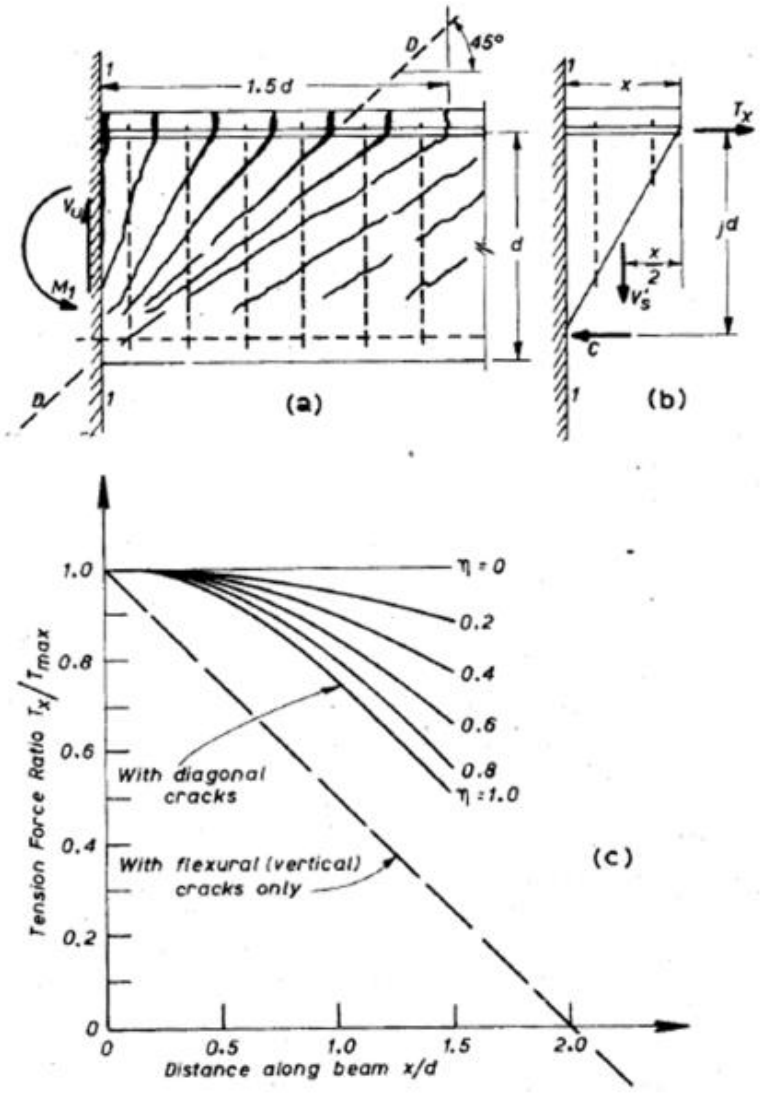

Figure 2.4 The distribution of steel forces at end region of the member affected by shear (Park and Paulay, 1975)

3 EXPERIMENTAL RESULTS

3.1 Introduction

The proposed analytical model for strain demands presented in Chapter 4 was supported by three series of experimental tests of concrete columns with total of nine columns tested in three series (LeBorgne, 2012; Sokoli and Ghannoum, 2016). Two of these nine tests were excluded in the calibration of the bar strain relations in Chapter 4, as one failed by bond and the other behaved differently due to the lack of clearly definable yield point in its bars. In Chapter 3, relevant details of the column tests are presented. Experimental results beyond what was reported in the original publications about the columns tests are also presented as they pertain to strain demands on longitudinal bars.

3.2 Column Tests

The nine columns were tested in three series in double curvature with no splices and axial loads were maintained constant during the tests. Series 1 columns were designed and detailed identically to yield in flexure prior to sustaining shear and axial failures, but were tested under different axial loads (LeBorgne, 2102). Two columns were tested in Series 1. The column with low axial load level (2L06) was designed to have longitudinal reinforcement bar yielding at flexural capacity (tension controlled) and the column with high axial load (2H06) was designed to have concrete crushing at flexural capacity (compression controlled). Both columns were reinforced with grade 60 ASTM A615 longitudinal and transverse.

Series 2 columns were design to have almost identical flexural strength and associated shear demands but had different yield strength for reinforcement bars (Sokoli and Ghannoum, 2016). Three columns were tested in Series 2. Column CS60 was reinforced with grade 60 ASTM A706

bars, column CS80 was reinforced with grade 80 ASTM A706 bars and column CS100 was reinforced with grade 100 bars that did not have ASTM specifications at the time of testing. Column CS100 sustained a bond failure mechanism, which is not beneficial for the purpose of evaluating strain demands on longitudinal bars and excluded for the rest of this thesis. The columns satisfied most ACI 318-14 provisions for Special Moment Frames except for the following. The imposed shear stresses were around 10 $\sqrt{f'c}$ (in psi units; 0.83 $\sqrt{f'c}$ in MPa units); where $f'c$ is concrete compressive strength. In addition, column CS60 and column CS80 hoop spacing exceeded by one inch the maximum allowed spacing of 4.5 inch in ACI 318-14 for confinement of plastic hinge regions in Special Moment Frames.

Series 3 columns were designed to impart large demands on longitudinal reinforcement, while having relatively low shear stresses on the order of 4.0 $\sqrt{f'c}$ (in psi units) for specimens with grade 100 reinforcement. These columns were purposely designed with low shear stresses to reduce the effect of tension shift and potentially increase strain concentrations in the longitudinal bars (Park and Paulay, 1975). Four columns were tested in Series 3 and were considered to be 2/3 the scale of prototype columns. Three of them were reinforced with grade 100 steel and one was reinforced with grade 60 steel. All columns were designed with the same bar sizes, bar detailing, and were geometrically identical. All four columns were designed per ACI 318 for seismic requirements except for the hook lengths of grade 100 transverse reinforcement were designed as specification of grade 60 steel. All three columns reinforced with grade 100 steel therefore had almost identical flexural capacity and associated shear demands. The column reinforced with grade 60 steel had lower flexural strength and associated shear stress. Columns reinforced with grade 100 steel were differentiate by the steel manufacturing process, which led to the difference in maximum tensile strength of the steel or tensile to yield strength ratio (T/Y ratio) of the bar being the main variable. Column CH100 was reinforced with grade 100 bars with a relatively high

(H) T/Y ratio, and was produced using the micro-alloying process. Column CL100 was reinforced with grade 100 bars with a relatively low (L) T/Y ratio, and was produced using the quenching and tempering process. Column CM100 was reinforced with grade 100 A1035 bars and was produced using the MMFX (M) proprietary process. Column CH60 was reinforced with grade 60 A706 bars with a relatively high (H) T/Y ratio.

3.2.1 SPECIMEN DETAILS

Column specimens for the three series are summarized in Table 3-1, which includes the cross-section view and clear height for each column, and in Table 3-2 which includes longitudinal bar sizes, transverse bar sizes, and transverse bar center to center spacing information. All columns framed into top and bottom footings (Figure 3.1), which were required to simulate the fixed restraint at both ends of the column and provide required anchorage lengths.

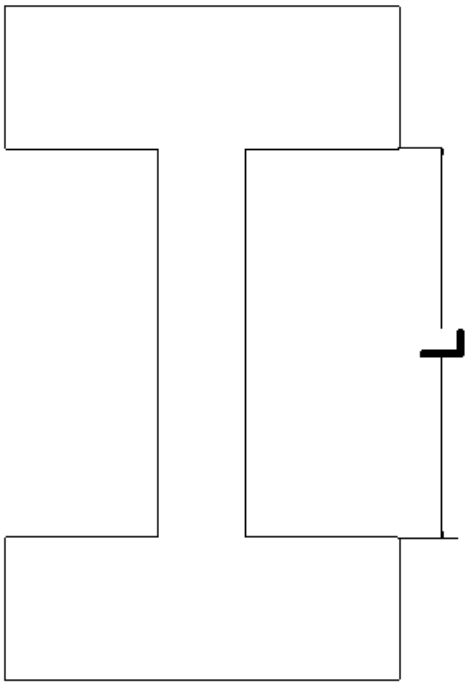

Figure 3.1 Column geometry

Table 3-1 Specimen details summary

Specimen	Cross-Section	Clear Height (L) (inch)
2L06	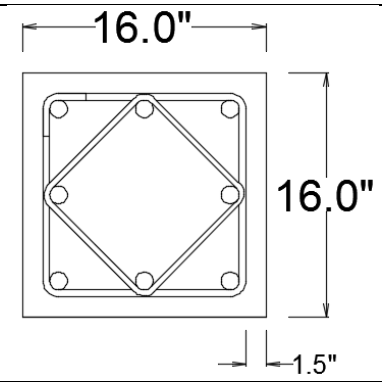	116
2H06		
CS60	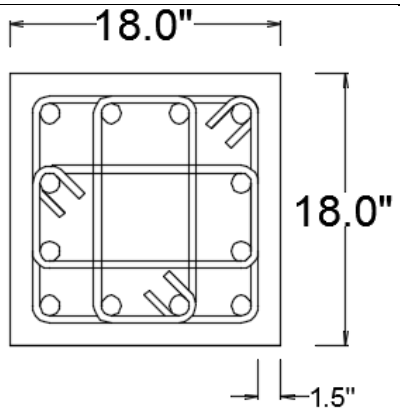	84
CS80		
CL100	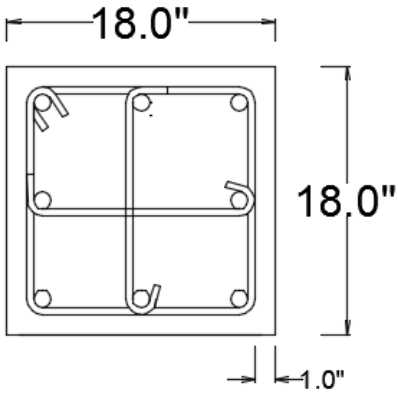	108
CH100		
CM100		
CH60		

Table 3-2 Specimen reinforcement summary

Specimen	Longitudinal Reinforcement	Transverse Reinforcement (center to center spacing)
2L06	#8 ρ_L = 2.5%	#3 @6in. (6 d_b)
2H06		
CS60	#10 ρ_L = 4.7%	#5 @5.5in. (4.4 d_b)
CS80	#9 ρ_L = 3.7%	#4 @5.5in. (4.9 d_b)
CL100	#6 ρ_L = 1.1%	#4 @3.5in. (4.7 d_b)
CH100		
CM100		
CH60	#6 ρ_L = 1.1%	#4 @4.5in. (6 d_b)

Note: d_b is the nominal bar diameter

The detailed discussion of this experimental research can be found elsewhere (LeBorgne, 2012; Sokoli and Ghannoum, 2016; and Sokoli, 2014).

3.2.2 MATERIAL PROPERTIES

Concrete strength was measured at the day of the column testing using three cylinders per ASTM C39 (ASTM C39/C39M-16a, 2016). Reinforcing bar steel coupons were taken from the same batch as the steel used in each specimen. Three steel coupons per bar type and grade were tested monotonically in tension to fracture as per ASTM A370 (ASTM 370-16, 2016). Uniform elongation of the steel was measured according to ASTM E8 (ASTM E8/E8-15a, 2015). Table 3-3 summarizes the concrete strength for all the columns and Table 3-4 summarizes the steel material properties.

Table 3-3 Concrete material properties

Specimen	Concrete Strength (ksi)
2L06	3.13
2H06	3.34
CS60	3.83
CS80	4.29
CL100	5.11
CH100	5.21
CM100	5.58
CH60	4.57

Table 3-4 Steel material properties

Specimen	Bar Size	Yield Strength (ksi)*	Tensile Strength (ksi)	Tensile to Yield Strength (T/Y) Ratio	Yield Strain (ε_y) ****	Fracture Elongation (%)	Uniform Elongation (%)
2L06** 2H06**	#8	65.5	107.2	1.63	0.0022	14	N/A
	#3	66.6	101.8	1.52	0.0023	14	N/A
CS60	#10	67.3	94.9	1.41	0.0022	18.3	10.1
	#5	68.5	95.8	1.40	0.0022	14.4	9.9
CS80	#9	79.1	106.5	1.34	0.0025	15.5	8.8
	#4	83.7	111.4	1.33	0.0030	12.1	8.9
CL100	#6	106	123	1.16	0.0036	12.8	8.6
	#4	85	100	1.18	0.0032	11.5	8.0
CH100	#6	100	127	1.27	0.0031	11.5	7.6
	#4	101	123	1.21	0.0035	12.8	9.0
CM100***	#6	124	157	1.27	N/A	9.8	4.9
	#4	141	171	1.22	N/A	8.6	4.7
CH60	#6	64.4	93.3	1.45	0.0022	17.6	11.8
	#4	N/A	N/A	N/A	N/A	N/A	N/A

**yield strength was defined by 0.002 offset method or the start of yield plateau*
***values from mill test report with gauge length of 8 in.*
****no yield plateau*
*****yield strength divided by modulus elasticity of steel of 29000 ksi*

3.2.3 TEST SETUP AND LOADING

A picture taken during one of the tests illustrates a specimen in the test setup in Figure 3.2. The specimens were tested under symmetric double curvature with fixed rotation boundary condition at the top and bottom. Specimens were post-tensioned to the strong floor using post-tensioned steel rods. The steel test frame was connected to the specimens through the top footings using post-tensioned steel rods.

Figure 3.2 Test setup

All specimens were tested under displacement controlled quasi-static reversed cyclic loading and compressive axial loads were maintained during the test with three hydraulic actuators. However, the axial loads were different for every column and are summarized in Table 3-5. The prescribed

lateral loading protocols differed between the series. The Series 1 loading protocol was based on the yield displacement of the high axial load column (2H06). The yield displacement was estimated analytically to be 0.81 inches. The loading scheme of Series 2 and 3 was based on the drift ratio of the columns as per FEMA 461 recommendations. Both loading protocols are presented in Table 3-6 and Table 3-7.

Table 3-5 Specimen compressive axial load

Specimen	Axial Load (kip)	Axial Load Ratio*
2L06	150	0.19
2H06	350	0.41
CS60	370	0.3
CS80	370	0.27
CL100	252	0.15
CH100	252	0.15
CM100	252	0.15
CH60	252	0.15

*Axial load divided by A_g f'_c (where f'_c = concrete compressive strength at the day of testing; A_g = gross-sectional area)

Table 3-6 Series 1 loading scheme

Three fully reversed cycles per drift level	
Load Stage	**Drift Ratio**
1	0.10%
2	0.20%
3	0.41%
4	0.81%
5	1.62%
6	3.24%
7	6.48%

Table 3-7 Series 2 and 3 loading scheme

Two fully reversed cycles per drift level	
Load Stage	**Drift Ratio**
1	0.20%
2	0.30%
3	0.40%
4	0.60%
5	0.80%
6	1.00%
7	1.50%
8	2.00%
9	3.00%
10	4.00%
11	5.50%
12	7.00%

3.2.4 INSTRUMENTATION

Columns were instrumented to measure the applied loads, deformations of the specimens, strains and crack widths on the concrete surface, and strains in the longitudinal reinforcing bars. In addition, Series 2 columns (CS60 and CS80) and two columns from Series 3 (CH100 and CL100) were instrumented to measure strains on the transverse reinforcing bars. Actuator load cells were used to measure the applied load. An optical measurement system was used to measure full profiles of member curvatures, rotations, plasticity spread, shear deformations, bar-slip induced rotations, flexural deformations, surface strains and crack widths (Sokoli et al., 2014). In all test, there were two linear potentiometers used to measure column lateral drifts to verify the optical system data. Strain gauges were glued on reinforcing bars to obtain strain data. The Data Acquisition System (DAQ) recorded data from actuator load cells, strain gauges, and other installed potentiometers. The DAQ system also recorded the image frame numbers of the optical system to synchronize the data from both systems.

Strain gauges were installed on the corner longitudinal bars from column ends until nearly the mid-height of the columns. However, the strain gauges located at interface between the columns and footings were only considered in this study as they were at the sections of highest moment where maximum strains occurred on the longitudinal bar. Specimens CM100 and CH60 had strain gauges on two middle longitudinal bars in addition to those on the corner bars. Additional details on instrumentation can be found in LeBorgne, 2012 and Sokoli, 2014.

3.2.4.1 Optical Measurement System

The optical measurement system used in the experiments utilized Digital Image Correlation (DIC) and as developed by Sokoli et al, 2014. The system tracks target locations in each recorded frame using a DIC algorithm. A calibration procedure adjusts for lens distortion and provides the necessary extrinsic and intrinsic camera parameters for the three -dimensional triangulation of target locations. The system tracks surface movements to a resolution on the order of $1/25^{th}$ of a pixel for raw location data, and a $1/100^{th}$ of a pixel after smoothing is applied to the location data.

After completing tracking, calibration, and the triangulation process, the system provided the three-dimensional movements of each target for the duration of the experiments. These three-dimensional movements can be processed to obtain global and local deformations, surface strains, and crack widths. In Series 1, targets were spaced at 3 in. on center, with 6 targets fitting per horizontal row. In the Series 2 and 3, targets were spaced at 2.75 in. on center, with 7 targets fitting per horizontal row. An additional row of targets was placed in each footing to allow for measurement of deformations at the column-to-footing interface (i.e., bar-slip induced deformations). The grids of targets are shown in Figure 3.3.

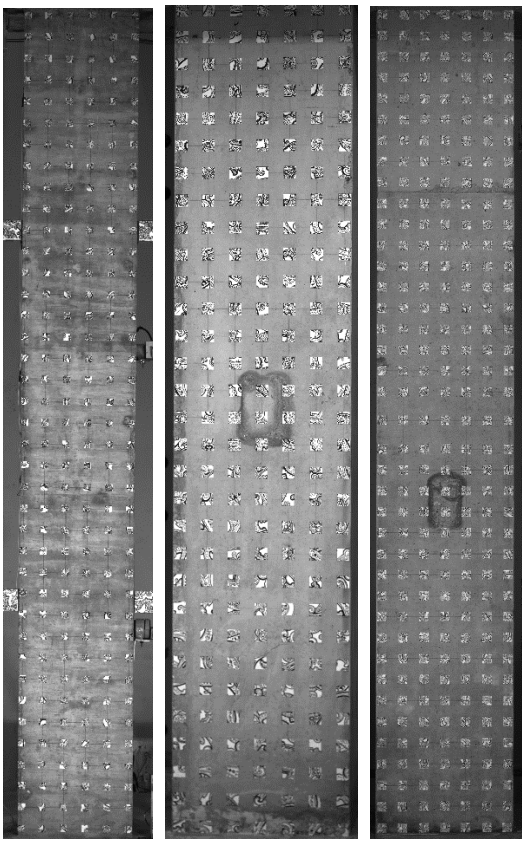

Figure 3.3 Column grid targets (left to right: Series 1, Series 2 and Series 3)

3.2.5 DATA PROCESSING

3.2.5.1 Global Deformations from DIC Data

Global deformations were obtained by processing three-dimensional target displacements. The total global deformation on the top of the column (lateral drift) was obtained by averaging difference in horizontal displacements of the targets on the top and footings. The DIC system was able to resolve deformations on the order of a $1/100^{th}$ of a pixel, which is equivalent to $1/10000^{th}$ of an inch. Lateral drift ratios were obtained by dividing lateral drifts by the column clear height for each specimen.

Global deformations were deconstructed as flexural deformations, shear deformations, and bar-slip induced rotations. Flexural deformations were extracted by integrating curvature over the

height of the column. Curvature profiles along the column were evaluated by assembling the difference in angle of rotation between two target rows divided by the measured distance between two rows over column height. Angles of rotation were computed at each frame as the change in the slope of regression line fitted through each horizontal row of targets with respect to the initial slope of the line prior to loading. Column end rotations, attributed mainly to slip of longitudinal bars (Ghannoum and Moehle (2012)) were determined as the difference in rotation between the rows of targets at column ends and the adjacent rows in the footings. Shear deformations were evaluated by subtracting the global lateral drift from bar-slip and flexural deformations.

3.2.5.2 Surface Strains from DIC Data

The surface targets arranged in a rectangular mesh (3 x 3 in. for Series 1 and 2.75 x 2.75 in. for Series 2 and 3) were used as nodal points for bilinear-strain quadrilateral elements. Assuming that strains varied linearly between targets, the measured x-directional (horizontal strain, ε_x), x-directional (vertical strain, ε_y), shear, and principal strains were determined (ε_1 = largest principal strain and ε_2 = smallest principal strain) for each bilinear-strain quadrilateral element (Figure 3.4). The system was able to resolve element surface strains on the order of 10^{-4} over the field of view; which is on the order of the cracking strain of concrete. The optical system captured the strain development under the initial application of the axial loads on the columns (Sokoli et al., 2014).

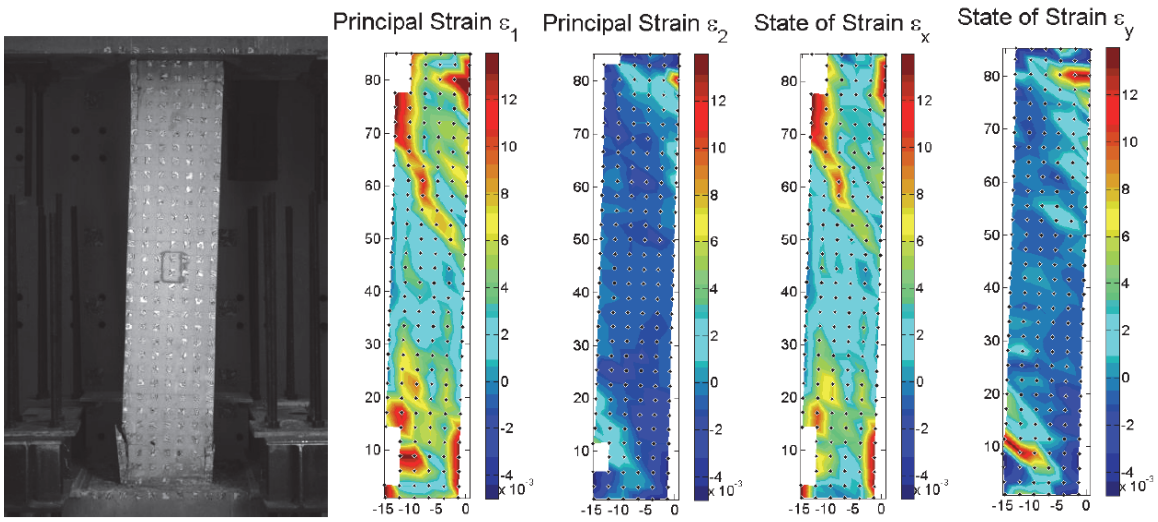

Figure 3.4 Surface strain of CS60 +3.00% drift ratio (Sokoli et al, 2014)

3.2.5.3 Forces from Actuators

Applied forces were computed using large-deformation equilibrium accounting for the location and inclination of all three actuators.

3.3 Column Lateral Behavior

3.3.1 COLUMN 2L06 ($\frac{P}{A_g f'c}$ = 0.19; T/Y = 1.64; $f_y\,(ksi)$ = 65.5; ρ_L = 2.5%; $f'c(ksi)$ = 3.13; a/d = 4.00)

The lateral load versus drift ratio response of column 2L06 is plotted in Figure 3.5. This specimen was tested under displacement controlled quasi-static reversed cyclic loading with an applied constant compressive axial load of 150 kips; which corresponds to an axial load ratio of 0.19 A_g f'$_c$ (where f'$_c$ = concrete compressive strength at the day of testing; A_g = gross-sectional area).

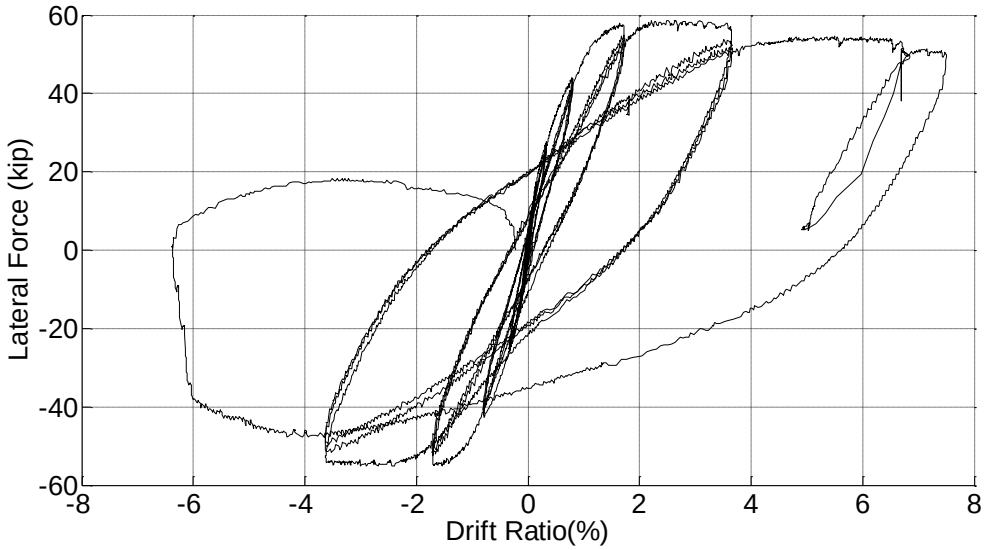

Figure 3.5 Response of column 2L06

There were no visible cracks on the column surface prior to loading. The first flexural cracks on the extreme tension face of the column end regions formed at a drift ratio of 0.69%. The average strain in the tension longitudinal reinforcement at the sections of maximum moment reached the yield strain at a drift ratio of 0.90%. At drift ratio of 0.92%, three inclined diagonal hairline shear cracks became visible on the column surface in the lower end region of the column. During the following three cycles at a drift ratio of 1.62%, bar slip cracks at the interface between column and the footing became visible and flexural cracks widened. At the next drift cycles (3.24% drift ratio), crushing of cover concrete in the end regions of the column was observed, shear crack extended diagonally at a 45 degrees angle from the compression toe towards the tension face of the column, and minor localized spalling was observed causing some targets to be lost. The maximum load was applied at drift ratio of 2.5% during the cycle to a drift ratio of 3.24%. During cycling to a drift ratio of 3.24%, spalling of the cover concrete was observed on the compression faces. After three cycles to a drift ratio of 3.24%, the lower end region of the column lost much of

the concrete cover and a shear crack widened. A similar scenario was observed at the top end-region of the column.

At the end of the first excursion to a drift ratio of 6.48%, the critical shear crack in the lower end region of the column widened substantially. When it was loaded in the opposite direction to drift ratio of 6.48%, initiation of lateral-strength loss occurred at drift ratio of 4% and the initiation of axial strength loss at drift ratio of 6%. The test was stopped after the initiation of axial strength loss. At the end of the test, the 90-degree hooks were found opened due to the loss of cover concrete causing the longitudinal bars to buckle, which initiate the axial strength loss. No bars fracture either of longitudinal or transverse bars was observed. Column 2L06 sustained a shear/axial failure mode (Leborgne, 2012).

3.3.2 COLUMN 2H06 ($\frac{P}{A_g f'c}$ = 0.41; T/Y = 1.64; $f_y\,(ksi)$ = 65.5; ρ_L = 2.5%; $f'c(ksi)$ = 3.34; a/d = 4.00)

The lateral load versus drift ratio response of column 2H06 is plotted in Figure 3.6. This specimen was tested under displacement controlled quasi-static reversed cyclic loading with and applied constant compressive axial load of 350 kips; which corresponds to an axial load ratio of 0.41 $A_g f'_c$.

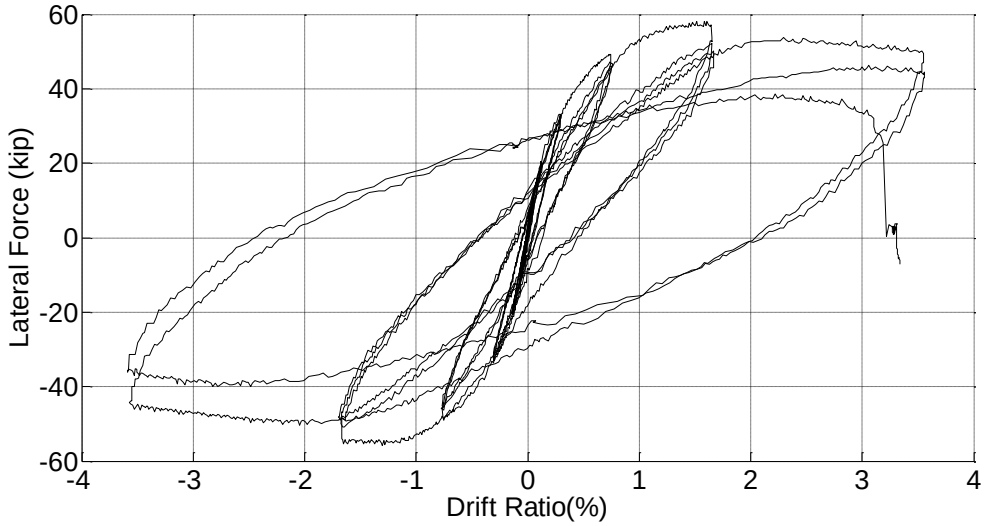

Figure 3.6 Response of column 2H06

There were no visible cracks on the column surface prior to loading. The first flexural cracks on the extreme tension face of the column end regions formed at a drift ratio of 0.65%. The average strain in the tension longitudinal reinforcement at the sections of maximum moment reached the yield strain at a drift ratio of 1.30%. At the end of first excursion to a drift ratio of 1.62%, the maximum lateral load was applied. After three cycles to a drift ratio of 1.62%, three inclined diagonal hairline shear cracks became visible on the column surface at both end regions of the column.

The damage progression occurred slowly over the three loading cycles at a drift ratio of 3.24%. By the end of first excursion to a drift ratio of 3.24%, wide inclined crack with 50-degree angle at the bottom end region of the column and 45-degree angle at the top end region of the column were formed. Halfway through the second excursion to a drift ratio of 3.24%, sliding along the 50-degree angle inclined crack at the bottom end region of the column was observed. Sliding resulted in spalling and crushing of the concrete around the shear crack. During the third excursion to a drift ratio of 3.24%, the initiation of lateral strength loss occurred at a drift ratio of 2.2% and the initiation of axial strength loss at a drift ratio of 3.1%. The test was stopped after the initiation of axial strength loss. At the end of the test, a similar scenario of opened 90-degree hooks and buckling of longitudinal bar were found in column 2H06 as occurred in column 2L06 but at lower drift ratio target cycles. No bars fracture either of longitudinal or transverse was observed. Column 2H06 sustained a shear/axial failure mode (Leborgne, 2012).

3.3.3 COLUMN CS60 ($\frac{P}{A_g f'c}$ = 0.30; T/Y = 1.41; $f_y\,(ksi)$ = 67.3; ρ_L = 4.7%; $f'c(ksi)$ = 3.83; a/d = 2.75)

The lateral load versus drift ratio response of column CS60 is plotted in Figure 3.7. This specimen was tested under displacement controlled quasi-static reversed cyclic loading with and applied constant compressive axial load of 370 kips; which corresponds to an axial load ratio of 0.3 A_g f'_c.

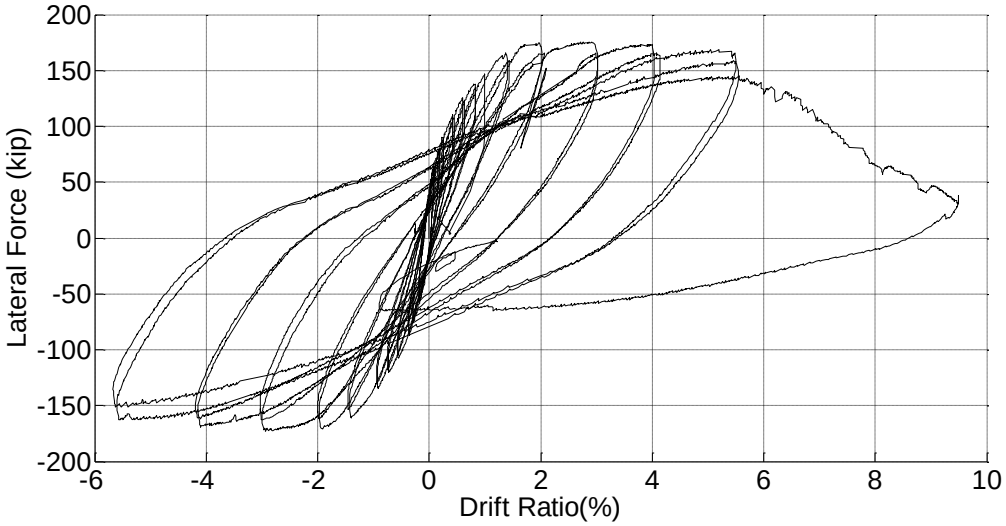

Figure 3.7 Response of column CS60

There were no visible cracks on the column surface prior to loading. The first flexural cracks on the extreme tension face of the column end regions formed at a drift ratio of -0.3%. The first inclined crack occurred and the horizontal cracks at the interface between the column and the footing opened up when the column was displaced to +0.6% drift ratio. Crushing of cover concrete at both end regions of the column was observed at the end of the first excursion to a drift ratio of +1.5%. The average strain in the tension longitudinal reinforcement at the sections of maximum moment reached the yield strain at a drift ratio of +2.0%. During cycles to drift ratio of 2.0%, the width of horizontal cracks increased and more flexural cracks formed close to the column's mid-height. At the end of the first excursion to a drift ratio of +3.0%, the maximum applied lateral force was applied. At a drift ratio of -3.0%, first yield in the transverse reinforcement was observed

based on optical data. The column remained stable and maintained axial load capacity past two cycles to a drift ratio of 5.5%. During the two cycles to a drift ratio of 5.5%, concrete spalled heavily on both ends of the column.

When the column was being pushed to the first excursion to a drift ratio of +7.0%, the initiation of lateral strength loss occurred at a drift ratio of +5.2% and the initiation of axial strength loss occurred at a drift ratio of +5.8%. Beyond a drift ratio of +6.0%, the column was no longer able to resist the initial axial load of 370 kips, which was reduced gradually to 280 kips as the column was pushed to a drift ratio of +9.1% where the test was stopped. No bar fracture on both longitudinal and transverse were observed. Column CS60 sustained a shear/axial failure mode.

3.3.4 COLUMN CS80 ($\frac{P}{A_g f'c}$ = 0.27; T/Y = 1.35; $f_y\,(ksi)$ = 79.1; ρ_L = 3.7%; $f'c(ksi)$ = 4.29; a/d = 2.72)

The lateral load versus drift ratio response of column CS80 is plotted in Figure 3.8. This specimen was tested under displacement controlled quasi-static reversed cyclic loading with and applied constant compressive axial load of 370 kips; which corresponds to an axial load ratio of 0.27 $A_g f'_c$.

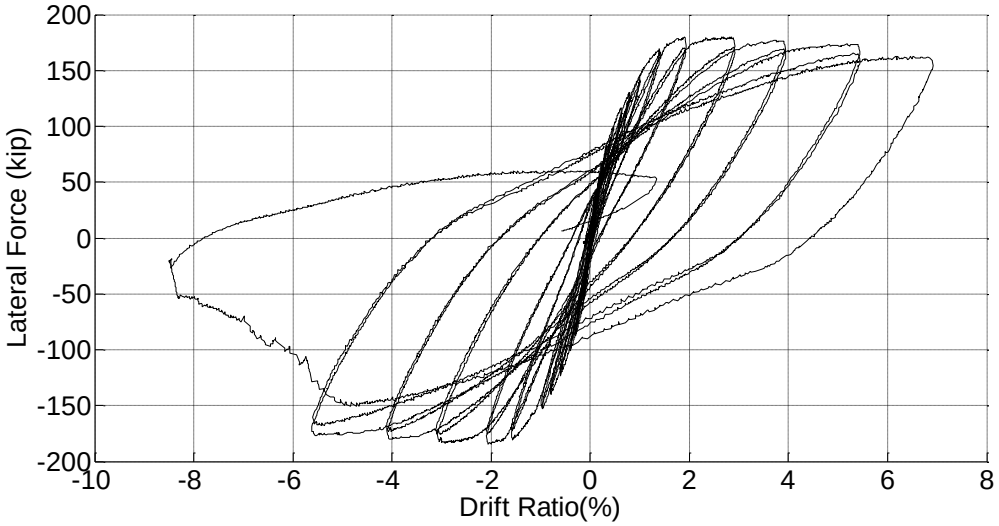

Figure 3.8 Response of column CS80

There were no visible cracks on the column surface prior to loading. The first flexural cracks on the extreme tension face of the column end regions formed at a drift ratio of +0.4%. The first inclined crack occurred and the horizontal cracks at the interface between the column and the footings opened up when the column was displaced to a drift ratio of +0.6%. The average strain in the tension longitudinal reinforcement at the sections of maximum moment reached the yield strain at a drift ratio of +1.05% on its way to the first excursion to a drift ratio of 1.5%. Crushing of cover concrete at both end regions of the column was observed at the end of the first cycle to a drift ratio of +1.5%. During cycles to a drift ratio of 2.0%, the width of horizontal cracks increased and more flexural cracks formed close to the column's mid-height. At the end of the first cycle to a drift ratio of +2.0%, the maximum applied lateral force was applied. At a drift ratio of -2.0%, first

yield in the transverse reinforcement was observed based on optical data. The column remained stable and maintained axial load capacity past two cycles to a drift ratio of 5.5%. During the two cycles to a drift ratio of 5.5%, concrete spalled heavily on both ends of the column.

The column survived the first excursion to a drift ratio of +7.0%. When the column was being pushed to the first excursion to a drift ratio of -7.0%, the initiation of lateral strength loss occurred at drift ratio of -4.5% and the initiation of axial strength loss occurred at a drift ratio of -4.6%. Beyond a drift ratio of -5.5%, the column was no longer able to resist the initial axial load of 370 kips, which was reduced gradually to 230 kips as the column was pushed to a drift ratio of -8.2% where the test was stopped. No bar fracture on both longitudinal and transverse were observed. Column CS80 sustained a shear/axial failure mode.

3.3.5 COLUMN CL100 ($\frac{P}{A_g f'c}$ = 0.15; T/Y = 1.16; $f_y\,(ksi)$ = 106; ρ_L = 1.1%; $f'c(ksi)$ = 5.11; a/d = 3.60)

The lateral load versus drift ratio response of column CL100 is plotted in Figure 3.9. This specimen was tested under displacement controlled quasi-static reversed cyclic loading with and applied constant compressive axial load of 252 kips; which corresponds to an axial load ratio of 0.15 A_g f'_c.

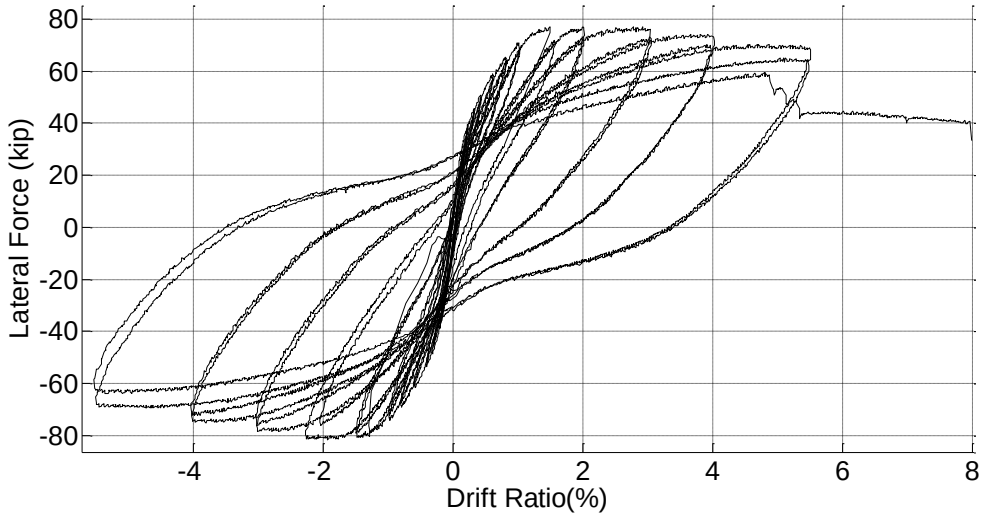

Figure 3.9 Response of column CL100

There were no visible cracks on the column surface prior to loading. The first flexural cracks on the extreme tension face of the column end regions formed at a drift ratio of -0.2%. The first inclined crack occurred when the column was displaced to the second excursion to a drift ratio of +0.6%. The average strain in the tension longitudinal reinforcement at the sections of maximum moment reached the yield strain at a drift ratio of +0.90%. During cycles to drift ratio of 2.0%, the width of horizontal cracks increased and more flexural cracks formed close to the column's mid-height. At the end of the first excursion to a drift ratio of -2.0%, the maximum applied lateral force was applied. The column remained stable and maintained axial load capacity past two cycles to a drift ratio of 5.5%. During the two cycles to a drift ratio of 5.5%, concrete spalled heavily on both ends of the column and longitudinal bars buckled causing loss of lateral strength. The column lost 9% in lateral strength at the second cycle to a drift ratio of +5.5%, compared to the strength observed during the first cycle.

When the column was being pushed to the first excursion to drift ratio of +7.0%, the first bar fracture occurred at a drift ratio of +4.8% and the lateral strength dropped by 28% from the previous cycle peak. After the first bar fracture, two more consecutive bar fractures occurred as the column was pushed further to a drift ratio of +7.0%. At a drift ratio of +7.0%, lateral strength dropped to 50% of the maximum applied lateral force. The test was stopped after a fourth bar fractured at a drift ratio of +8.0%. Column CL100 sustained a longitudinal bar fracture failure mode.

3.3.6 COLUMN CH100 ($\frac{P}{A_g f'c}$ = 0.15; T/Y = 1.27; $f_y\,(ksi)$ = 100; ρ_L = 1.1%; $f'c(ksi)$ = 5.21; a/d = 3.60)

The lateral load versus drift ratio response of column CH100 is plotted in Figure 3.10. This specimen was tested under displacement controlled quasi-static reversed cyclic loading with and

applied constant compressive axial load 252 kips; which corresponds to an axial load ratio of 0.15 $A_g f'_{c.}$

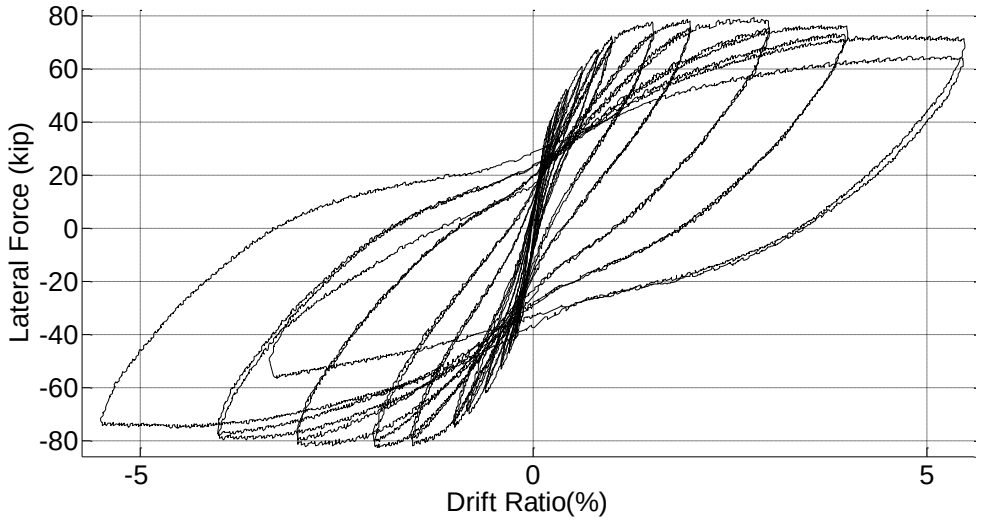

Figure 3.10 Response of column CH100

There were no visible cracks on the column surface prior to loading. The first flexural cracks on the extreme tension face of the column end regions formed at a drift ratio of -0.2%. The first inclined crack occurred when the column was displaced to the second excursion to a drift ratio of +0.6%. The average strain in the tension longitudinal reinforcement at the sections of maximum moment reached the yield strain at a drift ratio of -0.85%. During cycles to drift ratio of 2.0%, the width of horizontal cracks increased and more flexural cracks formed close to the column's mid-height. At the end of the first excursion to a drift ratio of -2.0%, the maximum applied lateral force was applied. The column remained stable and maintained axial load capacity past the first cycles to drift ratio of 5.5%. During the first cycles to a drift ratio of 5.5%, concrete spalled heavily on both ends of the column and longitudinal bar buckled causing loss of lateral strength. The column lost 15% in lateral strength at the second cycle to a drift ratio of -5.5%, compared to the strength observed during the first cycle.

When the column was being pushed back to the second cycle to drift ratio of +5.5%, the first bar fracture occurred at drift ratio of -3.2% and the lateral strength dropped 30% lower than the maximum applied lateral force. The test was stopped at the first bar fracture. Column CH100 sustained a bar fracture failure mode.

3.3.7 COLUMN CM100 ($\frac{P}{A_g f'c}$ = 0.15; T/Y = 1.27; $f_y\,(ksi)$ = 124; ρ_L = 1.1%; $f'c(ksi)$ = 5.58; a/d = 3.60)

The lateral load versus drift ratio response of column CM100 is plotted in Figure 3.11. This specimen was tested under displacement controlled quasi-static reversed cyclic loading with and applied constant compressive axial load of 260 kips; which corresponds to an axial load ratio of 0.15 A_g f'_c.

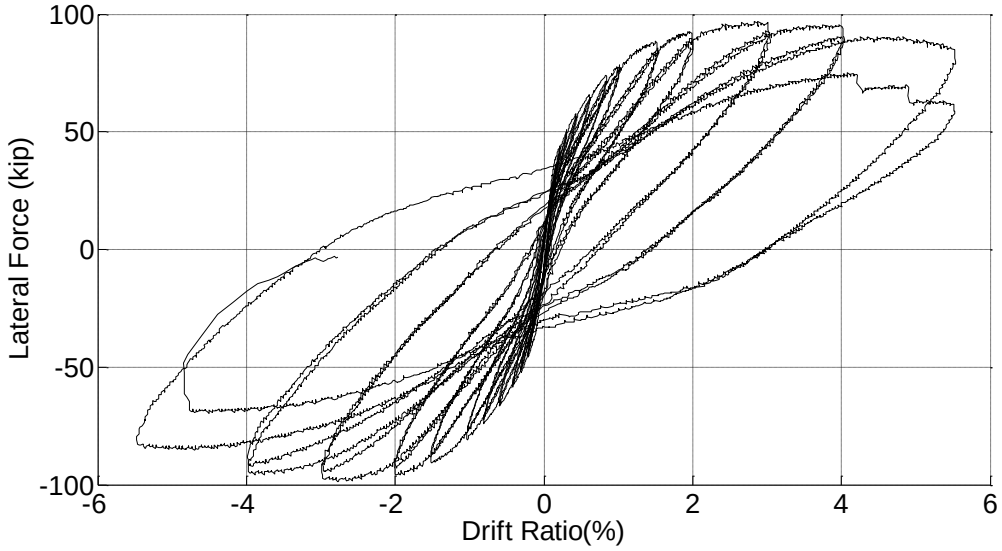

Figure 3.11 Response of column CM100

There were no visible cracks on the column surface prior to loading. The first flexural cracks on the extreme tension face of the column end regions formed at a drift ratio of +0.2%. The first inclined crack occurred when the column was displaced to the second excursion to a drift ratio of -0.6%. At the end of the first excursion to a drift ratio of 3.0%, the maximum applied lateral force

was applied. The column remained stable and maintained axial load capacity past the first cycles to a drift ratio of 5.5%. During the first excursion to a drift ratio of 5.5%, concrete spalled heavily on both ends of the column and longitudinal bar buckled causing loss of lateral strength. However, the bar buckling was substantially less severe than in column CH100, CL100 and CH60. During the excursion to the second cycle to a drift ratio of 5.5%, the first bar fracture occurred at a drift ratio of +4.2% and the second bar fracture at a drift ratio of +4.9%. The column lost 30% in lateral strength at the second cycle of +5.5% drift ratio compared to the strength recorded during the first cycle. When the column was being pushed back to the second cycle to drift ratio of -5.5%, the third bar fracture occurred at drift ratio of -4.7% and the lateral strength dropped to 30% lower than the maximum applied lateral force. The test was stopped at the third bar fracture. Column CM100 sustained bar fracture failure mode.

3.3.8 COLUMN CH60 ($\frac{P}{A_g f'c}$ = 0.15; T/Y = 1.45; $f_y\,(ksi)$ = 64.4; ρ_L = 1.1%; $f'c(ksi)$ = 4.57; a/d = 3.60)

The lateral load versus drift ratio response of column CH60 is plotted in Figure 3.12. This specimen was tested under displacement controlled quasi-static reversed cyclic loading with and applied constant compressive axial load of 220 kips; which corresponds to an axial load ratio of 0.15 A_g f'_c.

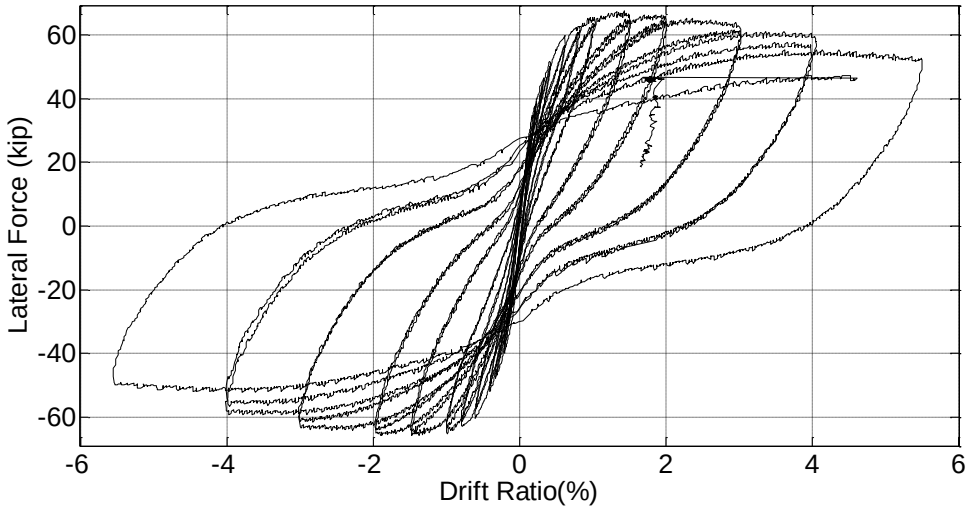

Figure 3.12 Response of column CH60

There were no visible cracks on the column surface prior to loading. The first flexural cracks on the extreme tension face of the column end regions formed at a drift ratio of +0.2%. The average strain in the tension longitudinal reinforcement at the sections of maximum moment reached the yield strain at a drift ratio of 0.425%. The first inclined crack occurred when the column was displaced to the second excursion to a drift ratio of +0.6%. At the end of the first excursion to a drift ratio of 1.5%, the maximum applied lateral force was applied. The column remained stable and maintained axial load capacity past the first cycles to a drift ratio of 5.5%. During the first cycles to a drift ratio of 5.5%, concrete spalled heavily on both ends of the column and longitudinal bar buckled causing loss of lateral strength. When the column was being pushed back to the second cycle to drift ratio of +5.5%, the first bar fracture occurred at a drift ratio of +4.6% and the lateral strength dropped 31% lower than the maximum applied lateral force. The test was stopped at the first bar fracture. Column CH60 sustained bar fracture failure mode.

3.4 Behavioral Milestones

This section presents the major behavioral milestone and deformation levels at which they occurred: the first flexural crack (1st FC), the first inclined crack (1st IC), the mean longitudinal reinforcement yield (M LBY), the first transverse reinforcement yield (1st TBY), spalling damages state 1 (SD1), spalling damages state 2 (SD2), and spalling damages state 3 (SD3).

The first flexural crack (1st FC) and the first inclined crack (1^{s} IC) were identified by surface strains acquired from the DIC system and verified by visual inspection at the end of the loading cycle. An inclined crack was defined as a crack having an angle greater than 20 degrees relative to the horizontal plane. The mean longitudinal reinforcement yield (M LBY) was identified from strain gauges installed at the interfaces of the column and footings where the demands were expected to be the largest. This milestone was determined to occur at the mean of the drift ratios at which

each bar reached first yield. First yielding of transverse bar reinforcement (1st TBY) was identified by monitoring surface strains and tie strain gauges for strain increases (Sokoli et al., 2014).

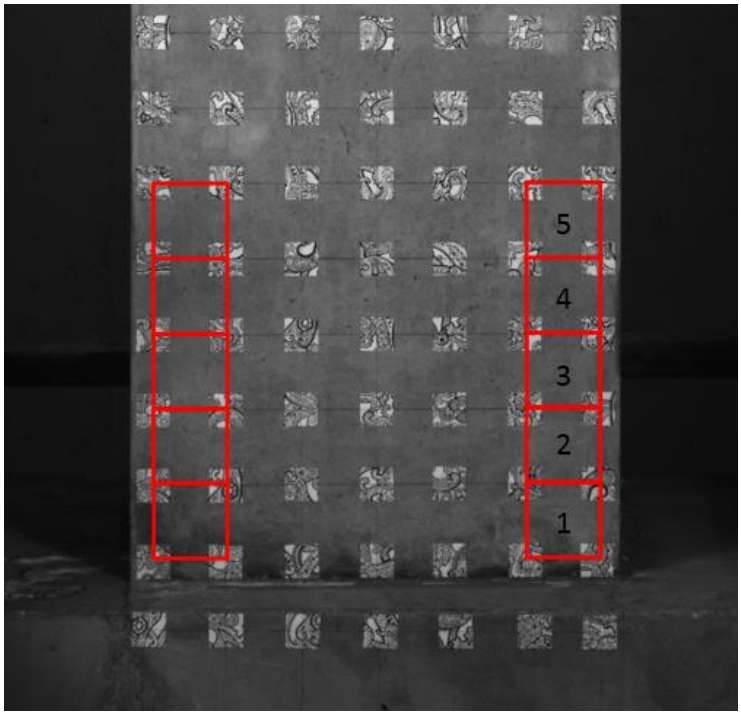

Figure 3.13 Horizontal strain exterior elements (red squares) and rows (numbers)

Spalling damages states (SD1, SD2, SD3) were identified by plotting the maximum of horizontal surface strains of five row of the exterior elements near both column ends (Figures 3.13 to 3.18). Horizontal surface strains at those locations captured the spalling behavior during the tests. Five row of exterior elements were analyzed. Row numbers are marked in Figure 3.13. The milestone SD1 was defined as the first jump in the horizontal strain in Row 1 elements, and represented when the first hairline spalling crack occurred (Figure 3.19). SD2 was defined as the point when any horizontal strain jumped above 0.02, which represented when significant widening of spalling cracks occurred (Figure 3.20). SD3 was defined as the point when any horizontal strain jumped above 0.04, which represented when the column was severely damaged due to spalling (Figure

3.21). In Figures 3.14 to 3.18, plots of the horizontal strains versus frame numbers are given, with the frames at which the first excursions to various target drift ratios occurred being highlighted. The horizontal strain measurement stopped when targets were lost due to the concrete spalling. Horizontal strain measurement for column 2L06 and 2H06 were unavailable because of lack of data. Horizontal strain measurements for column CM100 were still being processed when this thesis was submitted.

The lateral drifts at which the behavioral milestones occurred are presented in Table 3-8 for all specimens.

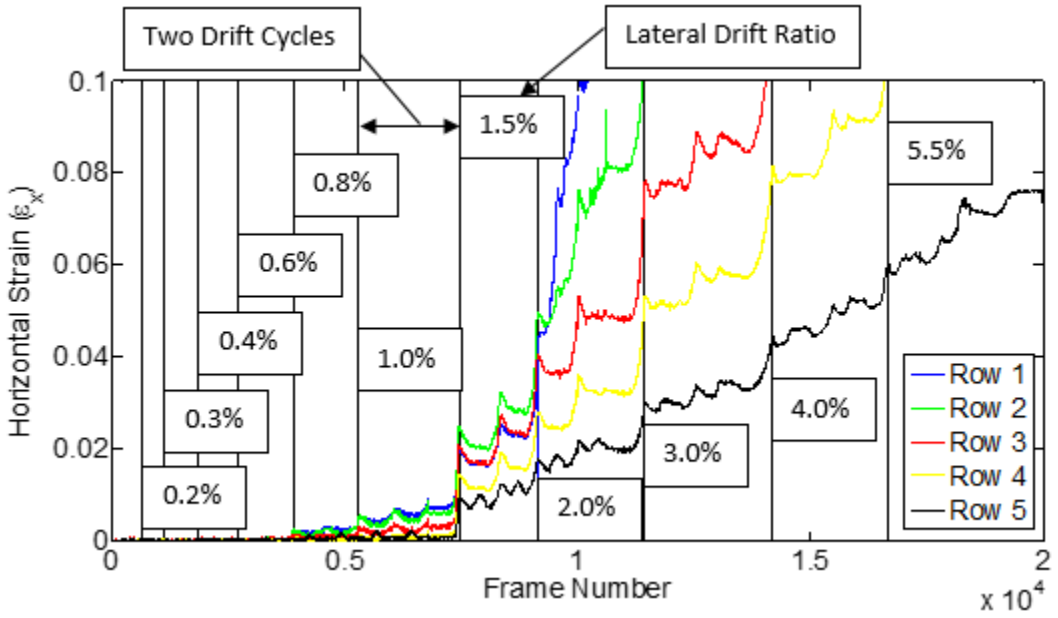

Figure 3.14 CS60 horizontal strains

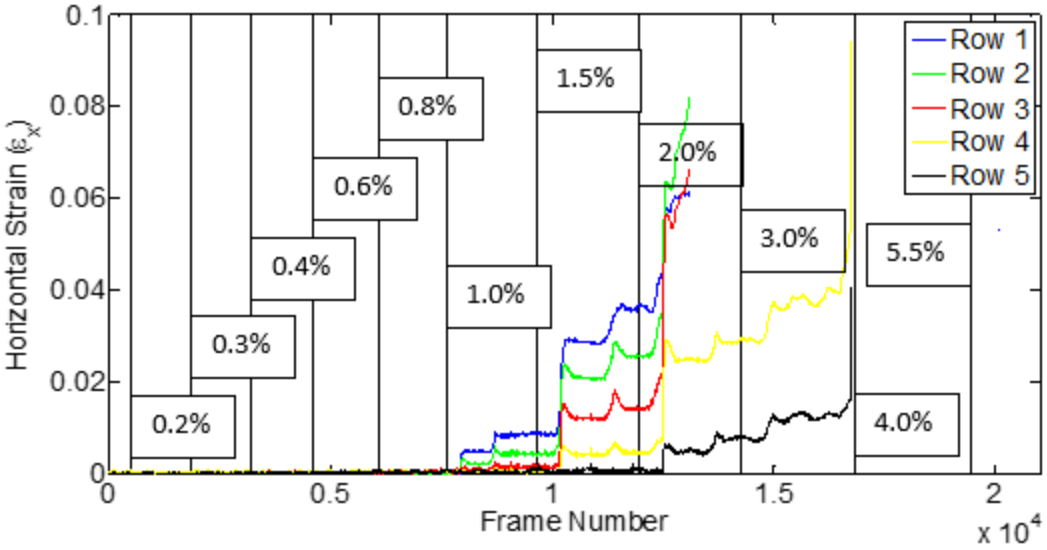

Figure 3.15 CS80 horizontal strains

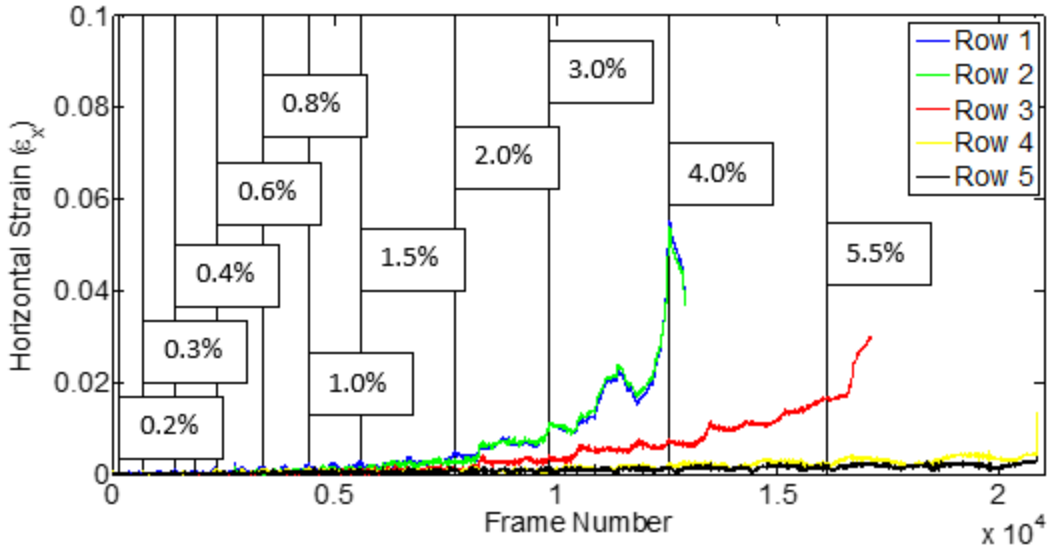

Figure 3.16 CL100 horizontal strains

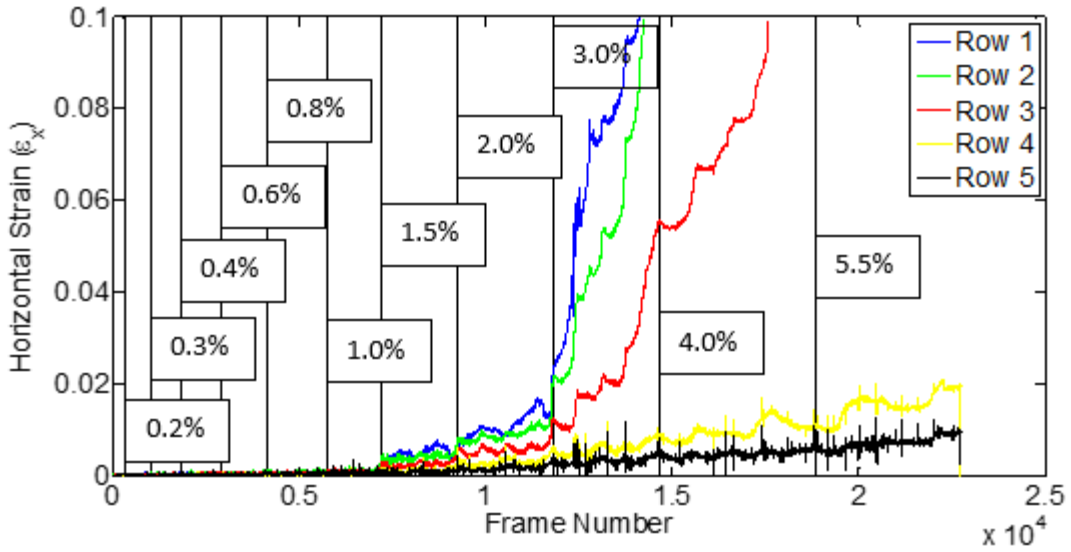

Figure 3.17 CH100 horizontal strains

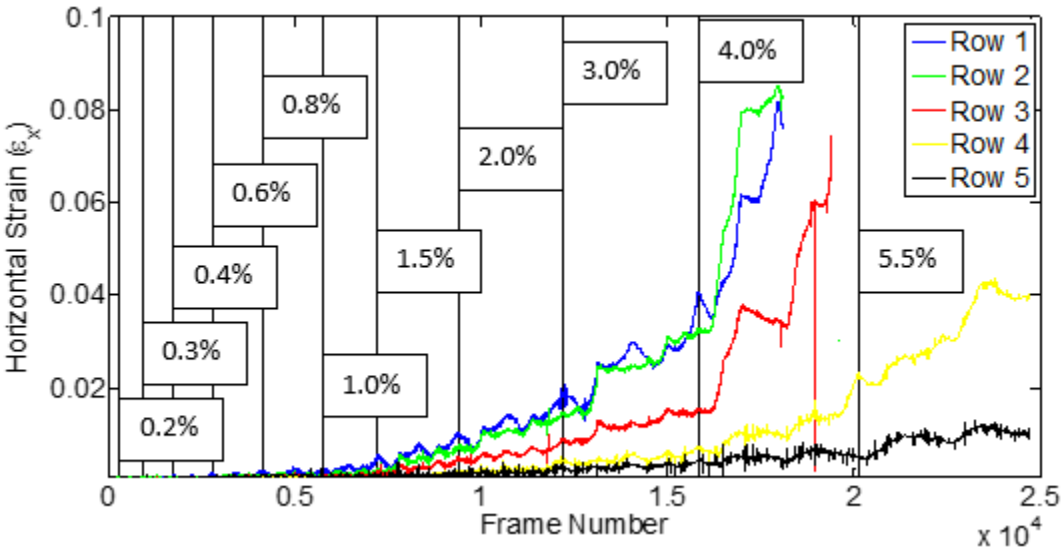

Figure 3.18 CH60 horizontal strains

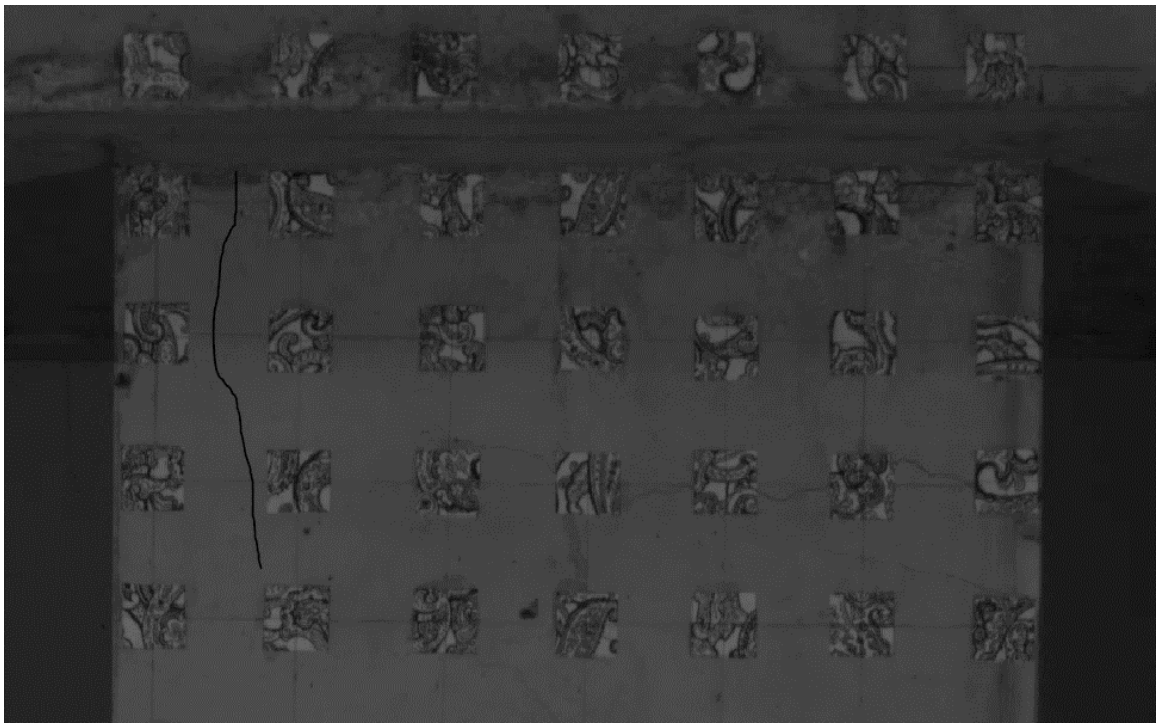

Figure 3.19 Spalling damage states 1 (SD1) for column CH100 (hairline crack highlighted)

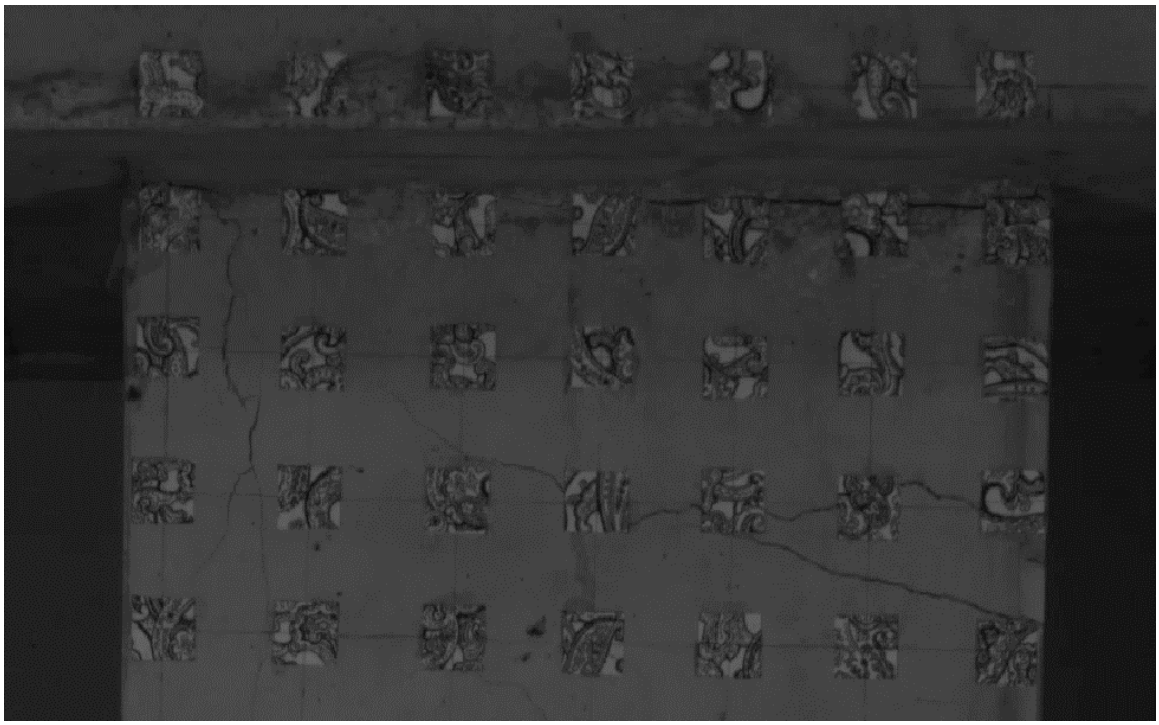

Figure 3.20 Spalling damage states 2 (SD2) for column CH100

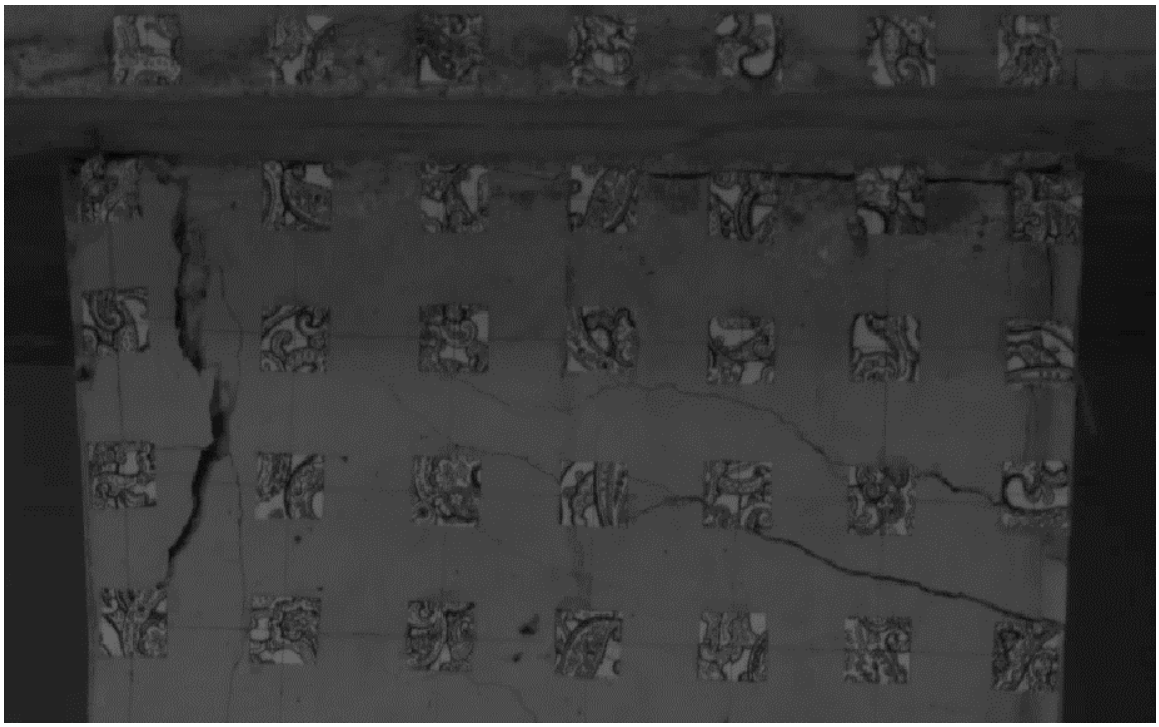

Figure 3.21 Spalling damage states 3 (SD3) for column CH100

Table 3-8 Lateral drift rations at the behavioral milestones

Specimen	First Flexural Crack (1st FC)	First Inclined Crack (1st IC)	Mean Longitudinal Bar Yield (M LBY)	First Transverse Bar Yield (1st TBY)	Spalling Damage 1 (SD1)	Spalling Damage 2 (SD2)	Spalling Damage 3 (SD3)
2L06	0.69%	0.92%	0.90%	N/A	N/A	N/A	N/A
2H06	0.65%	1.62%	1.30%	N/A	N/A	N/A	N/A
CS60	0.30%	0.60%	2.00%	3.00%	0.60%	1.32%	1.67%
CS80	0.40%	0.60%	1.05%	2.00%	1.00%	1.41%	2.00%
CL100	0.20%	0.60%	0.90%	none	1.50%	2.70%	3.12%
CH100	0.20%	0.60%	0.85%	none	1.50%	2.87%	3.00%
CM100	0.20%	0.60%	N/A	none	N/A	N/A	N/A
CH60	0.20%	0.60%	0.43%	none	1.00%	2.68%	3.99%

3.4.1 DISCUSSION

Based on Table 3-8, first flexural cracks occurred before the first longitudinal bar yield for all the columns, and also occurred at a relatively low drift ratio. The first inclined cracks for columns under high shear stresses occurred at lower drifts than in the other columns. For columns with

relatively low shear stresses, the first inclined cracks occurred around the yielding of the longitudinal bars. SD1, which captures the initiation of spalling cracks, also occurred at lower drifts with increasing shear stresses and axial loads (CS60 and CS80). The initial spalling cracks for both columns under high shear stresses (CS60 and CS80) occurred earlier than the yielding of longitudinal bars. This early spalling was observed to affect the longitudinal bar strain measurement of those columns due to debonding of the reinforcement from the concrete and may have delayed the yielding of the longitudinal bars to a higher drift levels (see Section 3.6). This behavior may have caused longitudinal bar yielding to occur at a relatively high drift ratio at of 2.0% in column CS60.

Both of the columns under high shear stresses (CS60 and CS80) suffered high levels of spalling damage at approximately half of the drift ratio levels of the columns under much lower shear stresses (Figure 3.14 to Figure 3.18). The damage of Series 2 columns under high shear stresses (CS60 and CS80) spread until the elements of row 5, with horizontal strains surpassing 0.04 prior to shear failure. This contrasts the behavior of Series 3 columns (CL100, CH100 and CH60) in which the row 5 element horizontal strains remained below 0.02. This damage spread was believed due to the high axial load ratio and high shear stresses which made the concrete reach crushing strains at earlier drifts.

The damage concentration in columns within the same series also showed discrepancies. In Series 2 columns, the end horizontal strains in column CS60 appeared to be higher for each element row and at every drift ratio level than in column CS80. The damage in column CS80 appeared to be more concentrated at the ends of the column compared with column CS60. The same trend was observed in the Series 3 columns. The spalling damage in column CL100 appeared to be more concentrated at column ends than in column CH100. This was concluded by comparing the strains

of elements at rows 3, 4 and 5. Column CH100 damage appeared to be more concentrated at column ends than in Column CH60. This was also concluded from observing higher horizontal strains at element row 4 for column CH60. In Series 2, column CS80 longitudinal reinforcement had a T/Y ratio of 1.34, which was lower than that of bars in column CS60 (T/Y ratio of 1.41). In Series 3, column CL100 longitudinal reinforcement had a lower T/Y ratio of 1.16 compared to reinforcement in columns CH100 and CH60, which had a T/Y ratio of 1.27 and 1.45, respectively. Therefore, the damage concentration in concrete columns were believed to be partially caused by the differences in tensile to yield ratio (T/Y ratio) of the longitudinal reinforcement. The lower T/Y ratio of longitudinal reinforcement increased damage concentration. This behavior will be explored in more detail in Chapter 4.

3.5 Deformations

In this section, column global deformations are subdivided into flexural deformations, shear deformations, and bar-slip deformations. These deformations will be utilized in Chapter 4 to verify that the analytical model proposed for estimating reinforcement strains also satisfies column global deformations.

3.5.1 Global Lateral Deformations

The three major components of column global lateral deformations are flexural deformations, bar slip deformations, and shear deformations. Those deformations were acquired from the optical measurement system as described in Section 3.2.5.1. The optical data was only reliable until a drift ratio of 3.24% for Series 1 columns, and 3.00% for Series 2 and 3 columns.

Column lateral displacement (Δ) was normalized with the respective column clear height (L) to produce the lateral drift ratio (Δ/L). The flexural deformation component was normalized by

column height to obtain the flexural drift ratio (DR_{flex}). Likewise, bar slip and shear deformation components were normalized to obtain the bar slip drift ratio (DR_{slip}) and shear drift ratio (DR_{shear}), respectively:

$$Drift\ Ratio\ \left(\Delta/L\right) = DR_{flex} + DR_{slip} + DR_{shear} \tag{3-1}$$

The force versus deformation components hysteresis curves are in Figure 3.22 to Figure 3.29. In addition, the percentage contribution of each component to the total deformation are also were plotted for each drift ratio target in the figures.

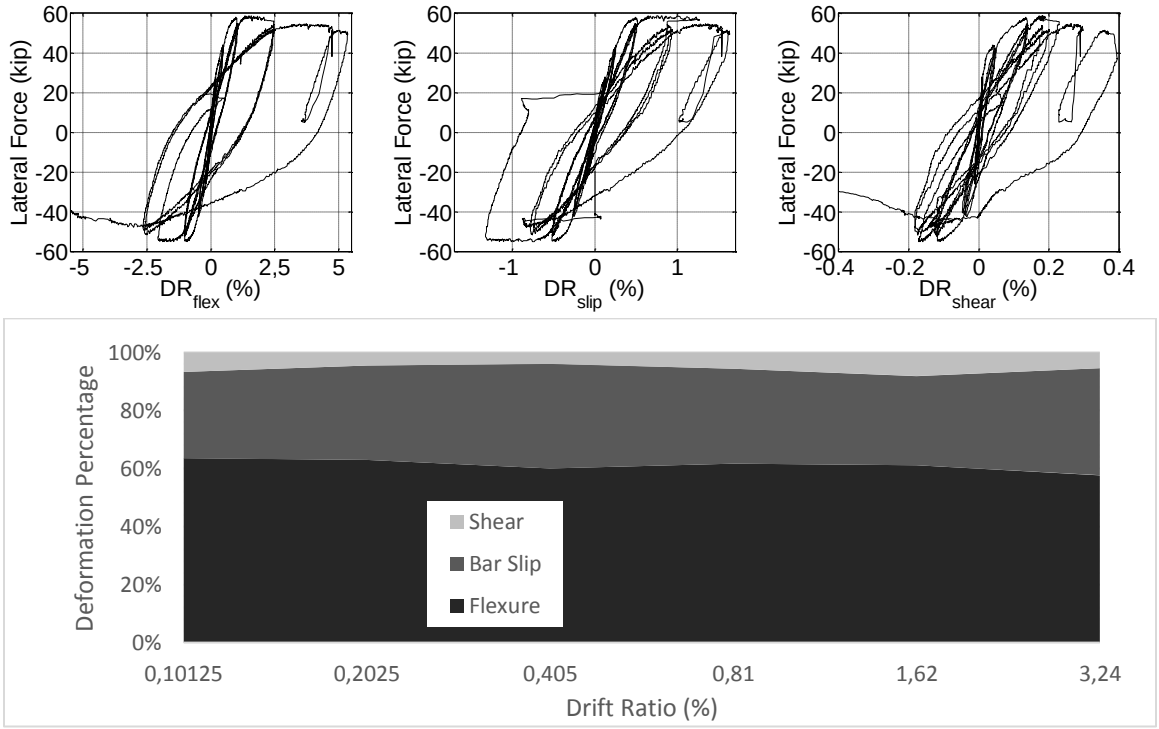

Figure 3.22 2L06 deformation components

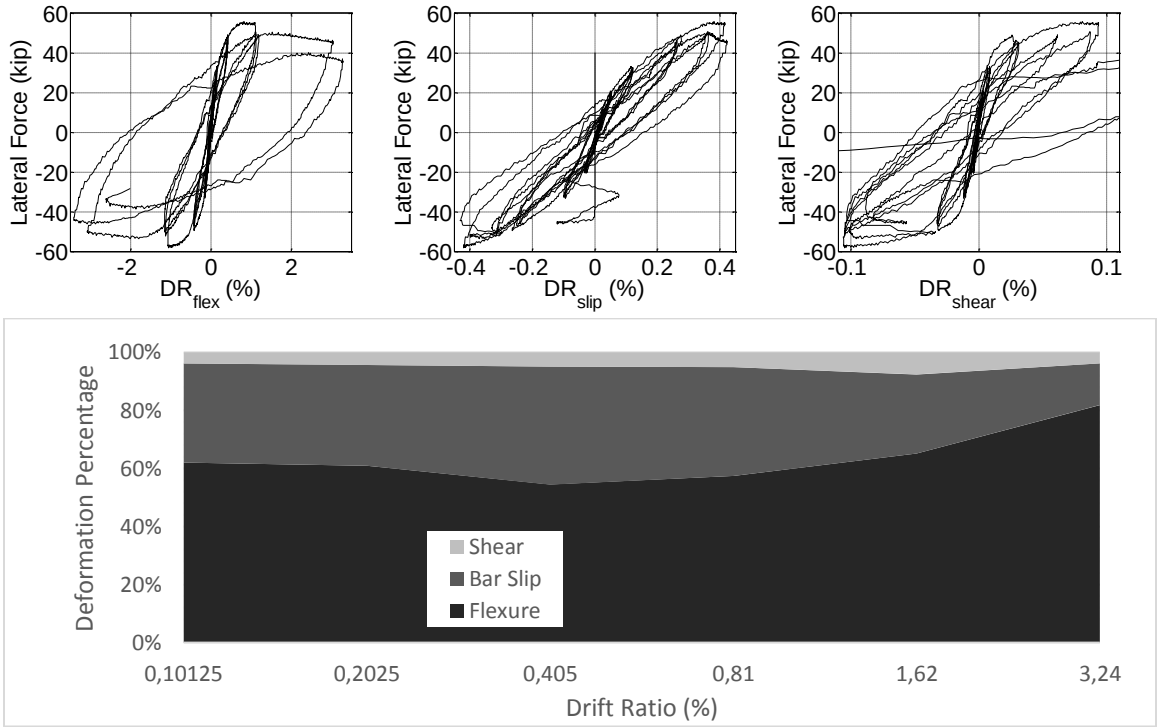

Figure 3.23 2H06 deformation components

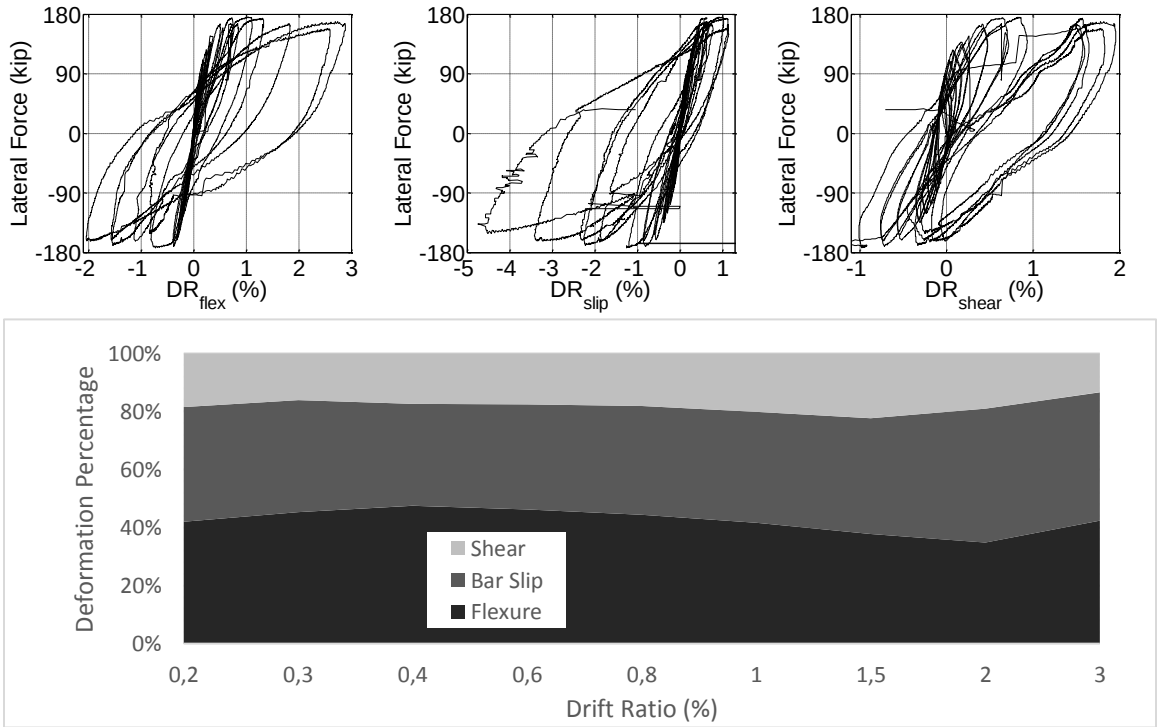

Figure 3.24 CS60 deformation components

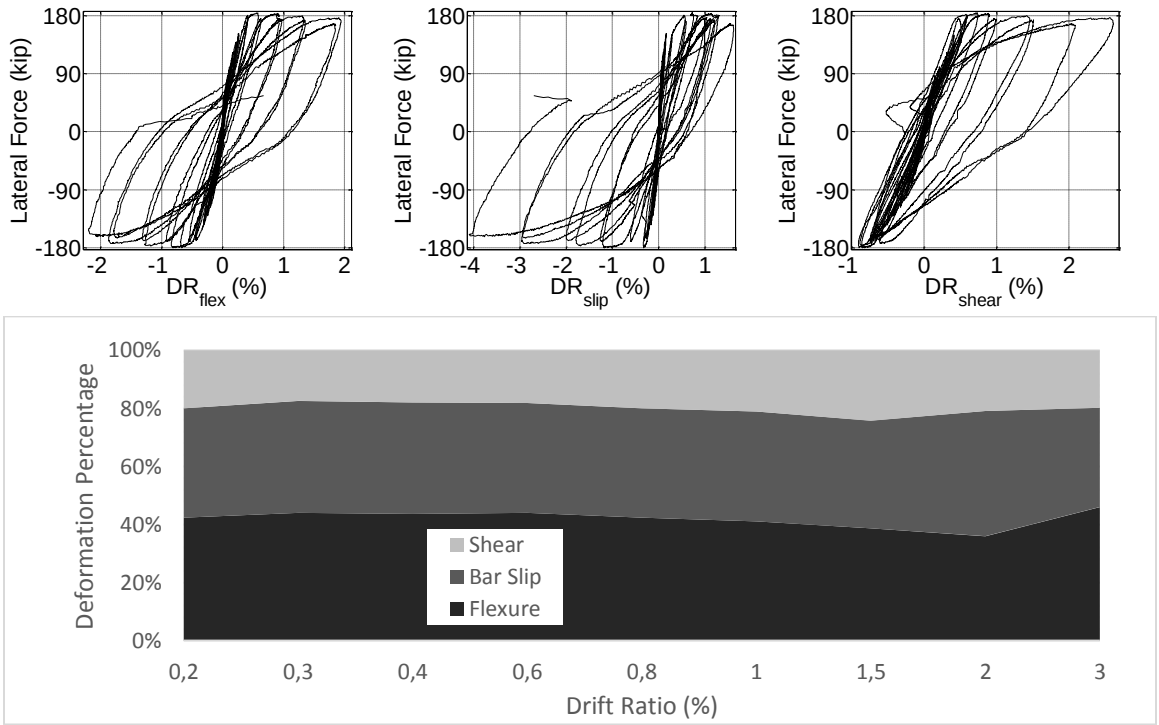

Figure 3.25 CS80 deformation components

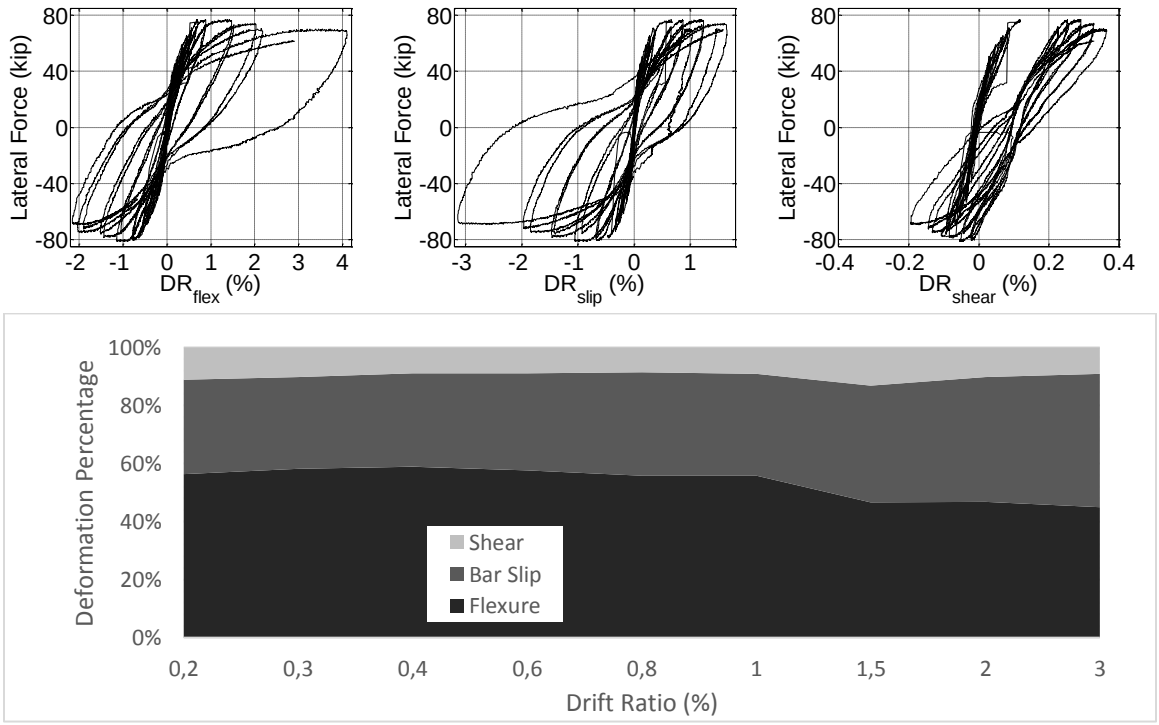

Figure 3.26 CL100 deformation components

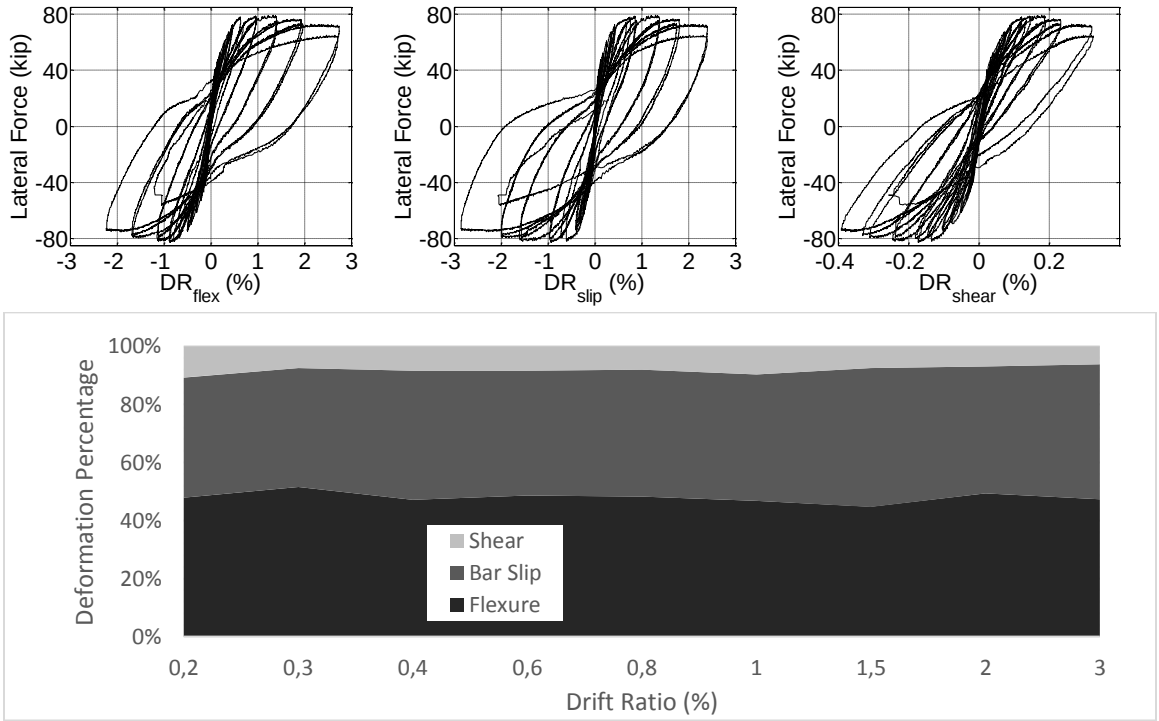

Figure 3.27 CH100 deformation components

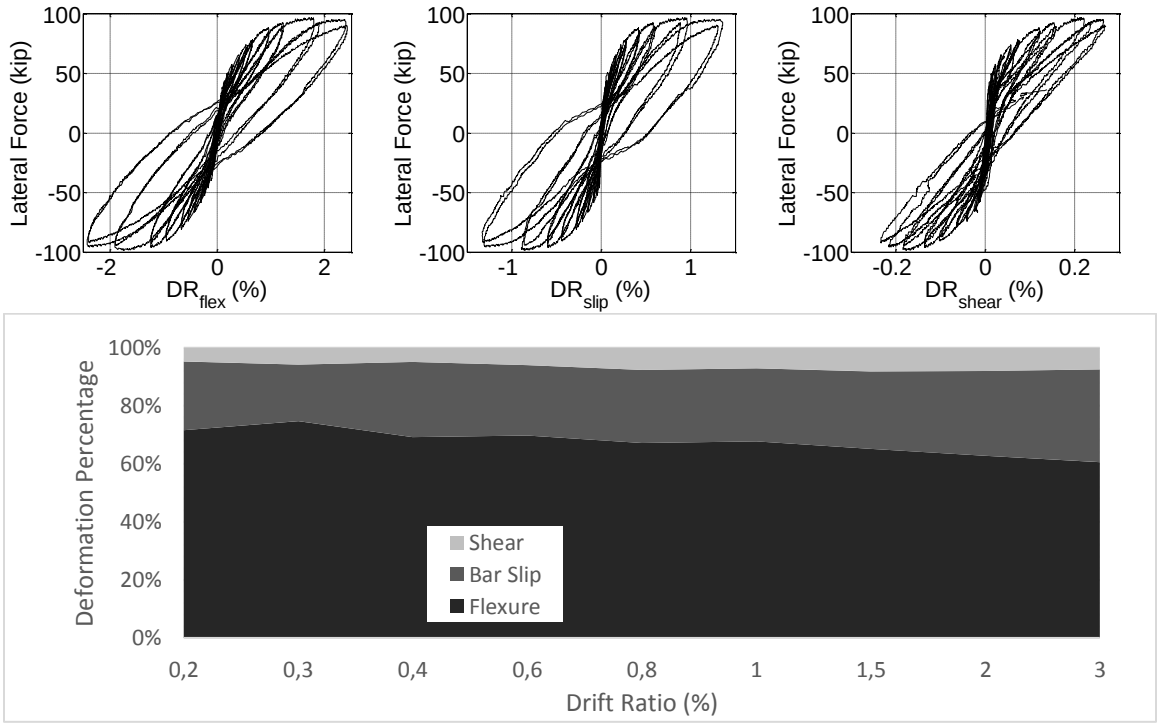

Figure 3.28 CM100 deformation components

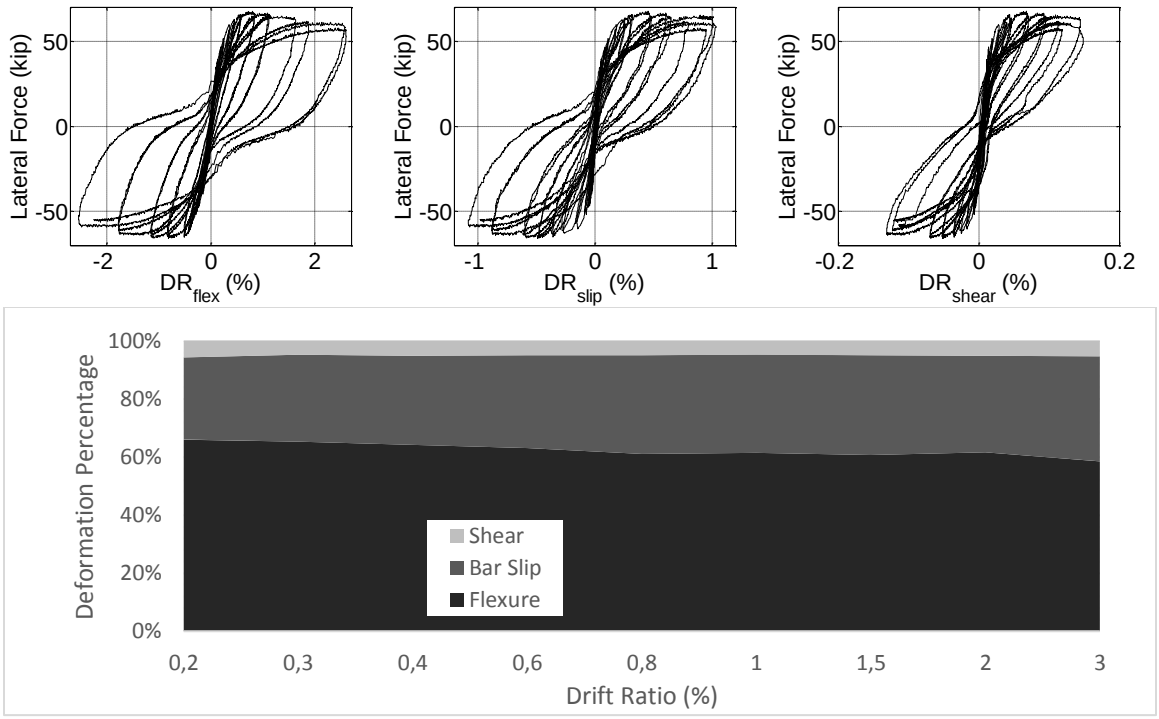

Figure 3.29 CH60 deformation components

For both columns in Series 1, shear deformation contributed roughly 5-8% of the total drift at the loading point. Bar slip deformations contributed in range of 30-40%, except at 3% drift ratio of column 2H06, where bar slip deformations accounted for only 14% of total drift. For both columns in Series 2, shear deformation percentages were relatively large around 20% of the total drift. Bar slip deformation percentages were around 40%. For Series 3 columns, shear deformation contributed in range of 8-14% for CH100 and CL100 and 5-8% for CM100 and CH60. Bar slip deformation contributed 45% in average for column CH100. For column CL100, bar slip deformation percentages were around 33% for drift ratio level less than 1% and jumped up to 44% at drift ratios greater than 1%. Column CM100 bar slip deformation percentages were relatively small compared to CH100 and CL100 at around 25% and increased to around 30% at higher drift ratio. Column CH60 bar slip deformation percentages were around 30% at early drift ratio and increased up to 36% at a drift ratio of 3.0%.

3.6 Strains

3.6.1 Measured Strain - Data Processing

Measured longitudinal bar tension strains that are presented in this study were obtained from the strain gauge readings on bars at the extreme compression and tension faces and at the sections of highest moment at both ends of the columns. The longitudinal bar compression strains were not the focus of this study and not be presented in this thesis. The measured strain plots were constructed by connecting with straight lines strain measurements at the first cycle to each drift target (Figure 3.30). The second cycle strain value at the same drift target was only marginally smaller for all columns, as shown in Figure 3.31 for column (CH100) with low shear stresses and axial load and column (CS80) with high shear stresses and axial load. For the purpose of this study, which is to predict the longitudinal bar reinforcement strain demand at a certain drift level, the slightly larger first cycle strain values were used. Mean strain (ε_M) was calculated as the mean value of each reliable strain gauge measurement on corner bars at each drift level. Due to the variability in the strain measurements from bar to bar at a critical section (Figure 3.32), the mean strain (ε_M) was targeted in the proposed analytical model. A sample plot of measured strains at critical sections for various longitudinal bars and the mean strain for column CH100 is shown in Figure 3.32, while the same plots are presented in Appendix A for the other columns.

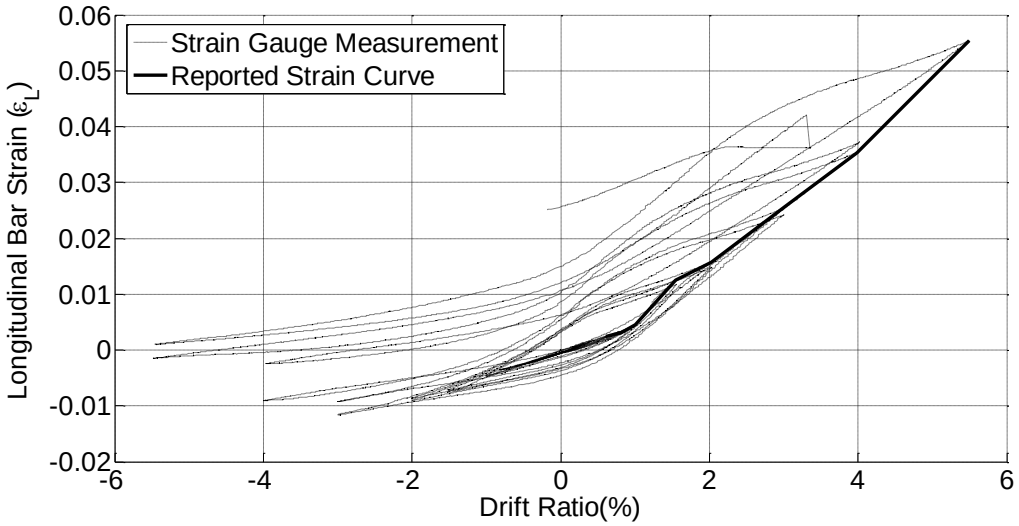

Figure 3.30 Reported strain

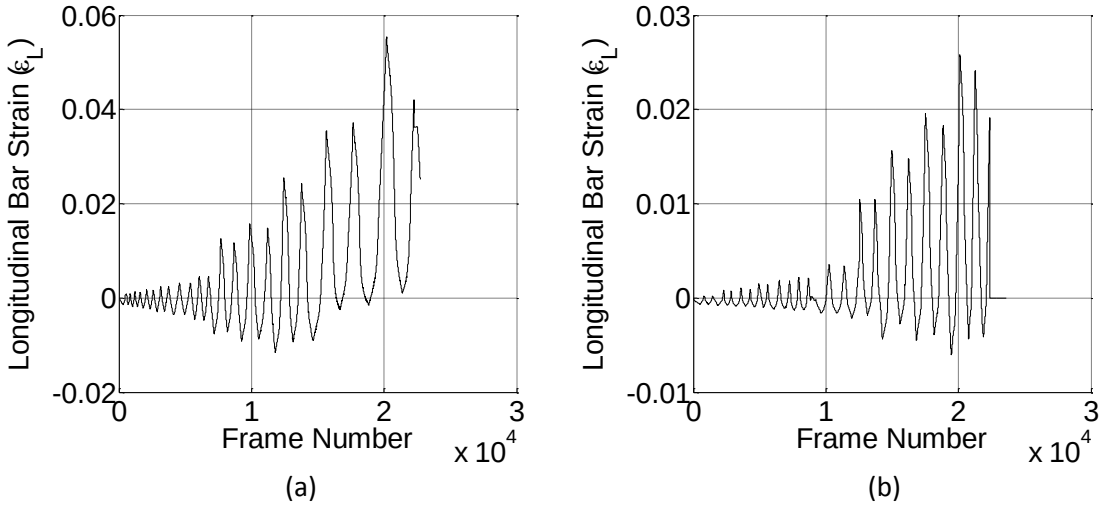

Figure 3.31 Sample longitudinal bar strain history: (a) Column CH100; (b) Column CS80

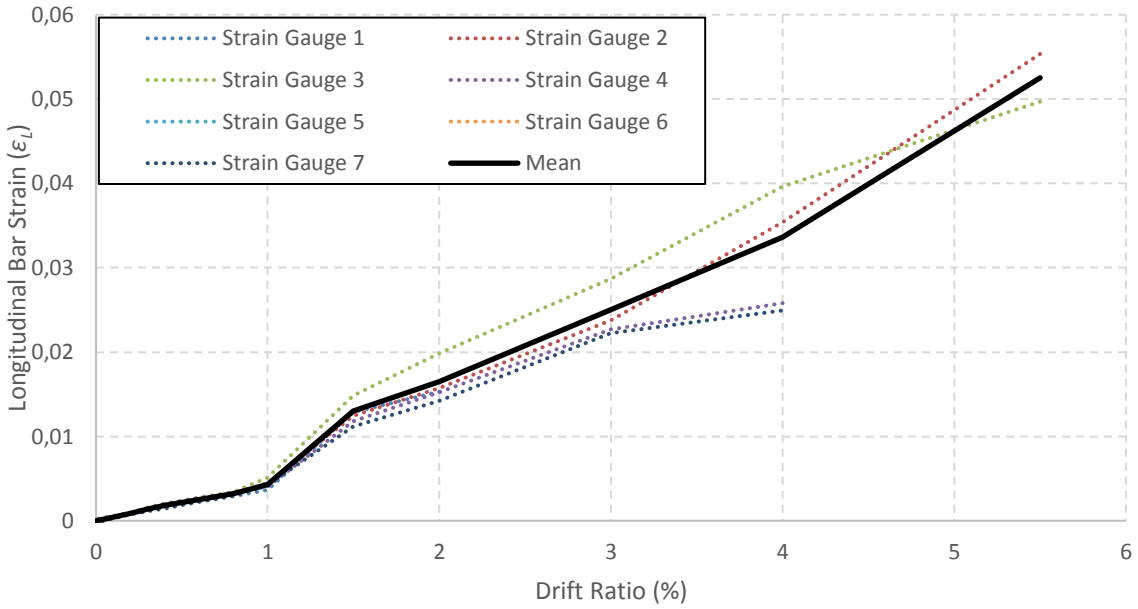

Figure 3.32 Measured longitudinal bar strains in column CH100

3.6.2 MEAN STRAIN

Mean strains are plotted for all columns versus drift ratio in Figure 3.33. One of the variables that influences the value of strain in longitudinal bar is the effective depth (*d*) of the column section in the direction of loading. The effective depth (*d*) is taken as the distance measured from the extreme compression fiber to the centroid of the outermost layer of longitudinal tension reinforcement. The bigger the effective depth, the larger the longitudinal bar strain value is at a given lateral drift. The measured strain normalized by effective depth versus the lateral drift ratio was used to provide more direct comparison between columns in Figure 3.34. The strain measurements were believed to be reliable up to at most a drift ratio of 4.0% for all columns.

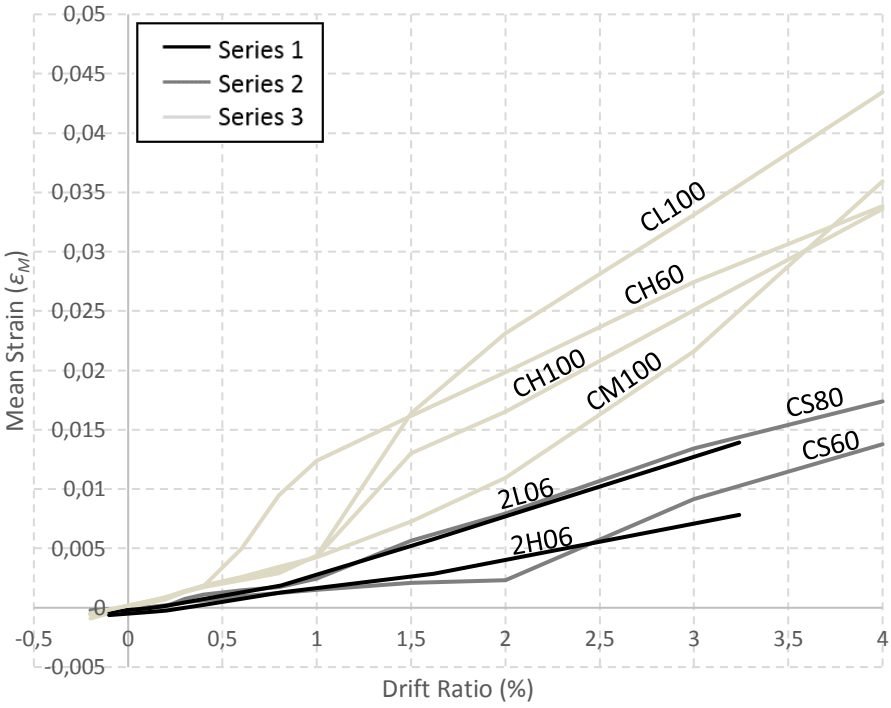

Figure 3.33 Mean strain vs drift ratio

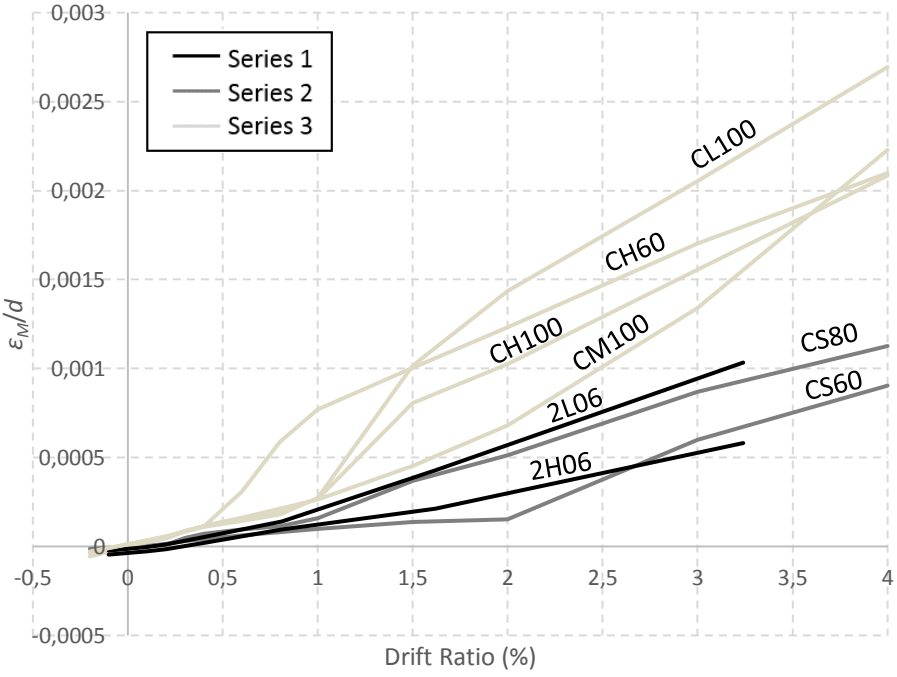

Figure 3.34 Normalized mean strain vs drift ratio

3.6.3 STRAIN RESULT TRENDS

In this section, mean strain plots are overlaid with behavioral milestones to capture investigate relations between milestones and strains (Figure 3.35).

As can be seen Figure 3.35, a strain jump (rapid increase in strain with increasing lateral drift) appeared right after the drift at which the mean longitudinal bar strains reached yielding. For columns CL100 and CH100, the strain increase with drift reduces after the first spalling crack occurs (milestone SD1).

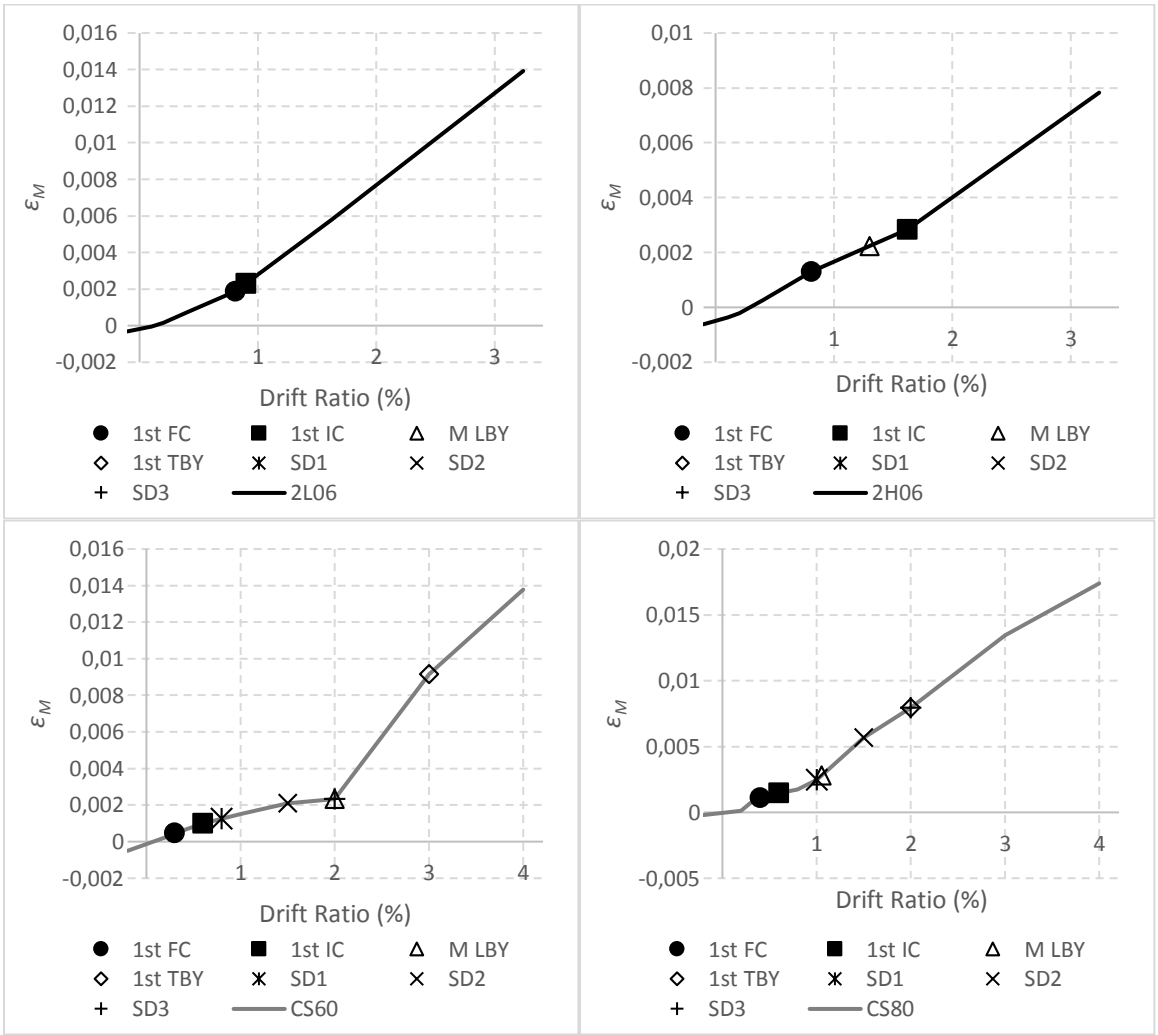

Figure 3.35: continued next page.

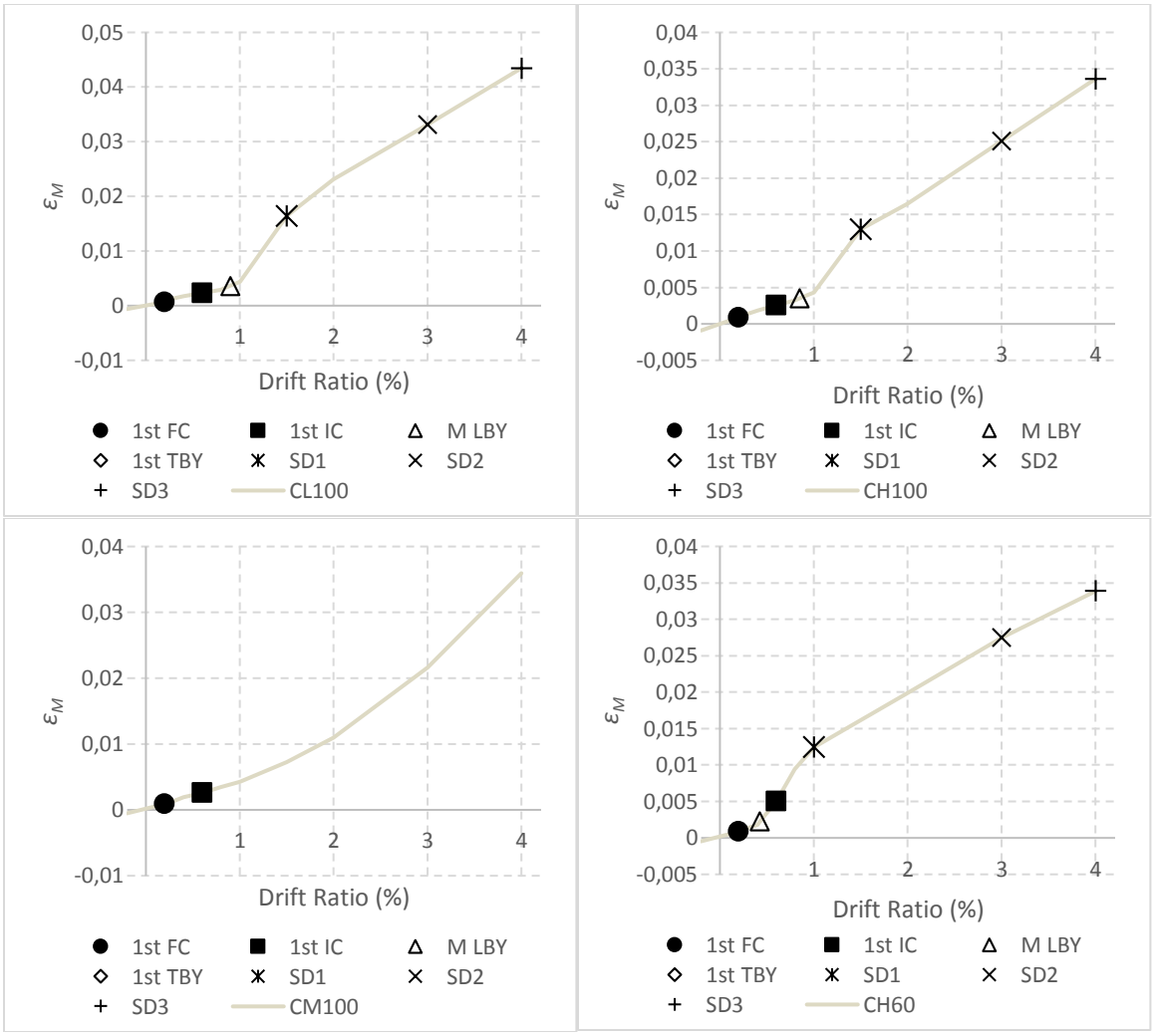

Figure 3.35 Mean strain versus drift ratio (all columns)

For CL100, CH100 and CH60, Figure 3.35 indicates that the columns with lower longitudinal bar yield strength experienced bar yield at lower drift ratios. This was demonstrated as column CH60 experienced bar yielding at an earlier drift level than the other Series 3 columns reinforced with grade 100 bars. From Figure 3.34, it can also be seen that columns with the same design and axial load ratio (CL100, CH100, CM100 and CH60) experienced the same strain increase with drift (or strain progression) until longitudinal bar yield. The presence of a yield plateau in longitudinal bars produced a significant rise in strain progression right after yielding of the longitudinal bars. Unlike

the other bars, column CM100 longitudinal bars did not have a yield plateau and did not experience a significant jump in the strain progression after reaching the defined yield point. Rather, the column CM100 strain progression increased gradually as the column was pushed to a higher drift past yield.

For columns 2L06, 2H06 and CS80 the increase in strain progression past yielding was not as significant as for columns CL100, CH100, and CH60. This was believed to be due to the debonding of the reinforcement from the concrete as indicated by the initiation of spalling at the drift of milestone SD1. The SD1 drift ratio of column CS80 occurred approximately at the time of longitudinal bar yielding. Damage milestones were not available for columns 2L06 and 2H06. The SD1 for 2L06 was inferred from the strain plot to occur around a drift ratio of 0.8% to 1.0% based on the column having the same bar yield strength and axial load ratio with column CH60. The SD1 milestone for 2H06 was assumed even at earlier drift ratio around 0.4% to 0.6% drift ratio based on CS60 SD1, which had a comparable high axial load ratio to 2H06. The strain in 2H06 is much lower from that of 2L06 as can be seen in Figure 3.34 and also appeared to reach yield at a later drift ratio, which may have been caused by high axial load ratio and earlier bar debonding. Column CS60 which had a relatively high axial load ratio and high shear stresses also showed the same trend with longitudinal bars partially debonding at an early drift and yielding at a higher drift. Bar debonding which decreased the strain progression was also observed on CL100, CH100, and CH60 after SD1. Spalling damage was therefore observed to be closely related to spalling and associated bar debonding, which decrease longitudinal bar strain demands in tension.

As discussed in section 3.4.1, the damage concentration is closely related with T/Y ratio which is also related to how far bar debonding spreads on the columns. Previous research (Berry and Eberhard, 2007) also stated that the strain of the longitudinal bar at the end of the column

decreased after the onset of spalling and the strain was distributed farther away from the section of maximum flexural demand. As could be expected, a lower value of the T/Y ratio appeared to concentrate strains after yielding as seen in comparing columns CL100 and CH100. The strain progression after debonding for bars with lower T/Y ratio values also appeared to be higher as seen in comparing the behavior of columns CL100, CH100 and CH60. It was therefore observed that the value of T/Y ratio is closely related with the strain demands in concrete columns.

4 ANALYSES AND RELATIONS

4.1 Introduction

The advent of performance-based earthquake engineering has increased the necessity of simulating the nonlinear response of a structural system under seismic events. Focusing on the acceptance criteria, standards have moved toward strain based acceptance criteria rather than displacement based acceptance criteria, especially the strain demands at the reinforcing bar. Uniform elongation and low cycle fatigue can be the controlling values that limit the allowable strain demand at the reinforcing bars. According to that, a model is proposed to predict the maximum strain demand in longitudinal bars during the seismic response for concrete columns.

4.2 Column Computational Model

A distributed plasticity, line-element model of the test columns was generated in OpenSees (OpenSees, Version 2.4.5, 2015). The analysis included second order P-Delta effects using the PDelta Transformation command in OpenSees. This type of model was selected as the starting point for the proposed model because it provides an estimate of longitudinal bar strains that intrinsically captures much of the effects of member geometry, reinforcing details, material properties, and the interactions between flexure and axial load. Figure 4.1 shows a schematic of the model. Initially, cyclic and pushover analyses were conducted on column models. However, results from pushover analyses are only presented, because the differences in global response and tension-strain response of the longitudinal bars between pushover and cyclic analyses were found to be insignificant. Pushover analyses were preferred to reduce computational cost. Additional detail and comparison plots between cyclic and pushover analyses can be found in Appendix F.

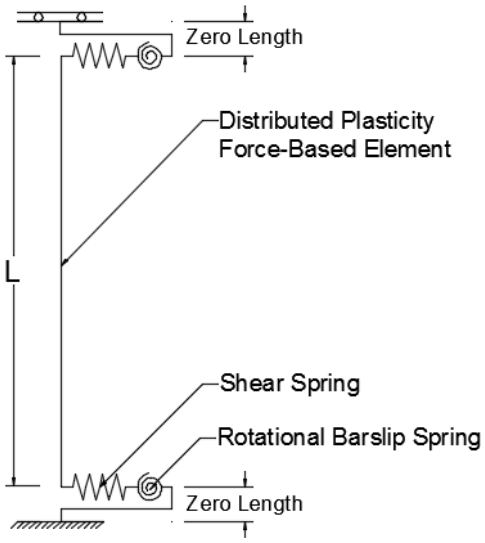

Figure 4.1 Schematic computational model of the column

4.2.1 COLUMN ELEMENTS

A distributed plasticity fiber-section force based formulation element was used to model the column flexural behavior (Spacone et al., 1996). This element is formulated with constant curvature between integration points, which generates constant strains around each integration point, unlike displacement-based elements which typically have linear curvature assumptions along the element. Additionally, one force-based element is sufficient to capture the column global deformation and strain demands in the nonlinear range of behavior, as opposed to requiring several displacement-based elements to achieve the same accuracy (Neuenhofer and Filippou, 1997; Scott and Fenves, 2006; Addessi and Ciampi, 2007). A lumped plasticity element was not chosen for the proposed model because lumped plasticity elements cannot capture local member deformations and do not provide a starting-point strain estimate for longitudinal bars.

4.2.2 ZERO LENGTH SHEAR AND ROTATIONAL SPRING

To model the shear deformation component, zero-length linear shear springs were introduced at both ends of the columns. Bar slip deformation was also modeled through a linear rotational

spring at both end of the column. A linear bar slip spring was used as opposed to a nonlinear one to avoid any localization of rotational deformations in the bar-slip or fiber element that are in series. The selected spring stiffnesses are presented in subsequent sections.

4.2.3 FIBER DISCRETIZATION

The column section was discretized into fibers modeling the cover concrete, core concrete, and steel reinforcement. The fiber section discretization scheme is shown in Figure 4.2 for a case with eight longitudinal reinforcement bars. Columns with twelve reinforcement bars used the same concrete fiber discretization but with twelve bar fibers. This discretization is recommended in the OpenSees online manuals for unilateral loading and similar fiber discretization was used successfully by many including Kaba and Mahin (1984).

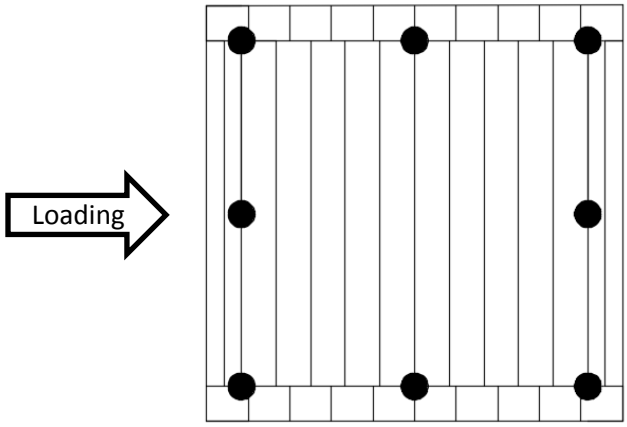

Figure 4.2 Column fiber section

4.2.3.1 Sensitivity of the Number of Concrete Fibers

Sensitivity analyses were conducted to determine the least number of concrete fibers required to capture column lateral response and provide a reasonable starting point for tension strains in longitudinal bars for all type of sections investigated in this study. The number of fibers affects computational time. Sensitivity analyses to global deformation and tensile strain on the

longitudinal bars were conducted for the number of core and side cover fibers (n) and the number of bottom and top cover fibers (m). Pushover loading was applied to the column models illustrated in Figure 4.1 in the sensitivity analyses. Reported here are the results of the sensitivity analyses conducted on column 2L06, which represents a tension controlled section, and column 2H06, represents a compression controlled section.

The of fiber numbers on column lateral response were conducted for a tension controlled section (column 2L06) using n = 1; 2; 4; 8; 10; 15; and 20 while m was maintained at a value of 1. The OpenSees output of lateral force versus drift ratio responses of the model for each number of n are plotted in Figure 4.3(a). It can be seen in this figure that the stiffness and capacity of the model converges at n greater or equal to 4. However, the responses softened at different rates for drift ratios above 3.5% for various n values. To adequately capture this softening, an n value of 10 was selected as it provided smoothest softening response (Figure 4.3(b)).

Then, using n = 10, the sensitivity analyses were conducted for m = 1; 2; and 4. The lateral response is plotted in Figure 4.4 and shows little difference for various m values.

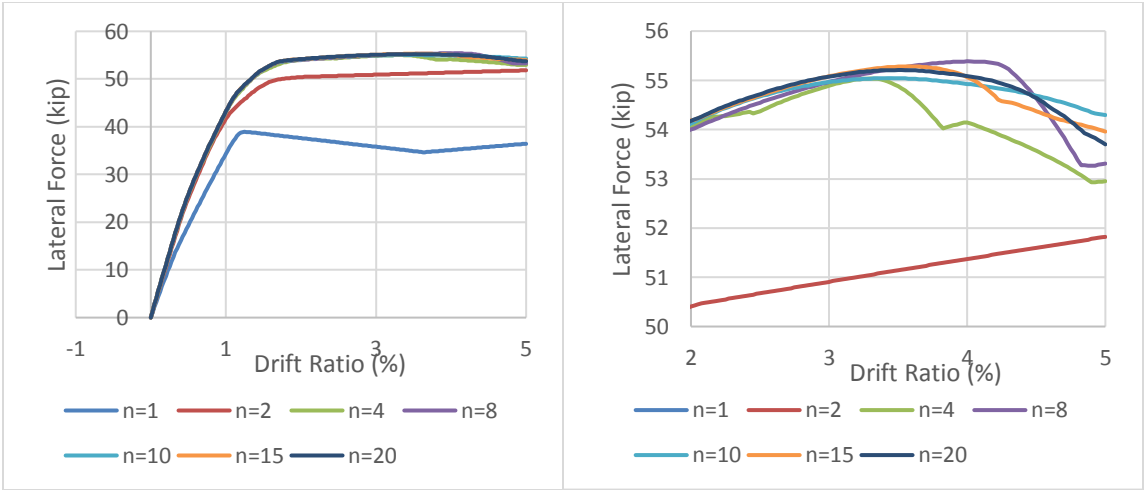

(a) (b)

Figure 4.3 (a) 2L06 global response sensitivity on n; (b) zoom in plot

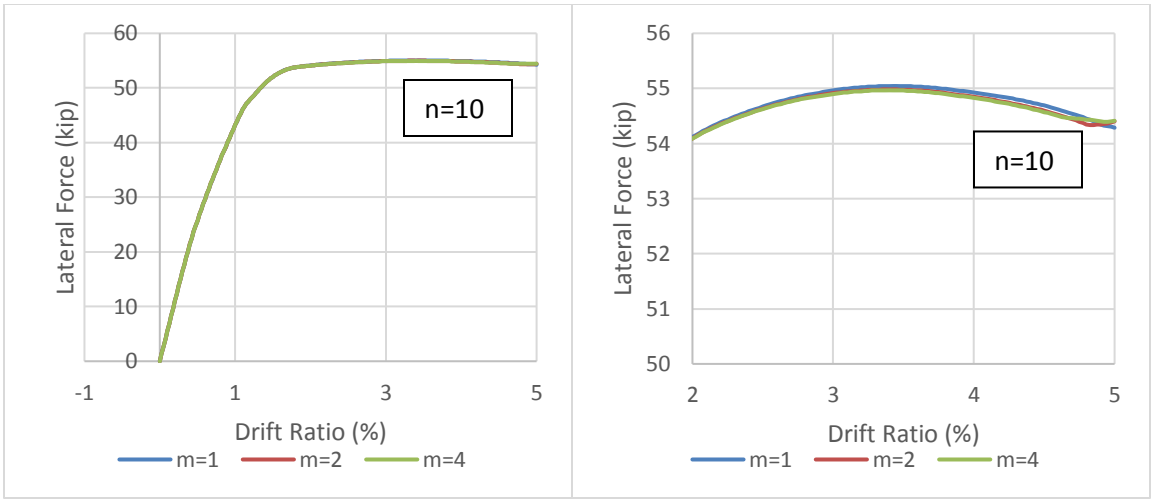

(a) (b)

Figure 4.4 (a) 2L06 global response sensitivity on m; (b) zoom in plot

Similar observations were made with respect to column lateral behavior for the compression controlled column 2H06 (Figure 4.5 and Figure 4.6)

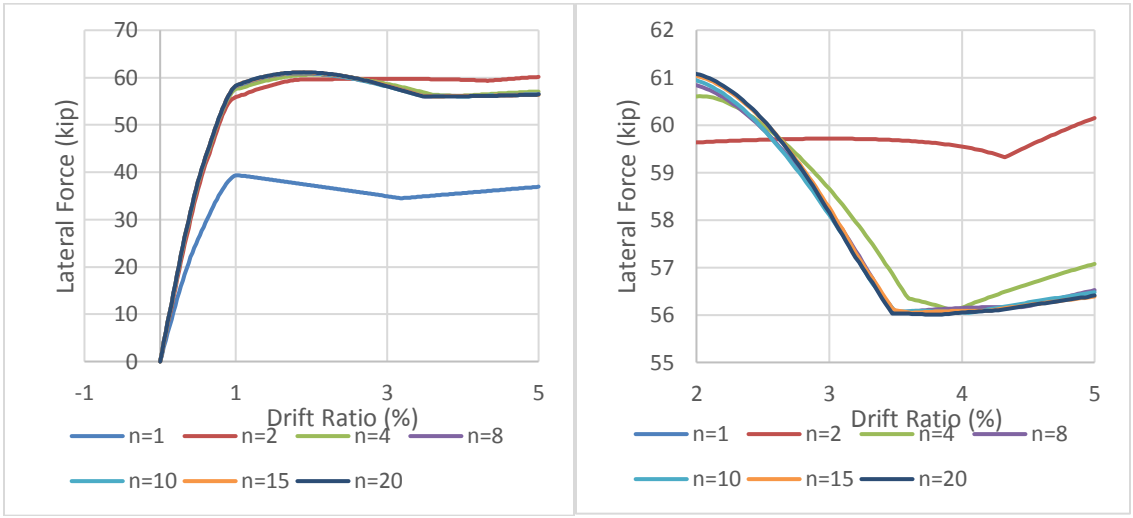

(a) (b)

Figure 4.5 (a) 2H06 global response sensitivity on n; (b) zoom in plot

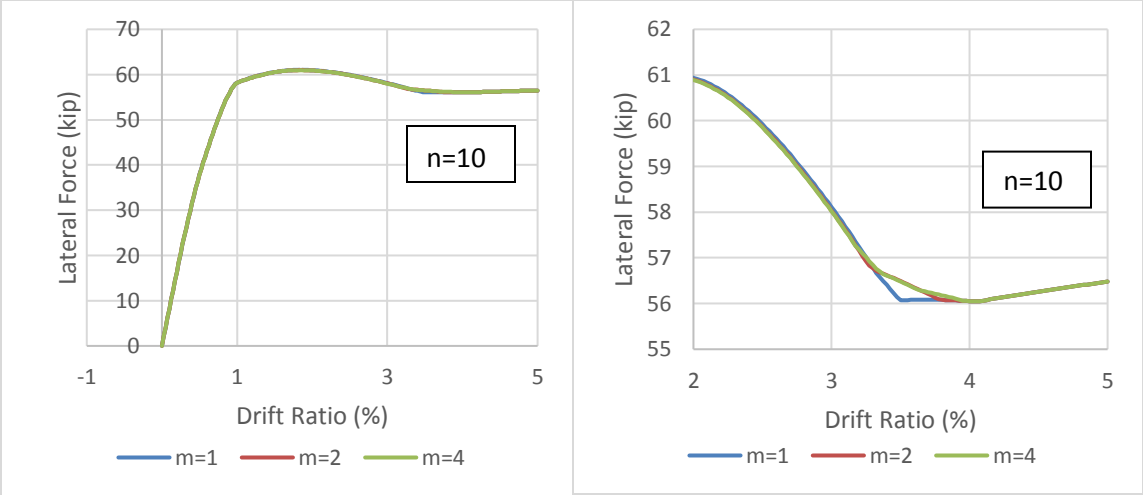

(a) (b)

Figure 4.6 (a) 2H06 Global deformation sensitivity on m; (b) zoom in plot

The sensitivity of fiber numbers on tension strains in longitudinal bars was also investigated for both tension and compression controlled sections (column 2L06 and column 2H06, respectively). The OpenSees output of tension strains versus lateral drift ratio for each value of n are plotted for each section in Figure 4.7 and Figure 4.8. From those two figures, it can be concluded that tension strains converged for n greater or equal to 4. However, based on the lateral response sensitivity analyses as value of n = 10 was selected for all subsequent analyses and recommended for use when estimating bar strains in concrete columns.

Furthermore, the tension-strain sensitivity analyses were conducted with the recommended value of n = 10 and for m = 1;2 and 4 for both sections (Figure 4.9 and Figure 4.10). The results show virtually no differences on the tension strain. A value of m=2 was selected for subsequent analyses.

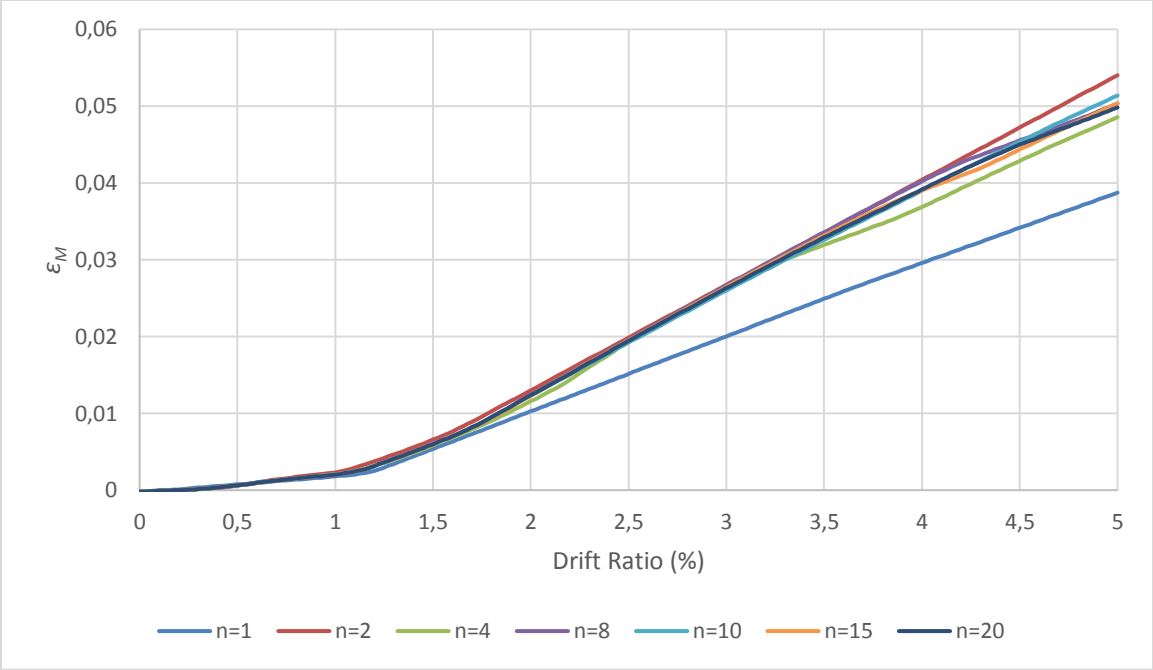

Figure 4.7 2L06 strain sensitivity on n

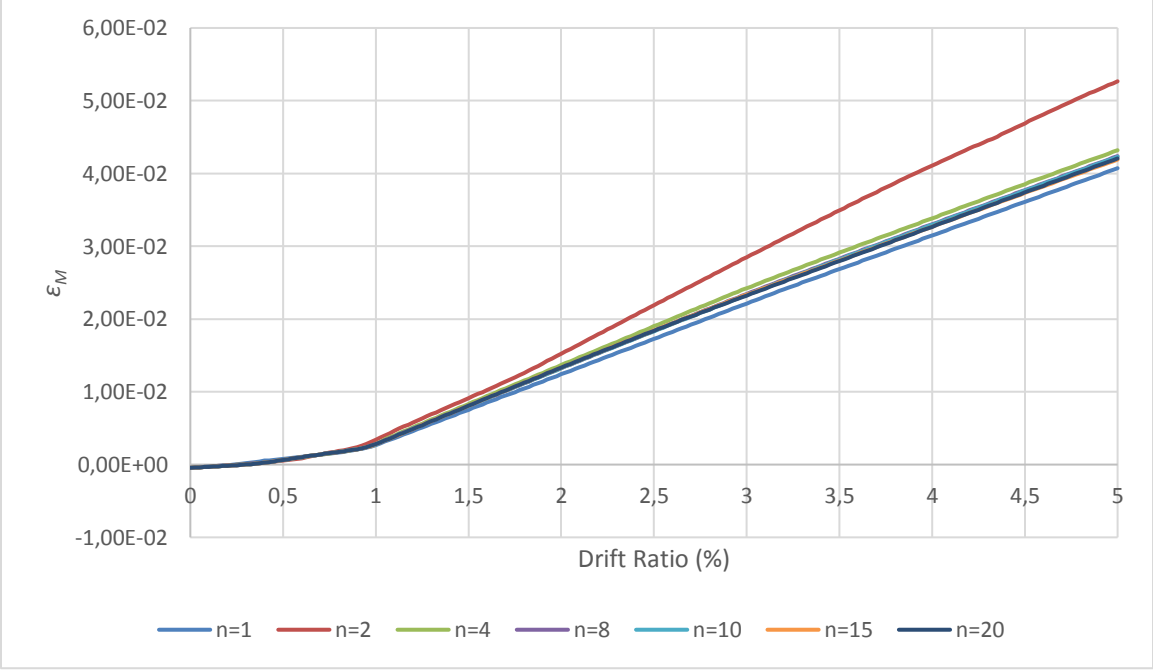

Figure 4.8 2H06 strain sensitivity on n

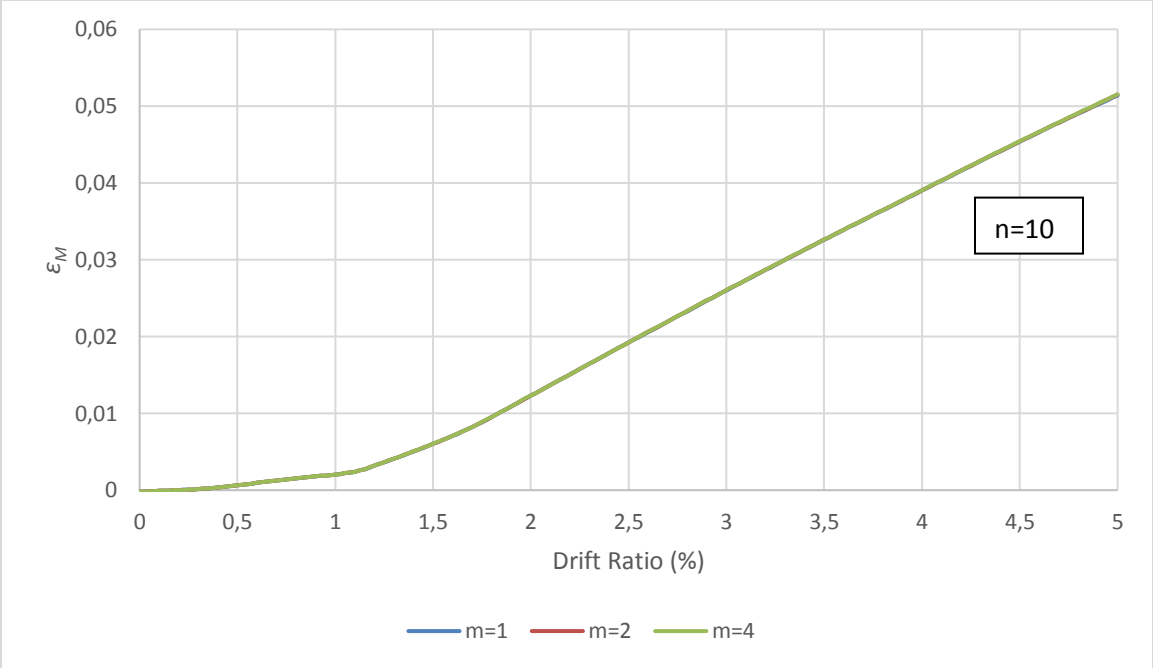

Figure 4.9 2L06 strain sensitivity on m

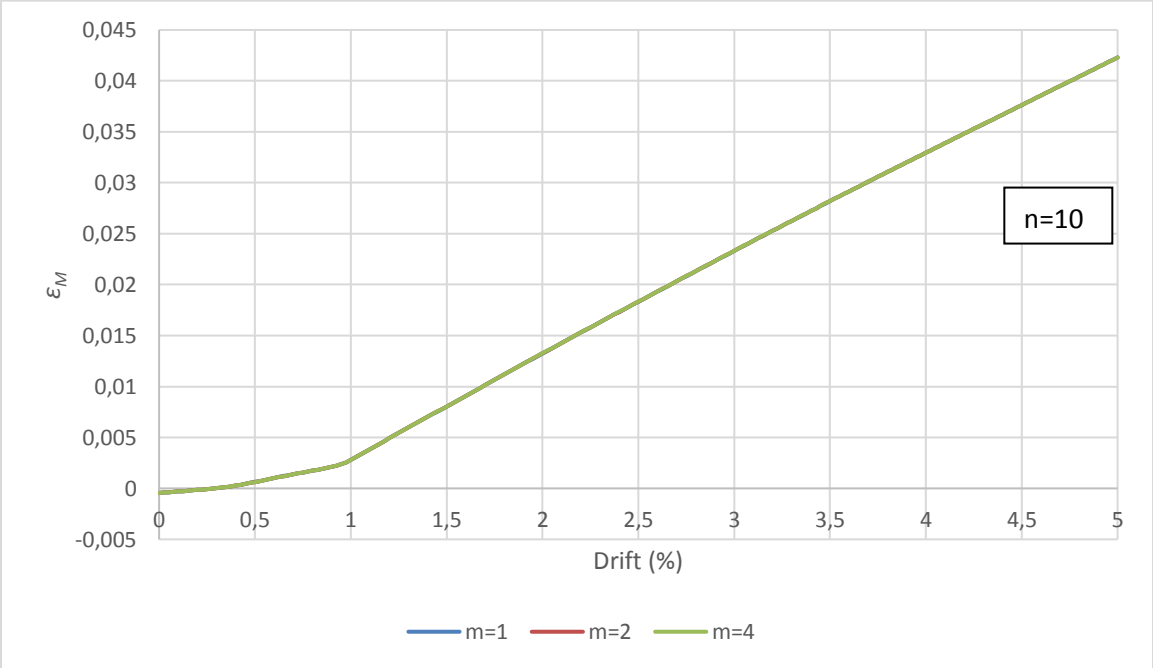

Figure 4.10 2H06 strain sensitivity on m

4.2.4 CONCRETE MATERIAL MODEL

4.2.4.1 Cover Concrete

The stress-strain response of cover concrete was modeled with the Concrete02 material model in OpenSees. The Concrete02 material model is constructed by Kent-Park (1971) concrete stress-strain model. In this section, five integration points force-based beam column element was used for fracture energy evaluation, which based on the results of an integration point sensitivity study presented later in the thesis. Because localization of deformations during softening sectional response occurs in force-based elements, the stress-strain response needed to be regularized by maintaining a constant energy release after strain-softening of the cover concrete response initiates (Coleman and Spacone, 2001).

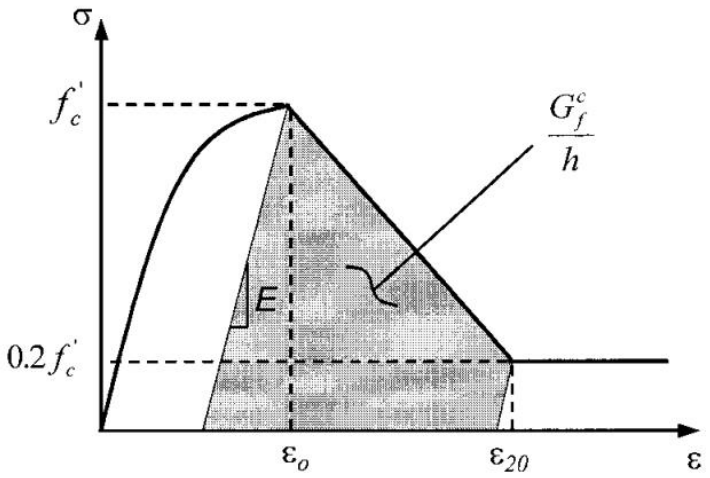

Figure 4.11 Kent-Park (1971) stress-strain model with fracture energy compression as shaded area

For that reason, the softening branch after the concrete reach the maximum stress ($f'c$) need to be regularized by adjusting the strain at which the concrete stress drops to 20% of $f'c$ in the softening branch. To maintain constant fracture energy, the strain value at 20% $f'c$, labeled as ε_{20} , was calculated with the following expression

$$\varepsilon_{20} = \frac{G_f^c}{0.6f'c\ Lp} - \frac{0.8\ f'c}{E_c} + \varepsilon_0 \quad (4\text{-}1)$$

where G_f^c is the constant fracture energy, E_c is the modulus of elasticity of concrete, ε_0 is strain at peak stress, L_p is plastic hinge length. The plastic hinge length is equal to the weighted length for the first integration point in the force-based element. The constant fracture energy can be calibrated based on experimental testing. The fracture energy values obtained from cylinder test of plain concrete usually vary from 0.114 kip/in. to 0.171 kip/in (Jansen and Shah, 1997). Concrete well confined by steel hoops may have a much higher fracture energy. Spacone and Coleman (2001) assumed the fracture energy value equal to 1.026 kip/in. The higher value of fracture energy (G_f^c) in regularization Eq. 4-1 will result in higher strain (ε_{20}) when concrete reaches 20% $f'c$. Higher values of ε_{20} or G_f^c result in a less softening slope in the lateral response of the column as shown in Figure 4.12. The sensitivity analyses of all the column specimens with varying value of G_f^c suggested that G_f^c=0.342 kip/in. was the best value to capture the softening slope of the column lateral response. Therefore, the recommended value of constant fracture energy is 0.342 kip/in.

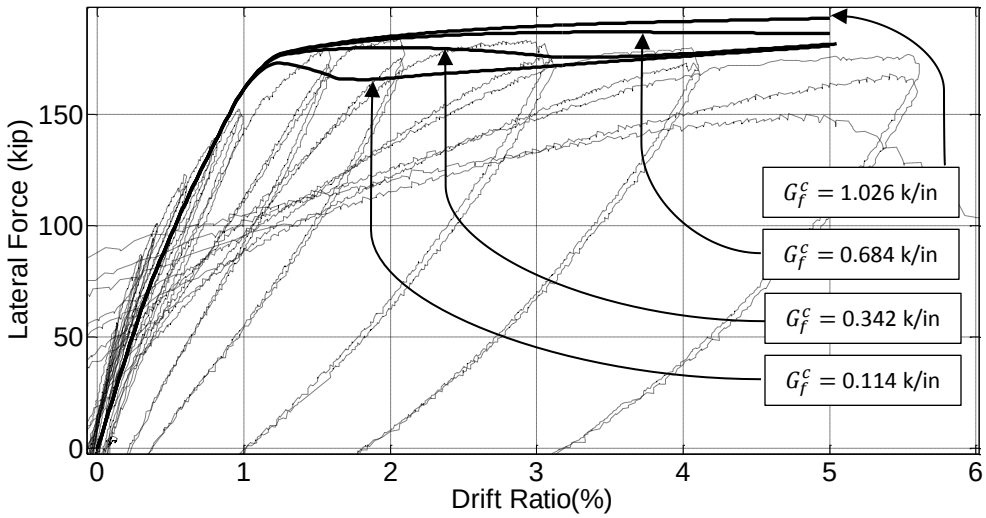

Figure 4.12 CS80 lateral response sensitivity to G_f^c

A sample calculation using Eq. 4-1 for column CL100 with G_f^c=0.342; $f'c$=-5110 psi; E_c =4075 ksi; ε_0=-0.0027 (based on previous research with bigger experiment data (Ghannoum et al., 2008)); and Lp=5.4 in. is presented below. Lp is the plastic hinge length which is the length of the first integration point weight times the length of the element. For five integration points using the Gauss-Lobatto integration scheme, the weight for the first integration point is 0.05L.

$$\varepsilon_{20} = \frac{G_f^c}{0.6 f'c\ Lp} - \frac{0.8\ f'c}{E} + \varepsilon_0$$

$$\varepsilon_{20} = \frac{0.342}{0.6\ (-5.11)\ 5.4} - \frac{0.8\ (-5.11)}{4075} + (-0.0027) = -0.02235$$ (negative in comprssion)

The result of the regularized concrete model was compared with the result from three concrete cylinder tests for column CL100 (Figure 4.13).

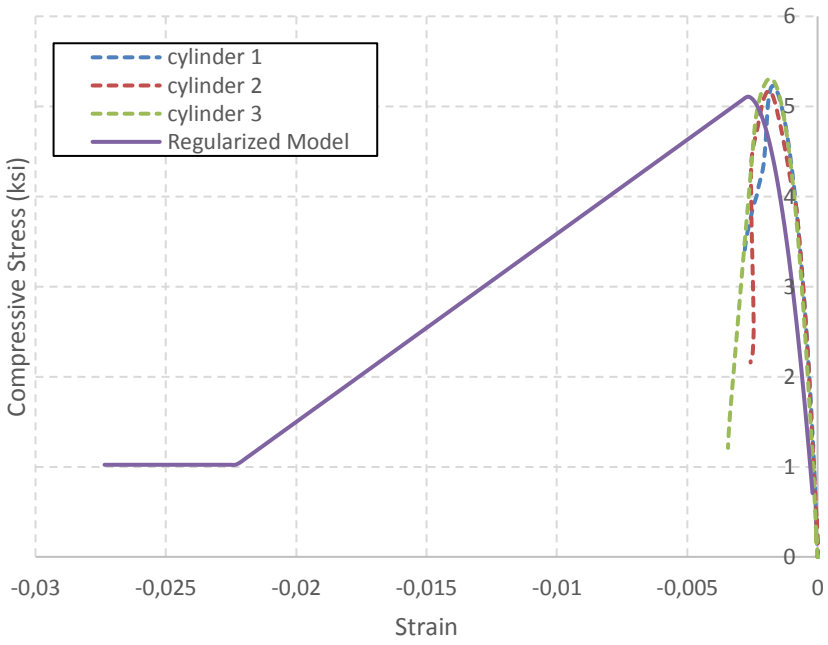

Figure 4.13 Comparison between cylinder test and regularized model of column CL100

The tension model for cover concrete in concrete02 also has a tension stiffening effect which is plotted in Figure 4.14 for column CL100. The kink near the peak tension stress was caused by a not small enough step size to capture the peak stress. The degrading slope (Et) was defined as 10% of tangent stiffness of concrete material at zero load. Tangent stiffness of concrete material at zero load given by 2($f'c/\varepsilon_0$) in the Concrete02 material. The tension strength (ft) was based on Eq. 19.2.3.1 per ACI 318-14 and was calculated as:

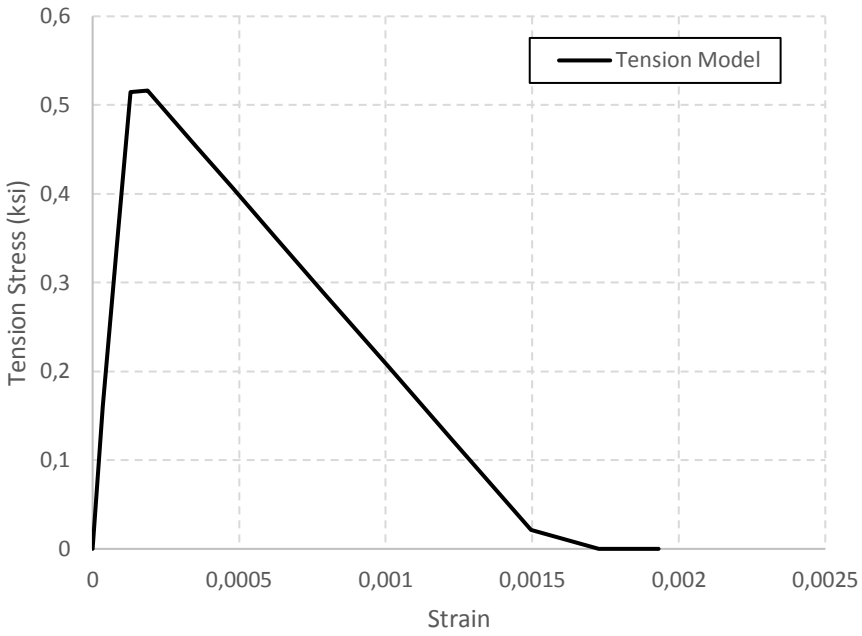

Figure 4.14 Tension model of cover concrete of column CL100

4.1.1.1 Core Concrete

Core concrete stress-strain response was modeled based on Mander confined concrete model (Mander et al., 1988). For modeling purpose, core concrete was modeled with Concrete04 material model in OpenSees by matching the stress-strain value at the maximum stress to Mander confined concrete model. The strain at crushing of the Concrete04 material model was modelled with empirical maximum strain equation introduced by Qi and Moehle (Qi and Moehle, 1991). The comparison between cover concrete model and core concrete model of CS80 column is shown in Figure 4.15. The tension concrete model of the Concrete04 material of column CS80 is shown in Figure 4.16. The kink near the peak tension stress was caused by not having a small enough step size to capture the peak stress. The ultimate tensile strain of concrete was calculated as 2(ft/Et) as recommended by OpenSees.

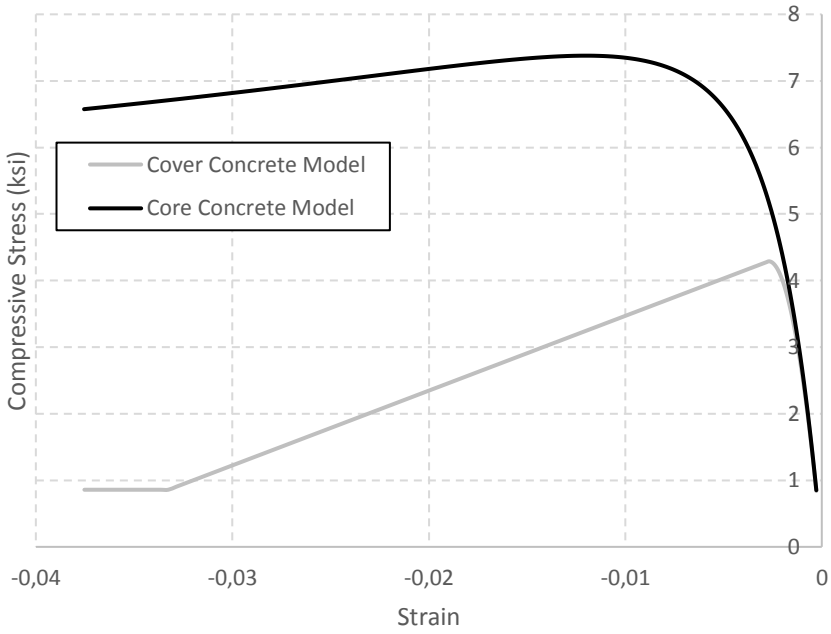

Figure 4.15 Comparison between core and cover concrete model

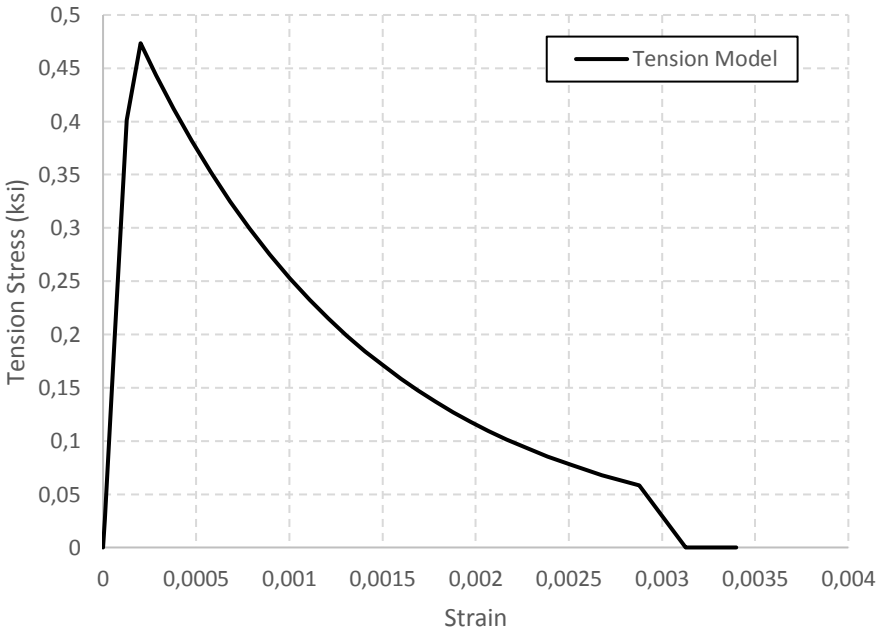

Figure 4.16 Tension model of cover concrete of column CS80

4.1.2 STEEL MATERIAL MODEL

The stress-strain response of the reinforcing bar was modeled with the steel02 material model in OpenSees. The steel02 material model is based on the Giuffre-Menegotto-Pinto (1972) steel material model with isotropic strain hardening. The steel02 material model was used because the model is commonly used and available both in commercial and research software. An attempt to compare the steel02 and the Reinforcing Steel material, which has a curvilinear hardening form, was made and it was found that the differences in responses were insignificant as demonstrated in Appendix G. The strain hardening ratio (b) which is the ratio between post-yield tangent stiffness and initial elastic stiffness was calculated from the steel material properties data based on Table 3-4. The strain hardening ratio (b) can be calculated with the following expression:

$$b = \frac{f_y\left[\left({}^{T}/_{Y}\right) - 1\right](ksi)\Big/(uniform\ elongation - \varepsilon_y)}{29000} \tag{4-2}$$

The results of the Eq. 4-2 calculation are presented in Table 4-1. The comparison between the steel material model and a coupon test representing a longitudinal bar of column CH100, which exhibited a yield plateau, is shown in Figure 4.17. Figure 4.18 shows the same comparison for a coupon test representing the longitudinal bars of Grade100 A1035 that do not have a yield plateau. The values of b presented in Table 4-1 are consistent with the previous research that recommended a value around 0.01 for grade 60 bars (Berry and Eberhard, 2007).

Table 4-1 Strain hardening ratio variable for Steel02

Column	b
2L06	0.0100*
2H06	0.0100*
CS60	0.0096
CS80	0.0109
CL100	0.0071
CH100	0.0128
CM100	0.0258
CH60	0.0086

**selected based on recommendation from Berry and Eberhard (2007) due to lack of information on uniform elongation*

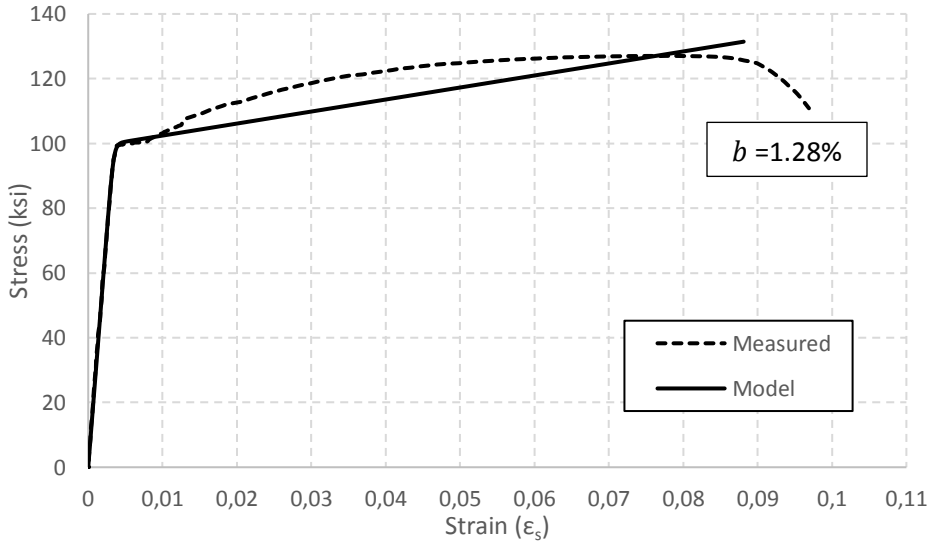

Figure 4.17 Comparison of CH100 steel material model to coupon test measurement

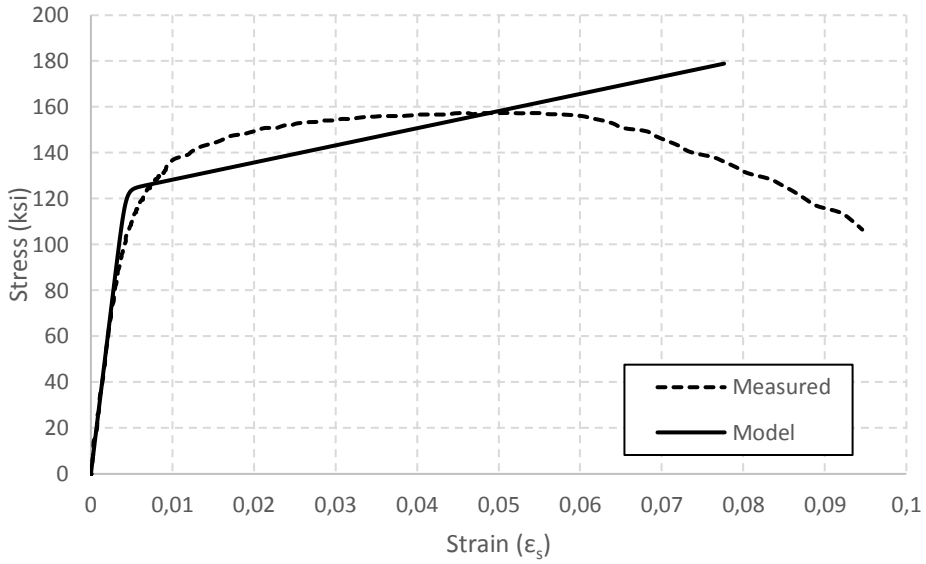

Figure 4.18 Comparison of CM100 steel material model to coupon test measurement

4.3 Flexural Deformation

The flexural deformation component was modeled using a distributed-plasticity, force-based (flexibility-based), fiber beam-column element. A fiber beam-column element is a line element with a fiber-section assigned at each integration point. The moment curvature response at each integration point is determined by the fiber-section assigned. A force-based formulation always satisfies equilibrium along the length of the element. Equilibrium is satisfied by the force interpolation functions. Deformations along the length of the element are obtained by weighted integration of the fiber-section deformations (Spacone et al., 1996).

Inelastic deformations in reinforced concrete columns typically occur in the end sections of the columns. On account of that, a Gauss-Lobatto integration scheme is used in the element since it has integration points at the ends of the element which coincide with the sections of highest inelastic deformation.

4.3.1 SENSITIVITY OF THE NUMBER OF INTEGRATION POINTS

In this section, the sensitivity of the number of integration points on flexural deformations is presented.

The Gauss-Lobatto integration method is a numerical integration approximation of the definite integral of a function, which is evaluated as the sum of weights multiplied by function values at the integration points within the domain of integration. The Gauss-Lobatto integration method matches the exact results of polynomials of degree 2N-1 (with N being the number of integration points). Thus, the Gauss-Lobatto integration method has a specific weight and integration point locations for each number of integration points (N) to match exactly the polynomials of degree 2N-1.

However, local flexural deformations along the length of reinforced concrete columns do not follow any polynomial function because of cracks, damage, and inelastic deformation that occur along the length of a column. Therefore, deformation delivered by a Gauss-Lobatto intergration scheme for fiber-section curvatures can only approximate the actual distribution of flexural deformations along a column length.

Global flexural deformations obtained by using various numbers of integration points are plotted for columns CH100 and CS80 in Figure 4.19 and Figure 4.20 respectively. The flexural deformations that are shown in this section were obtained by running the pushover analyses on column models. The backbones for the measured experimental flexural drift ratios (DR_{flex}) were drawn between points at the end of the first cycle at each target drift.

Both Figure 4.19 and Figure 4.20 show that three integration points are not sufficient to predict accurately the flexural deformation after the cracking moment is reached. The results for four to seven integration points are reasonably accurate at most force levels before significant inelastic

deformations occur. However, four integration points provide less accurate result at some force levels that the higher numbers of integration points (Figure 4.21 and Figure 4.22). As the number of integration points increases, so does the hardening of the column elements in the inelastic range. This is due to the increased concentration of curvatures at the end section with increased integration points, which drives higher strain in the steel fibers and associates increased strength for a given global deformation.

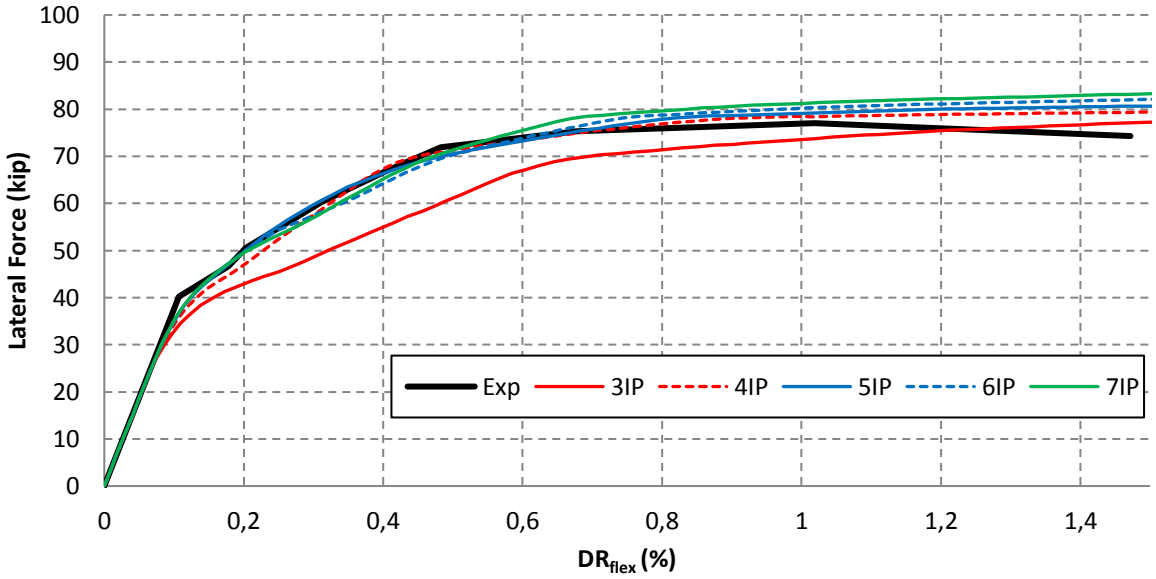

Figure 4.19 CH100 flexural deformation with 3 to 7 integration point

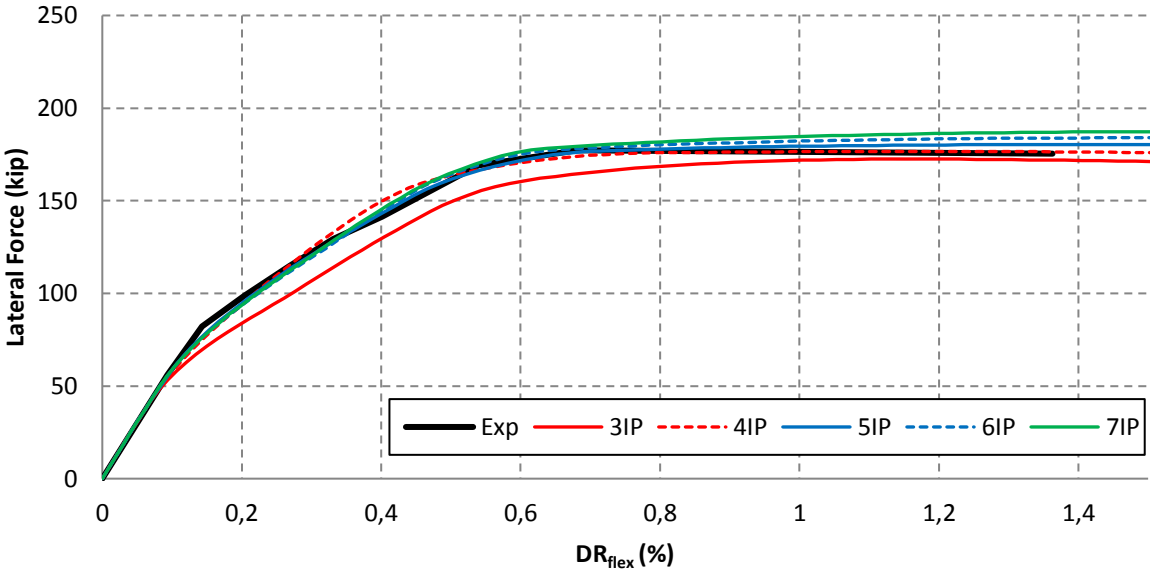

Figure 4.20 CS80 flexural deformation with 3 to 7 integration point

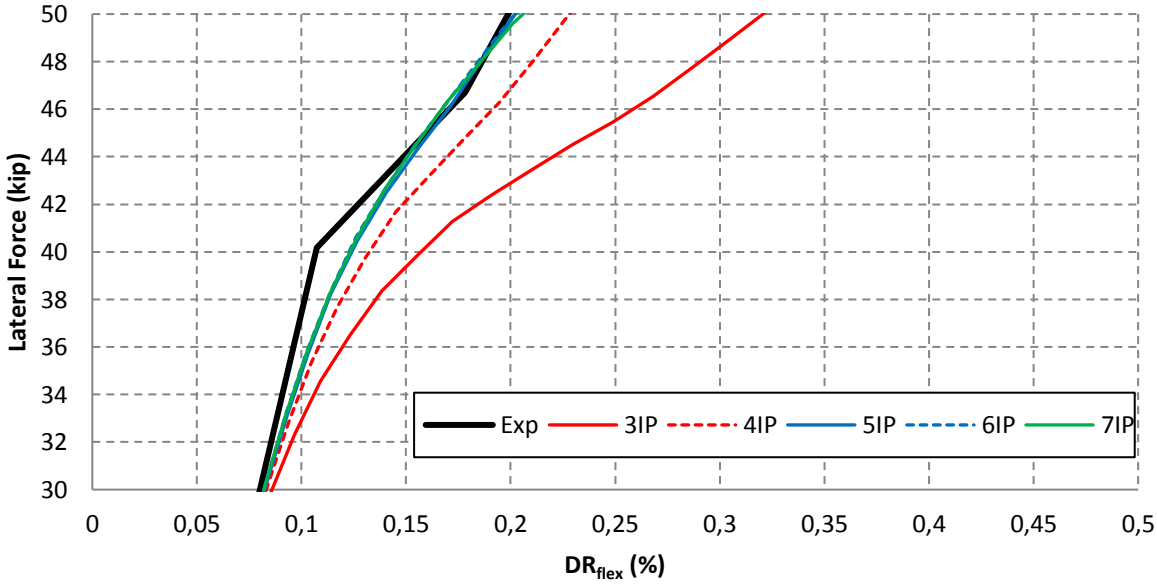

Figure 4.21 Zoom in of CH100 flexural deformation with 3 to 7 integration point

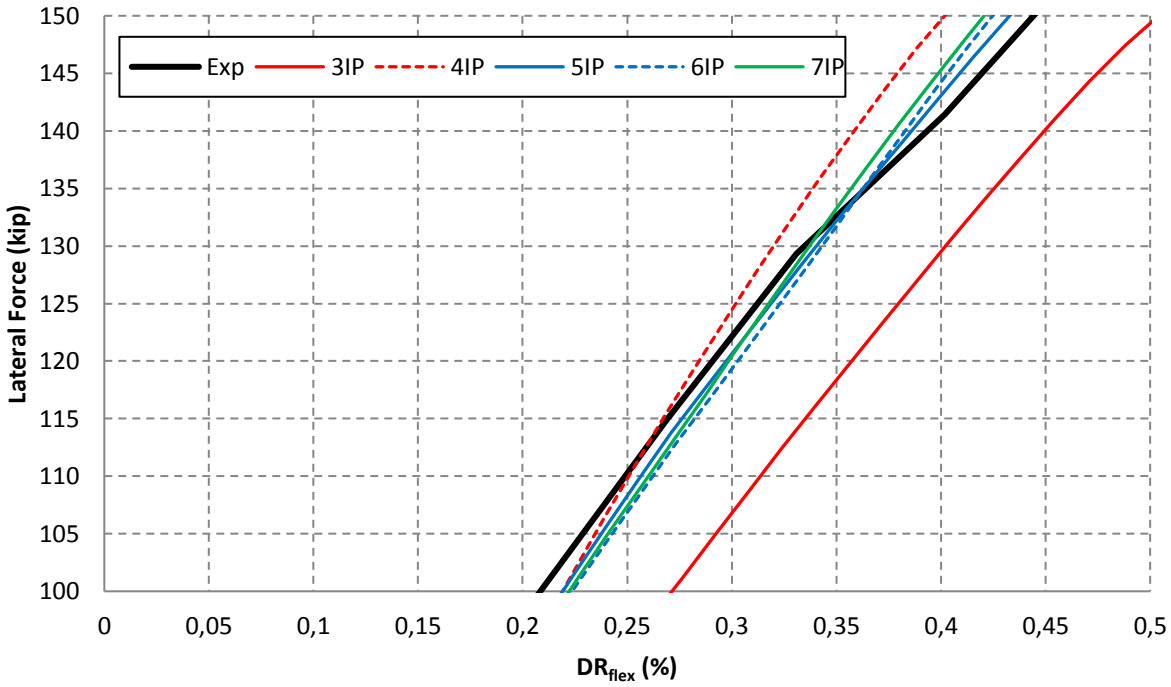

Figure 4.22 Zoom in of CS80 flexural deformation with 3 to 7 integration point

The errors between the model and experimental flexural deformations were tabulated to help select the optimal number of integration points. The errors were evaluated at two force levels: first yield and at 80% of that value. First yield was taken as recommended by Benzoni et al. (1996) as the first point at which the tension reinforcement yielded or the maximum concrete compressive strain reached a value of 0.002. The errors were calculated as follows:

$$error = \frac{\Delta_{measured} - \Delta_{estimated}}{\Delta_{measured}} \times 100\% \qquad (4\text{-}3)$$

The error results at the yield force and 0.8 of the yield force are represented in Table 4.2 and Table 4-3 respectively. Based on those two tables, five Gauss-Lobatto integration points produced the smallest number integration point with the overall smallest error for all columns. Thus, five integration points are recommended to be used in the force-based line element for double

curvature rectangular column to capture flexural deformation accurately and was used in this study for the rest of the estimated results. The estimated flexural deformations using five integration points are presented in Appendix B for all columns.

Table 4-2 Error at yield force

IP	2L06	2H06	CS60	CS80	CL100	CH100	CM100	CH60
3	23.0%	41.6%	7.7%	27.2%	43.4%	47.5%	34.9%	46.1%
4	-4.4%	21.4%	-11.1%	1.8%	-4.4%	-1.6%	-10.8%	2.6%
5	**-1.1%**	**16.4%**	**-8.9%**	**3.9%**	**-3.4%**	**-4.0%**	**-11.8%**	**-7.3%**
6	1.3%	17.5%	-7.8%	6.2%	5.3%	7.1%	-2.1%	-4.1%
7	0.3%	17.8%	-8.6%	5.3%	1.8%	3.6%	-4.9%	-0.5%

Table 4-3 Error at 0.8 yield force

IP	2L06	2H06	CS60	CS80	CL100	CH100	CM100	CH60
3	24.6%	63.5%	16.3%	33.9%	52.1%	57.5%	54.8%	27.6%
4	0.2%	51.8%	-0.3%	12.0%	7.0%	11.7%	8.4%	2.0%
5	**-1.7%**	**48.5%**	**-1.6%**	**9.3%**	**-4.2%**	**-0.6%**	**-4.1%**	**-6.5%**
6	0.2%	47.2%	-0.3%	10.9%	-2.2%	0.0%	-3.1%	-7.2%
7	-0.4%	48.0%	-0.5%	10.9%	1.4%	2.5%	0.3%	-7.3%

4.4 Shear Deformation

The column deformation due to shear was relatively small for most columns. If considered at all, shear deformations are often modeled according to elastic theory and idealized as homogeneous, isotropic material with a constant, reduced shear modulus. In this study, the shear deformation was modeled as a lumped shear deformation at the ends of the column represented as shear spring with elastic stiffness given by

$$k_{shear} = \frac{(5/6)GA_g}{L} \tag{4-4}$$

$$G = \frac{E_c}{2(1+\upsilon)} \tag{4-5}$$

where G is shear modulus, A_g is gross section area, L is the column length. E_c is the concrete material elastic modulus and is given by 57,000$\sqrt{f'c}$ psi. υ is concrete Poisson ratio (taken as 0.25). The measured shear deformation (DR_{shear}) was constructed as the backbone curve of the cyclic shear deformation component . The comparison of estimated and measured results are shown in Figure 4.23 and Figure 4.24. The estimated shear deformation shows a stiffer behavior than the measured shear deformation for CS80 and CH100 column. The rest of column shear deformation are presented in Appendix B.

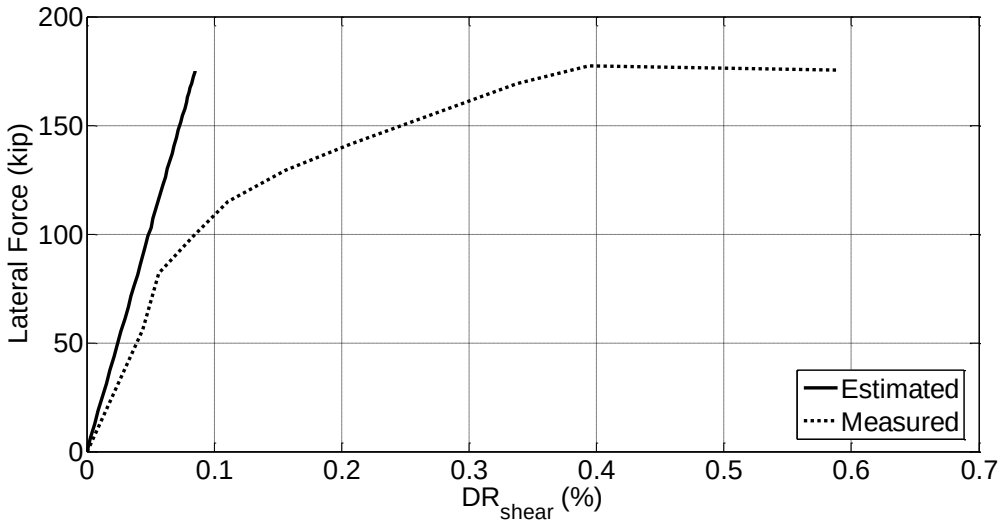

Figure 4.23 CS80 shear deformation

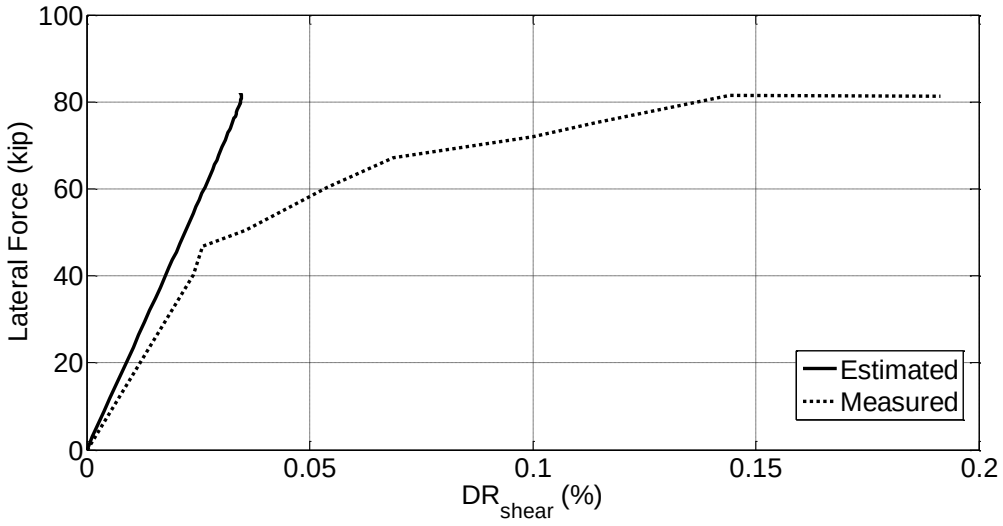

Figure 4.24 CH100 shear deformation

4.5 Bar Slip Deformation

Bar slip deformations are introduced through a linear relation between rotational slip and moment in the zero-length rotational springs. Based on Harajli (2009), bar slip deformations stay fairly elastic when damage/cracks do not occur in the concrete, which is a reasonable assumption for the footings of the columns that sustained only minor cracking. An effective linear bar slip stiffness was also used by Berry and Eberhard (2007) and Elwood and Eberhard (2009). Assuming a uniform bond stress between bars and adjacent concrete, and that bar slip rotation occur around the flexural neutral axis of the section (Sokoli et al., 2014), this relation for the rotational stiffness of the bar slip rotational spring can be derived:

$$k_{slip} = \frac{8u\ M_y}{d_b f_s\ \phi_y} \tag{4-6}$$

where u represents the constant bond stress between bars and adjacent concrete, M_y represents moment at first yield, ϕ_y represents the section's curvature at first yield, d_b represents longitudinal bar diameter, f_s represents longitudinal bar stress at first yield.

M_y and ϕ_y as well as f_s can be estimated from moment curvature analyses Those parameters are typically estimated accurately and have been verified experimentally (Sokoli et al., 2014). However, recommendations for the constant bond stress parameter vary greatly and depend on many factors, including whether the longitudinal bars are anchored in footings or in beam-column joints. To overcome the uncertainty in the constant bond stress value, the constant bond stresses were calibrated at first yield based on the measured bar slip deformation component (Figure 4.25). The measured bar-slip deformation (DR_{slip}) was constructed as the backbone curve of the cyclic bar-slip deformation component. The calibrated constant bond stress parameters are summarized in Table 4-4 as a function of the square root of the concrete compressive strength. The remainder of the column bar slip deformation plots are presented in Appendix B.

In subsequent analyses, the calibrated elastic stiffnesses are used for the bar-slip springs.

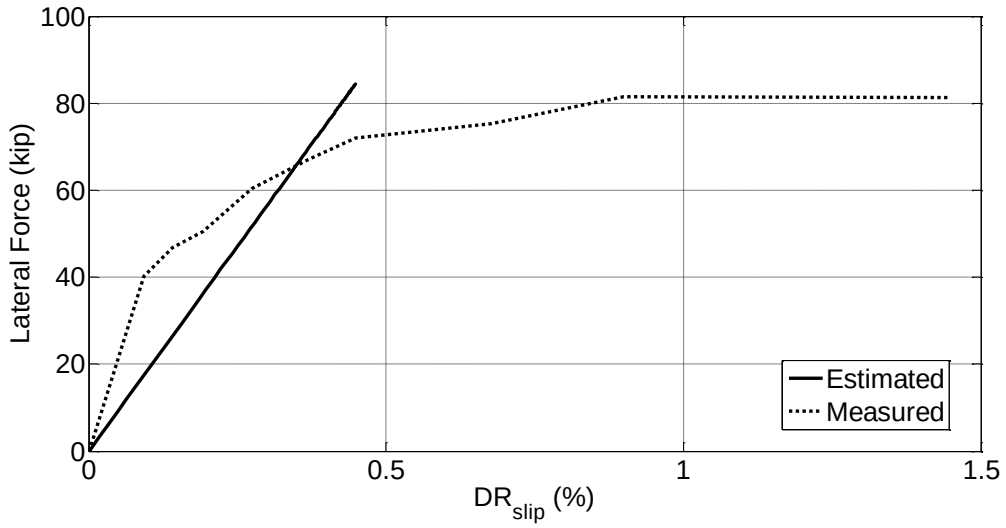

Figure 4.25 CH100 barslip deformation

Table 4-4 Calibrated bond stress

Column	Bond Stress (u) (psi)
2L06	$17.00\sqrt{f'c}$
2H06	$9.00\sqrt{f'c}$
CS60	$13.50\sqrt{f'c}$
CS80	$13.25\sqrt{f'c}$
CL100	$18.00\sqrt{f'c}$
CH100	$11.50\sqrt{f'c}$
CM100	$15.00\sqrt{f'c}$
CH60	$13.75\sqrt{f'c}$

4.6 Total Drift

Due to the use of simplified elastic relations for bar slip and shear deformations, the estimated drift before the first yield was typically slightly larger than the measured column global lateral drift, as shown in Figure 4.26. Nevertheless, the estimated total drift before the first yield happens is still acceptable and represents the measured stiffness after softening occurred due to cycling and past the point of first yield. Global drift for all columns are presented in Appendix B.

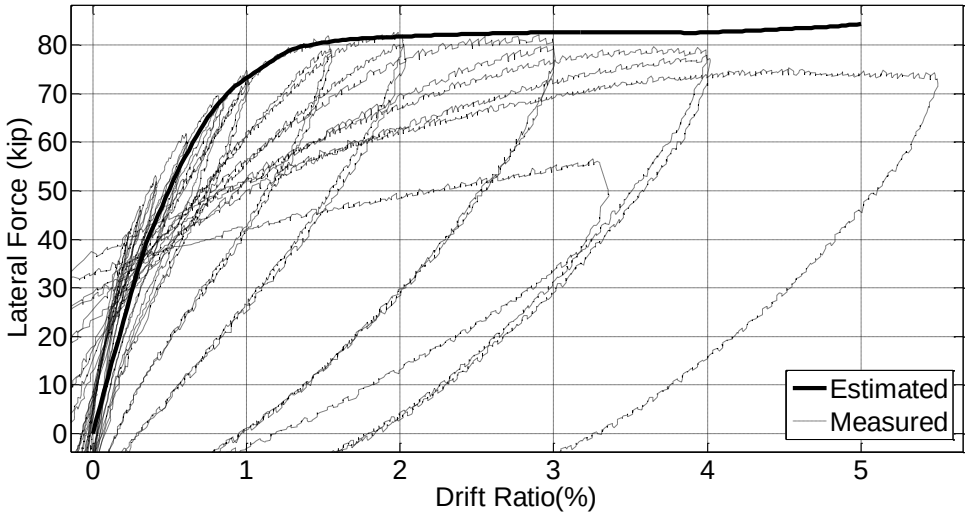

Figure 4.26 CH100 total deformation

4.7 Longitudinal Bar Strain

4.7.1 SENSITIVITY OF THE NUMBER OF INTEGRATION POINTS

Previous studies have indicated that curvature tends to localize in force-based beam-column elements at the integration point where flexural demands are highest when perfectly plastic or softening cross-sectional responses occur (Coleman and Spacone, 2001). Such localization can affect the global element stiffness and lateral deformation response (as seen in Section 4.2.4.1), as well as the curvature and strain demands at the critical integration point. To illustrate the strain localization in force-based beam-column elements, the strain responses of the outermost longitudinal bars obtained using various numbers of element integration points, are presented in Figure 4.27 to Figure 4.30. The models used in this analysis consisted of the Gauss-Lobatto force-based fiber beam column element with elastic rotational springs and elastic shear springs at both ends. The elastic rotational spring stiffness was determined in accordance with Eq. 4-6 with the calibrated bond stress (u) parameters provided in Table 4-4 that differed for each column. The elastic shear springs were assumed to have an elastic shear stiffness as stated in Eq. 4-5.

As can be seen in Figure 4.27 to Figure 30, the strain in longitudinal bars indeed localized significantly after yielding as the number integration points increased. The first integration point has a finite length proportional to the integration weight times the length of the element. Therefore, larger numbers of integration points generate smaller first integration weight (or length) where the plasticity is concentrated. This results in larger strains due to larger curvatures.

Five integration points were recommended to capture the global deformation accurately (Section 4.3). From Figure 4.37 to Figure 4.30, it also appeared that five integration points deliver the least amount of errors in strains before spalling triggers bar debonding. For these reasons, five integration points are recommended per element to simulate the global column behavior and estimate the strains in longitudinal bars. When columns experience spalling and associated bar debonding, the fiber-section strain results become less reliable. This is because the fiber-section analyses assume perfect bond between bars and concrete. In subsequent sections, an adjustment factor is proposed to modify the strains obtained from the five integration-point computational model after the initial hairline spalling crack occurs.

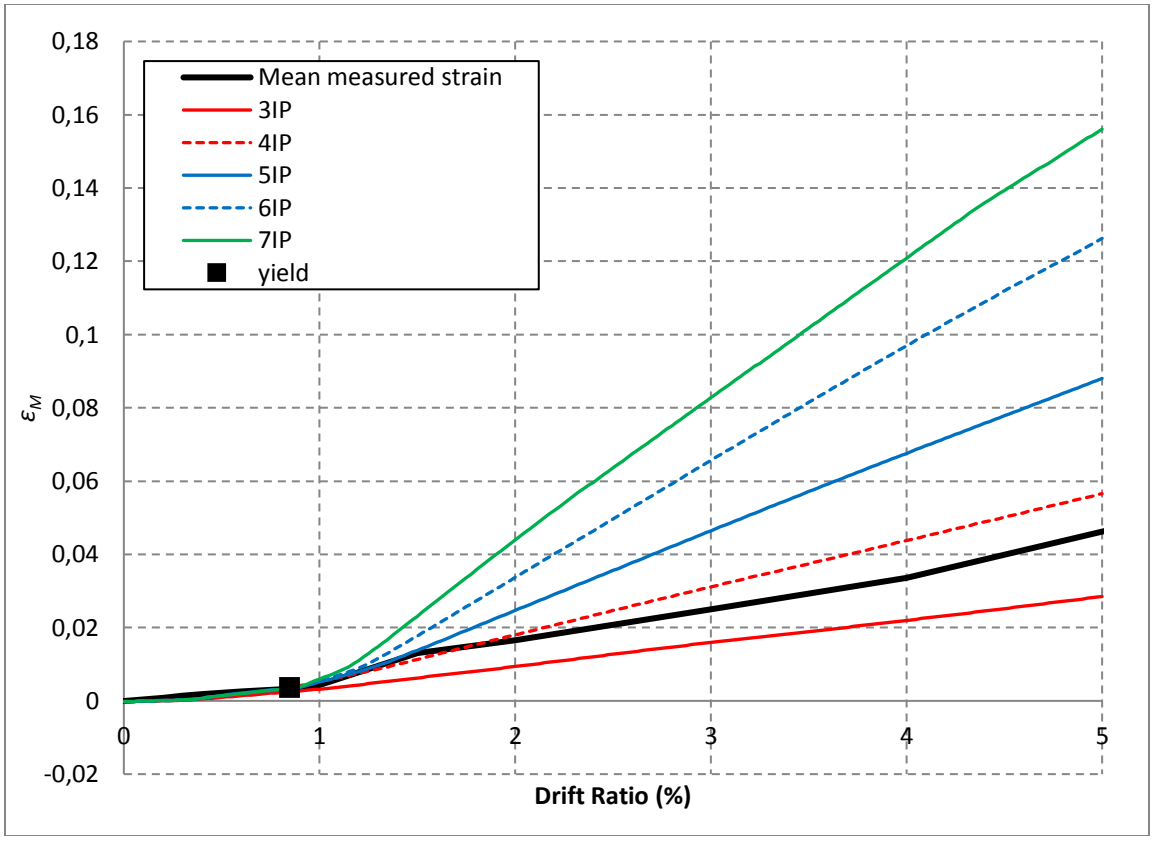

Figure 4.27 CH100 longitudinal bar Strain vs drift ratio sensitivity

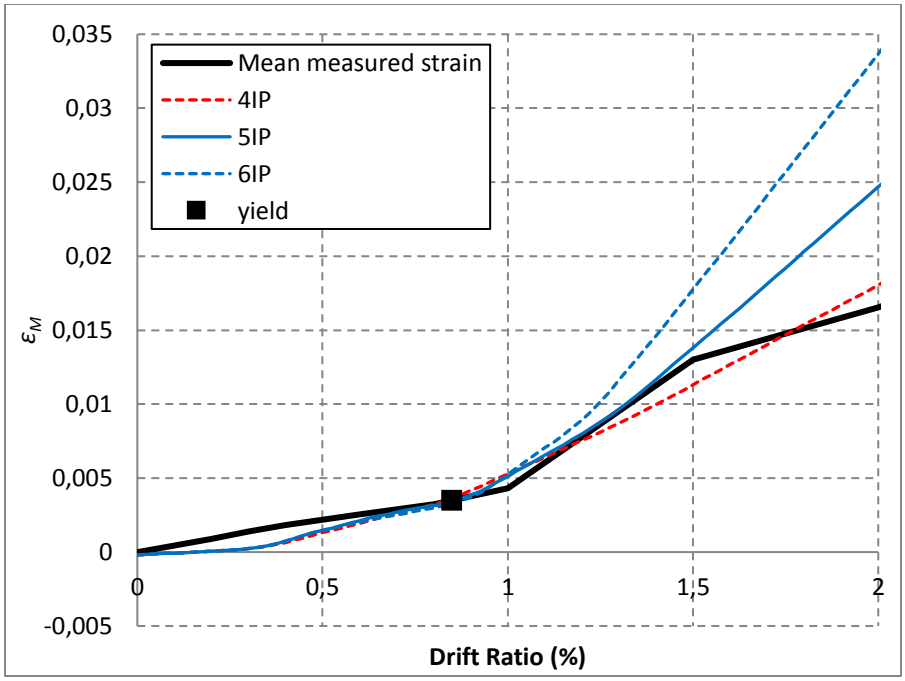

Figure 4.28 Sensitivity of CH100 longitudinal bar strain around bar debonding

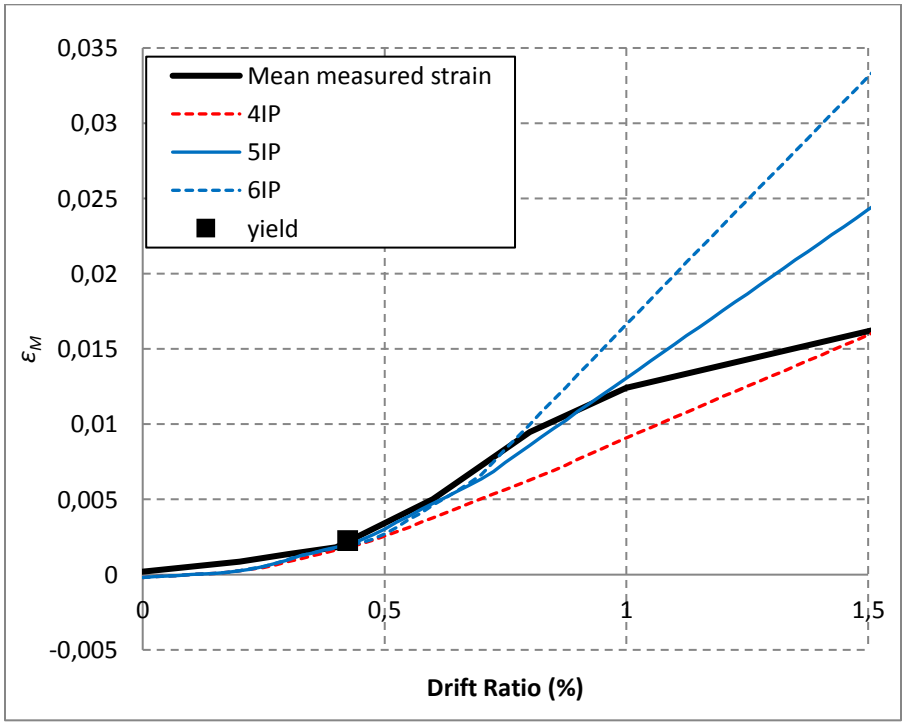

Figure 4.29 Sensitivity of CH60 longitudinal bar strain around bar debonding

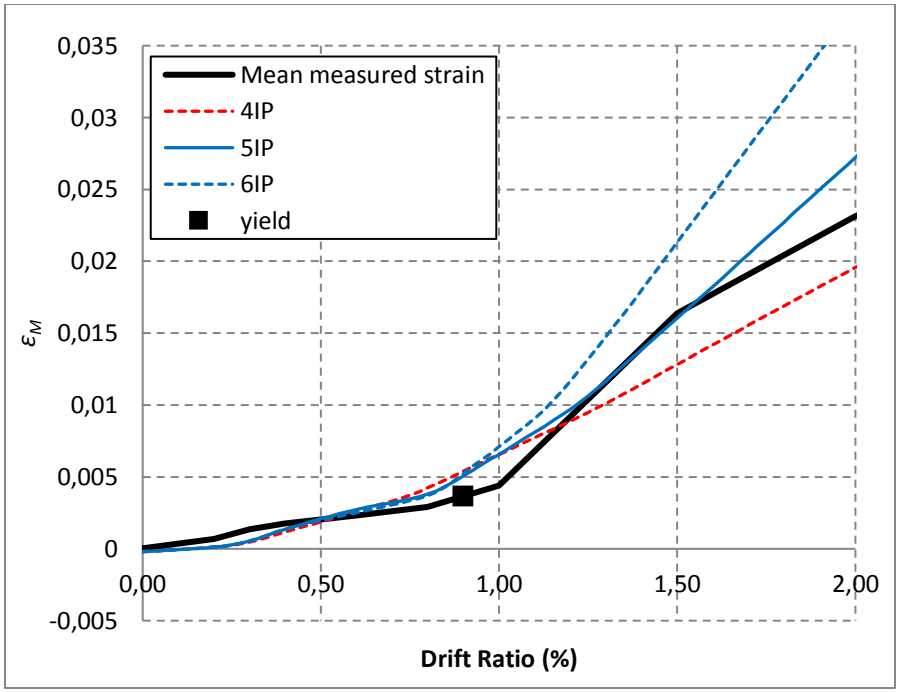

Figure 4.30 Sensitivity of CL100 longitudinal bar strain around bar debonding

4.7.2 Comparison Between Computational Model Strain Estimates and Measured Strains

Strain results for the outermost longitudinal bars produced by the computational model described in the previous section (with five integration points) are compared with experimental strains in Figure 4.31. In the figure, the drifts at which the computational and experimental strains diverge are highlighted.

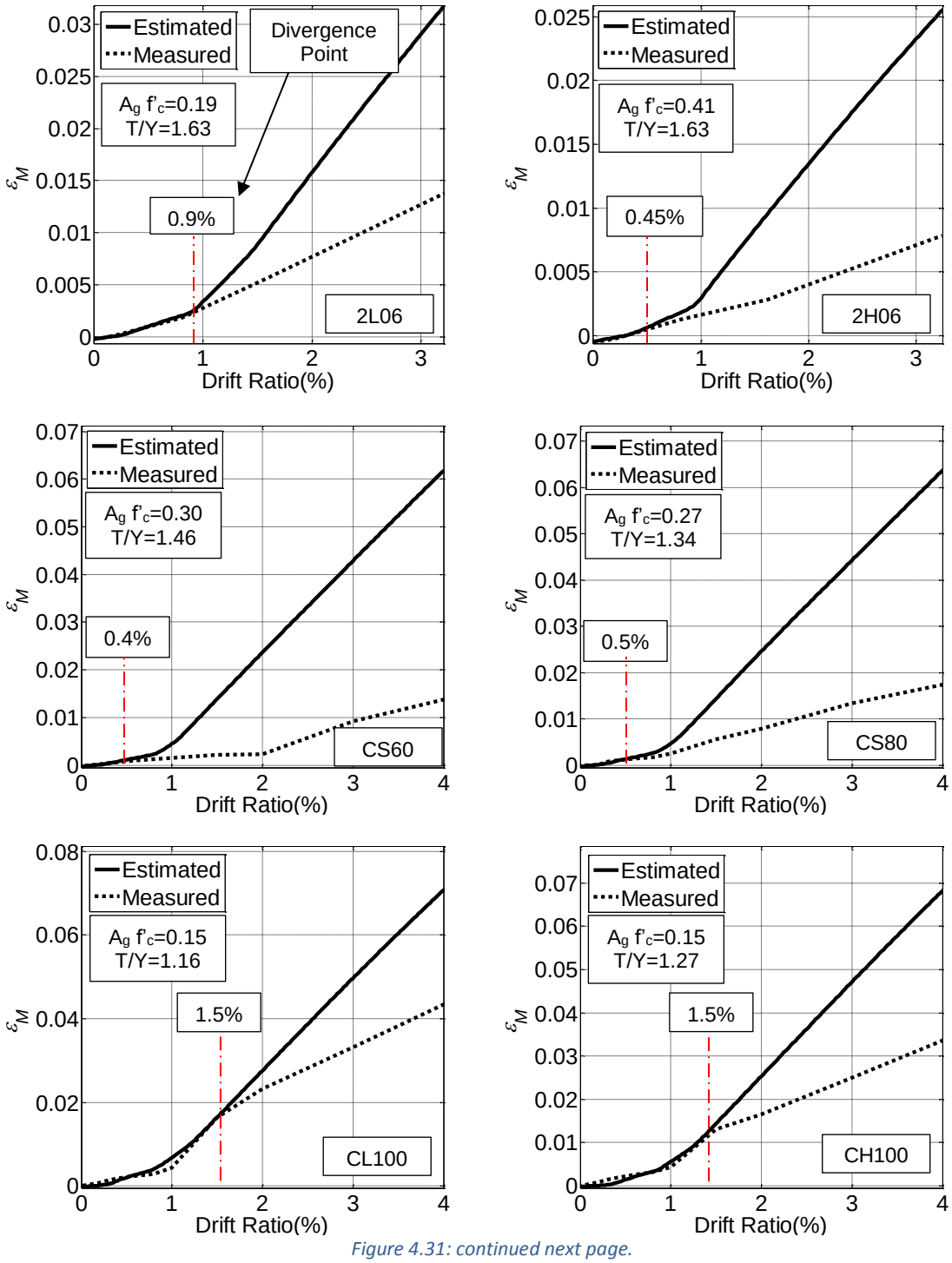

Figure 4.31: continued next page.

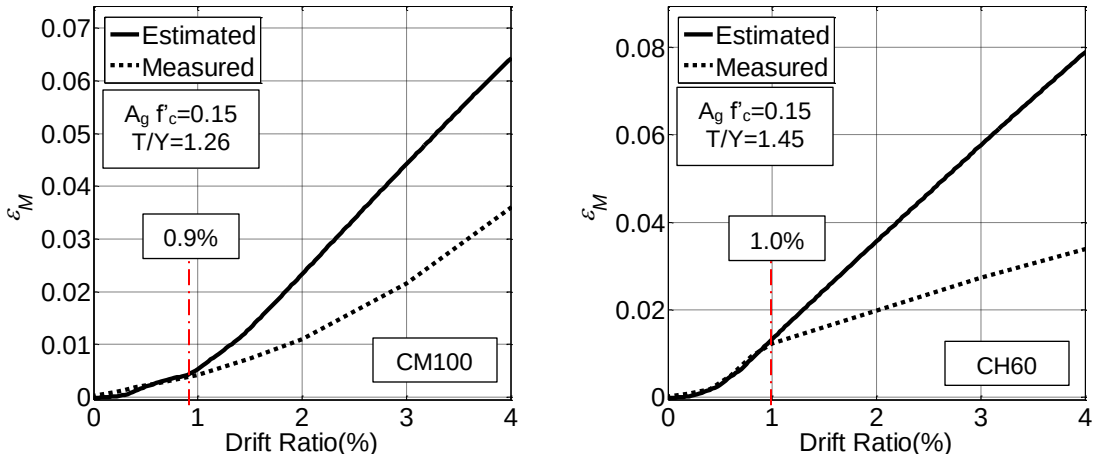

Figure 4.31 Comparison between estimated strain and measured strain with calibrated bond stress

As can be seen in Figure 4.31, the computational model seems to diverge from the experimental measurements at a different drift for each column. The "divergence points" coincide closely with the drift at initial hairline spalling cracking (SD1) determined using optical data (see section 3.4). A summarized comparison between the drift at the "divergence points" and SD1 is presented in Table 4-5.

Table 4-5 Comparison between SD1 and "Diverge Point"

Column	**SD1 Drift Ratio**	**Divergence Point Drift Ratio**	$\frac{P}{A_g f'c}$	$\frac{V_{max}}{b_w\, d\sqrt{f'c}}$ **(psi)**
2L06	N/A	0.90%	0.19	4.46
2H06	N/A	0.45%	0.41	4.74
CS60	0.80%	0.40%	0.30	10.55
CS80	1.00%	0.50%	0.27	9.86
CL100	1.50%	1.50%	0.15	3.93
CH100	1.50%	1.50%	0.15	4.00
CM100	N/A	0.90%	0.15	4.55
CH60	1.00%	1.00%	0.15	3.15

It is noteworthy that the computational strains are always larger than the measured strains after the divergence points. The computational model also miscalculated the drift ratio at first yield for

columns under high axial loads (2H06, CS60 and CS80) because spalling occurred before the longitudinal bars yielded in these columns. On the other hand, for columns under low axial load (2L06, CL100, CH100, and CH60), the computational model could estimate the strain with good accuracy until the concrete starts to spall. Column CM100 is an exception because of the absence of yield plateau in the longitudinal bar stress-strain relation.

4.7.3 Relation for Estimating the Drift at Bar Debonding

From the trends observed in Figure 4.31, it can be concluded that the estimated strains using the computational model and the measured strain start to diverge when debonding of the bars occur. For that reason, it is important to predict the drift ratio at which bars start losing bond with the concrete. The "divergence point" drift ratios were normalized by the effective section depth (*d*) because larger sectional depths produce larger compressive strains for a given drift level. The column CM100 divergence point was not included in this analysis because of the absence of a significant jump in the strain progression after reaching the defined yield point due to the steel stress-strain curve not having a yield plateau. The Pearson correlation method statistical analyses between the normalized divergence points and potentially influential parameters were conducted. The result of Pearson correlation is presented in Table 4-6. The influential parameters considered included: the axial load ratio, the normalized shear stress, the bar bond demand to capacity, represented by the yield strength divided by the square root of the concrete strength, and the amount of confinement, represented by the spacing of ties. The normalized shear stress (v_{max}) was calculated by dividing the maximum lateral force from the analysis by the column section width, effective depth (*d*) and $\sqrt{f'c}$:

$$\frac{V_{max}}{b_w\, d\sqrt{f'c}}(psi) \tag{4-7}$$

Table 4-6 Pearson correlation value for the "Divergence Point"/d

Pearson Correlation	$\frac{P}{A_g f'c}$	$\frac{V_{max}}{b_w\, d\sqrt{f'c}}$	$\frac{f_y}{\sqrt{f'c}}$	$\frac{s}{d_b}$
Divergence Point/d	-0.823	-0.733	-0.645	-0.135

The correlation analysis result showed that the "divergence point" had high correlation with the axial load ratio, shear stress, and normalized bar yield strength. Limited correlation was observed with the tie spacing normalized by the bar diameter. The axial load ratio and shear stress exhibit high correlation to respelling and bar debonding likely because high axial loads and shear stresses tend to generate large compressive strains in the concrete. Moreover, lower bar yield strengths and strain are reached at earlier drift ratios rather than column with higher bar yield strength. After the bars yield, the strain demand increases rapidly, which can cause larger concrete strains and localized debonding.

To predict the drift ratio at which longitudinal bars start to lose bond with the concrete (DR_{debond}), a linear regression analysis was performed with the influential parameters to obtain empirical equation. The details for the regression analysis result is presented in Appendix C. The empirical equation obtain is expressed as:

$$DR_{debond} = \frac{d}{1000}\left(0.065\left(\frac{f_y(psi)}{\sqrt{f'c(psi)}}\right) - 4\left(\frac{V_{max}(psi)}{b_w\, d\sqrt{f'c(psi)}}\right) - 140\left(\frac{P}{Agf'c}\right) + 36\right) \qquad (4\text{-}8)$$

4.7.4 SENSITIVITY OF THE CONSTANT BAR SLIP BOND STRESS

The calibrated constant bond stress (u) value presented in Table 4-4 varied between $9\sqrt{f'c}$ and $18.00\sqrt{f'c}$ in psi units. Due to this variability in constant bond stress value, a sensitivity study was conducted to observe any significance changes in strain behavior with changing bond stress parameter. Three values of constant bond stress coefficient were chosen to demonstrate its effect on strain behavior. Those value are $10\sqrt{f'c}$; $14\sqrt{f'c}$, and $18\sqrt{f'c}$.

The effects of increasing the constant bond stress value on strain behavior are demonstrated in Figure 4.32. As can be seen in the figure, the constant bond stress value influences the drift ratio at first yield obtained by the computational model. Moreover, longitudinal bar strains appear not to have a linear relation with respect to the bond stress, as it is varied from $10\sqrt{f'c}$ to $18\sqrt{f'c}$. On the other hand, the bond stress value does not affect the rate of increase in strain with increasing drift after yielding (Figure 4.32).

The strain differences with varying bond stress, or strain offsets, also appear to be different for every column as demonstrated in Figure 4.33. For example, the strain differences for column CL100 are higher than those for column CH60. The strain offsets from the lowest and highest bond stresses are summarized in Table 4-7. The strain offsets are also normalized by the effective depth (*d*) for each column in the table. The offsets are seen to vary as a function of the bar slip deformation at first yield. Bar slip deformation at first yield and strain offset are normalized relative to the values for column CS80 in Table 4-7. Those two values follow each other closely, which confirmed that the offsets varied with bar slip deformation at first yield.

Table 4-7 Strain offset analyses

Column	Strain Offset	Strain Offset/d	Relative Barslip Deformation at First Yield	Relative Strain Offset/d
2L06	0.0034	0.00025	1.05	0.93
2H06	0.0012	0.00009	0.45	0.32
CS60	0.0044	0.00029	1.16	1.07
CS80	0.0042	0.00027	1.00	1.00
CL100	0.0057	0.00035	1.27	1.31
CH100	0.0050	0.00031	1.12	1.14
CM100	0.0061	0.00038	1.33	1.39
CH60	0.0024	0.00015	0.56	0.54

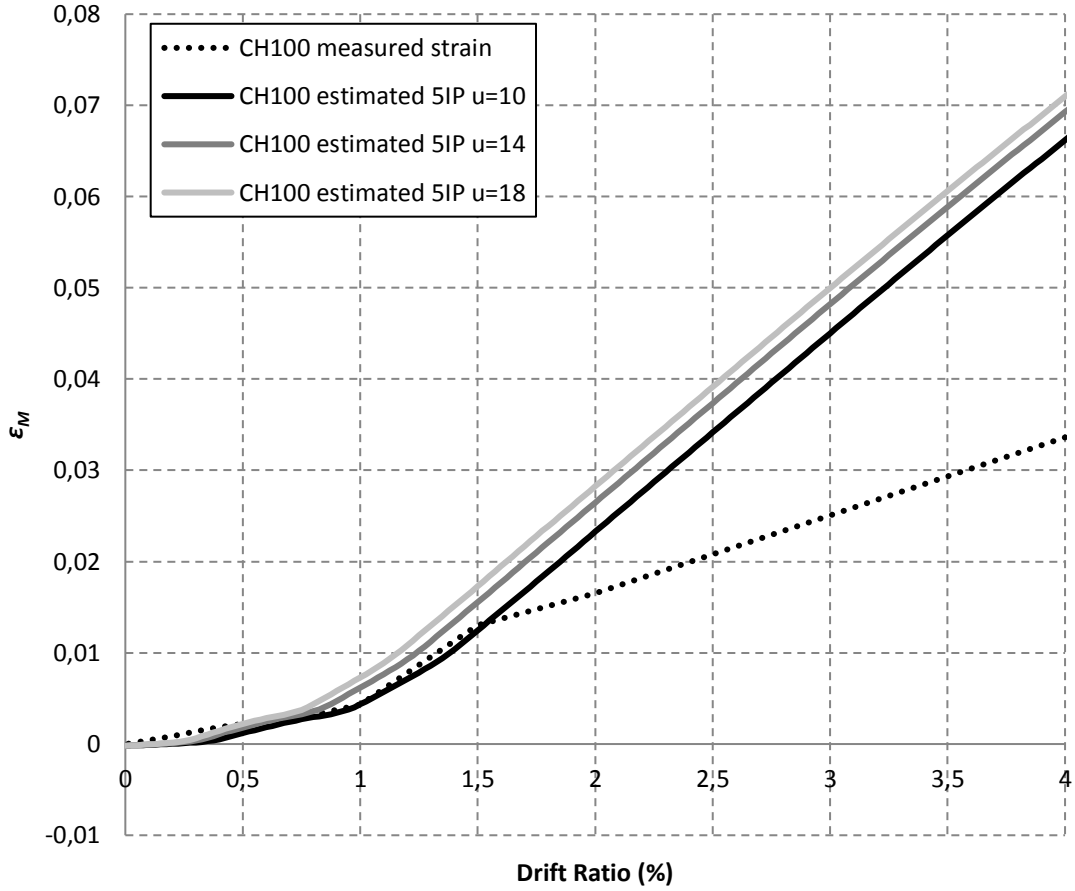

Figure 4.32 CH100 constant bond stress sensitivity

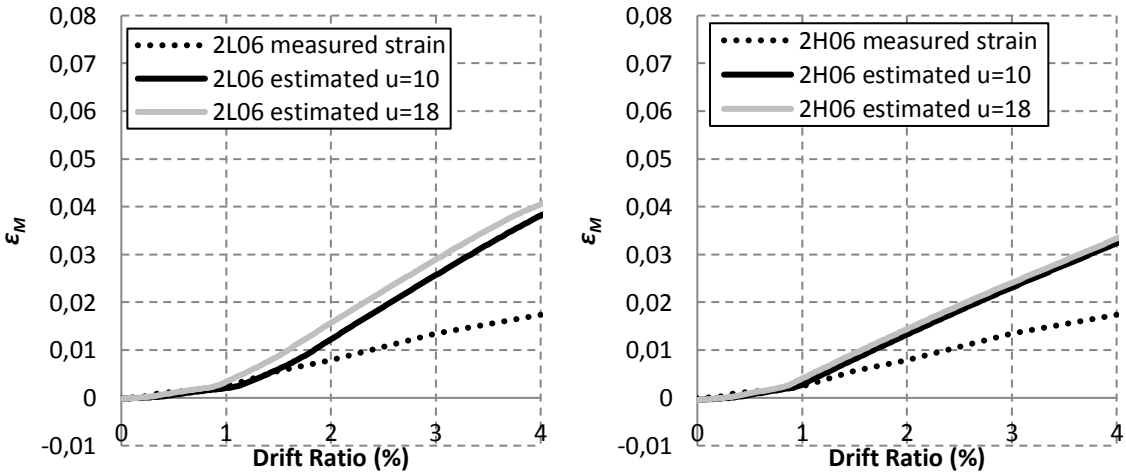

Figure 4.33: continued next page.

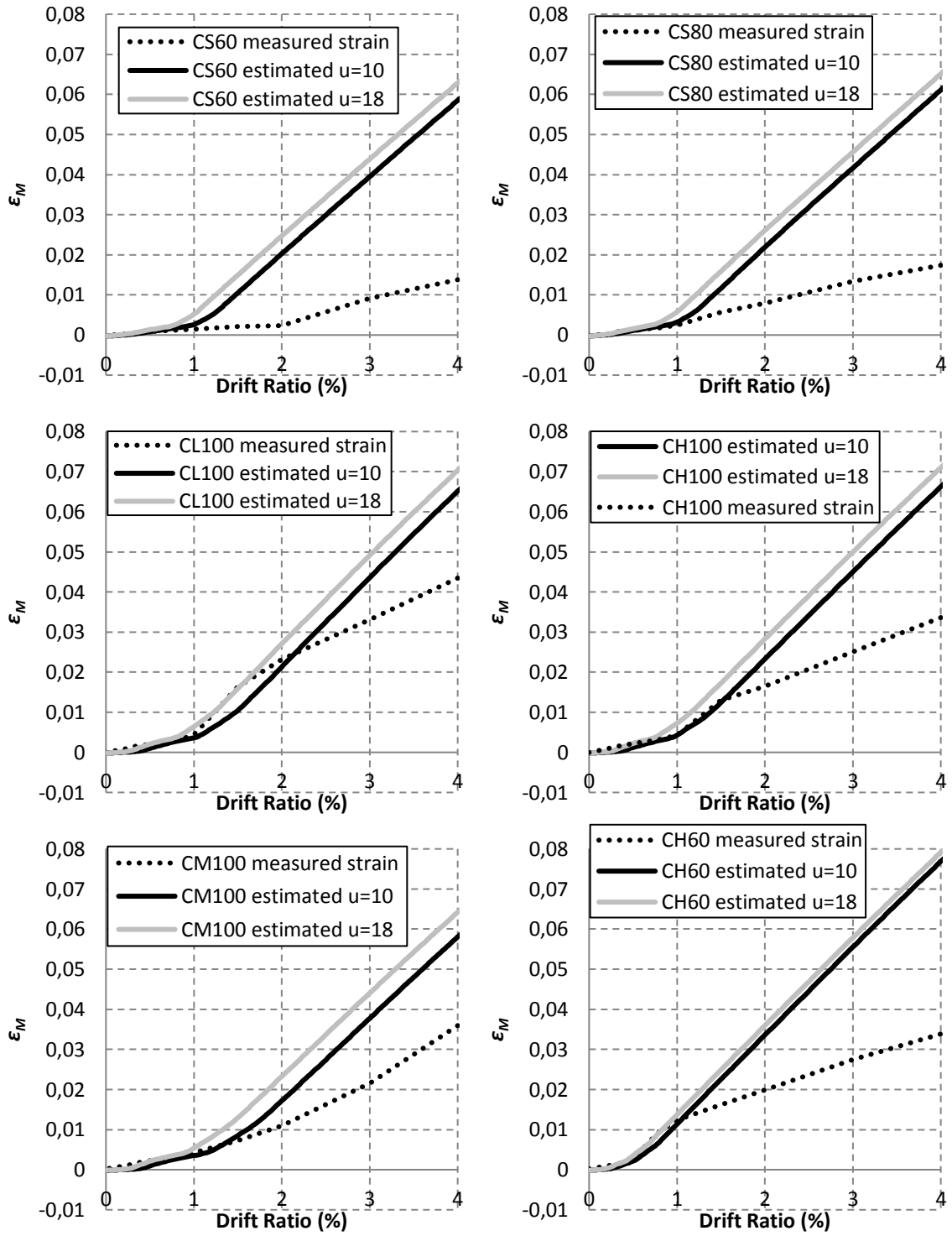

Figure 4.33 Sensitivity of constant bond stress on longitudinal bar strain

Currently, there is a wide range of recommendations for the constant bond stress value to use for columns. The average constant bond stress values recommended in the literature span the range of $0.5\sqrt{f'c}$ to $1.7\sqrt{f'c}$ in MPa units or $6\sqrt{f'c}$ to $20\sqrt{f'c}$ in psi units (Otani and Sozen, 1972; ACI Committee 408, 1979; Alsiwat and Saaticioglu, 1992; Sozen et al., 1992; Lehman and Moehle, 1998; Lowes et al. 2003; Ghannoum and Moehle, 2012b). A constant bond stress value was recommended for all columns as $0.8\sqrt{f'c}$ in MPa or $10\sqrt{f'c}$ in psi (Elwood and Eberhard, 2009) based on a large column test database. This value was also recommended to capture the lateral stiffness of a full size concrete building tested on a shaking table (Kwon, 2016).

While the value of constant bond stress of $10\sqrt{f'c}$ (psi) was found to produce reasonable column lateral stiffnesses, it did not appear to be suitable for predicting strains in the longitudinal bars. To identify the bond stress value that minimized strain errors at first yield across columns of this study, the following error function was evaluated:

$$error = \left|\frac{DRyield_{measured} - DRyield_{estimated}}{DRyield_{measured}}\right| \times 100\% \qquad (4\text{-}9)$$

The errors were only calculated for columns that sustained spalling and debonding after yielding and having steel with a yield plateau (2L06, CL100, CH100, and CH60). The errors are summarized in Table 4-8, from which a value of constant bond stress (u) of $14\sqrt{f'c}$ is seen to produce an acceptable error around 5% for every column. It is noteworthy that the test columns were connected to large footings that remained essentially undamaged during testing, which resulted in bond stresses on the higher end of the range provided in the literature.

No attempt is made in this study to provide a relation for estimating the bond stress parameter in this study as that parameter depends highly on the column boundary condition, which vary significantly from column to column and structure to structure. Most columns in buildings,

however, are connected to beam-column joints that have limited dimensions and sustain damage during the seismic event, which can result in higher bar slip deformations and lower bond stress values. Users of the proposed relations for bar strain demands should determine the bar slip bond parameters for their application.

Table 4-8 Bond stress errors (%) from Eq. 4-9

Column	$10\sqrt{f'c}$ (psi)	$12\sqrt{f'c}$ (psi)	$14\sqrt{f'c}$ (psi)	$16\sqrt{f'c}$ (psi)	$18\sqrt{f'c}$ (psi)
2L06	16.85	8.70	3.26	0.54	4.89
CL100	23.49	11.45	5.42	0.60	3.61
CH100	9.76	3.66	5.49	8.54	11.59
CH60	15.13	4.17	1.32	4.06	6.80

4.7.5 Effects of the Axial Load Ratio

The effects of the axial load ratio on the longitudinal reinforcement strains are discussed in this section. The experimental columns that isolate the effects of axial load ratio on the longitudinal reinforcement strain are column 2L06 and column 2H06. Both columns were nominally identical but were tested with different axial loads. Column 2L06 was tested with a 0.19 axial load ratio and column 2H06 with a 0.41 axial load ratio.

Estimated bar strains from the computational model illustrated in Figure 4.1 and with a constant bond stress parameter of $14\sqrt{f'c}$ (psi) are presented in Figure 4.34 along with experimental values. A constant bond stress value was used for all column in this section's analyses to remove the effect of bond stress.

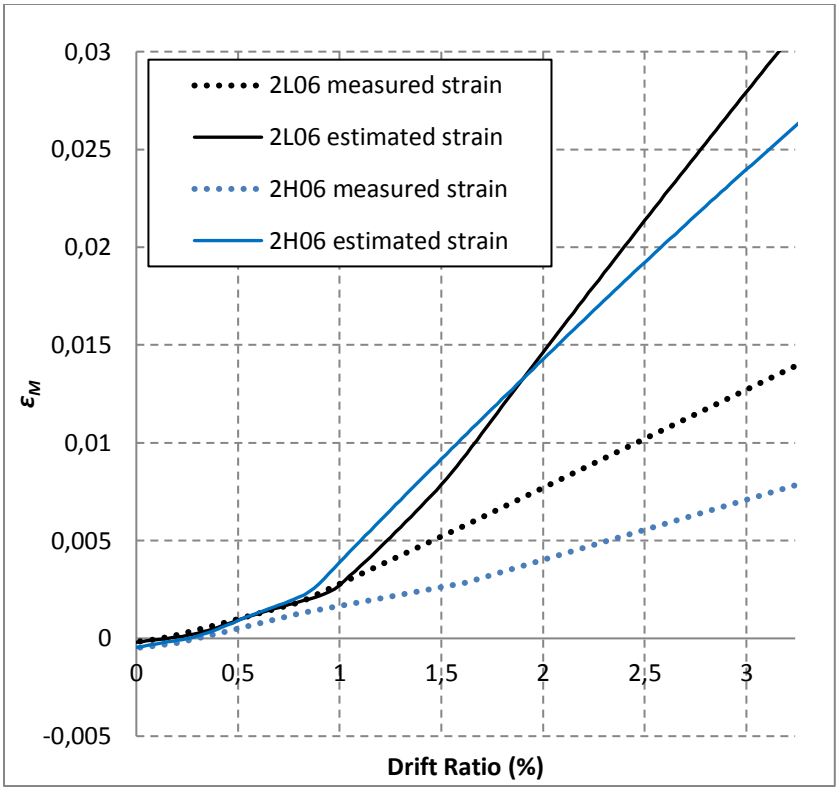

Figure 4.34 Effect of axial load ratio

As discussed in Section 3.6.3, the experimental measurements demonstrated that higher axial loads delayed the longitudinal bar yielding to larger drifts and produced lower strain increases with increasing drift after yielding. However, the computational showed the opposite trends, with the higher axial load generating yielding of the longitudinal bars at a lower drift. This occurred because the higher axial load resulted in the concrete model reaching its post-peak degrading branch at a lower drift, which re-distributed forces to the longitudinal reinforcement and yielded the steel. The column with higher axial load also suffered early spalling and bar debonding before the bar yielding, which the computational model is unable to capture.

4.7.6 EFFECTS OF THE STRAIN HARDENING RATIO AND YIELD STRENGTH

The effects of the strain hardening ratio (b) of the steel stress-strain model provided in Table 4-1 are discussed in this section. The experimental columns that isolate the effect of the strain hardening ratio on the longitudinal reinforcement strains are CL100, CH100, and CH60. CH100 and CL100 were nominally identical except for the reinforcing bar T/Y ratio and slightly different bar yield strengths. Column CH60 also had the same geometry and details as the other two but with a different T/Y ratio and a significantly different bar yield strength. Column CM100 was not included in this section because had the very different experimental strain behavior because had different steel stress strain curve (no yield plateau). The computational model described previously and illustrated in Figure 4.1 was used to generate the strain estimates. A constant bond stress of $14\sqrt{f'c}$ (psi) was used for all three columns to eliminate the effects of bond stress. The comparison between estimated strain and measured strain are plotted for all three columns in Figure 4.35.

As discussed in Section 3.4.1, the experimental strain measurements indicated that the longitudinal bar strain progression after bar debonding appeared to be related to the T/Y ratio of the bars. A higher T/Y ratio appeared to produce a lower strain progression with increasing drift. Even though the strain hardening had been adjusted for the steel material model, the computational results showed the same rate of strain progression with increasing drifts for all columns (Figure 4.35). On the other hand, the computational model appeared to capture the effects of the bar yield strength, with lower yield strengths yielding at earlier drift ratios.

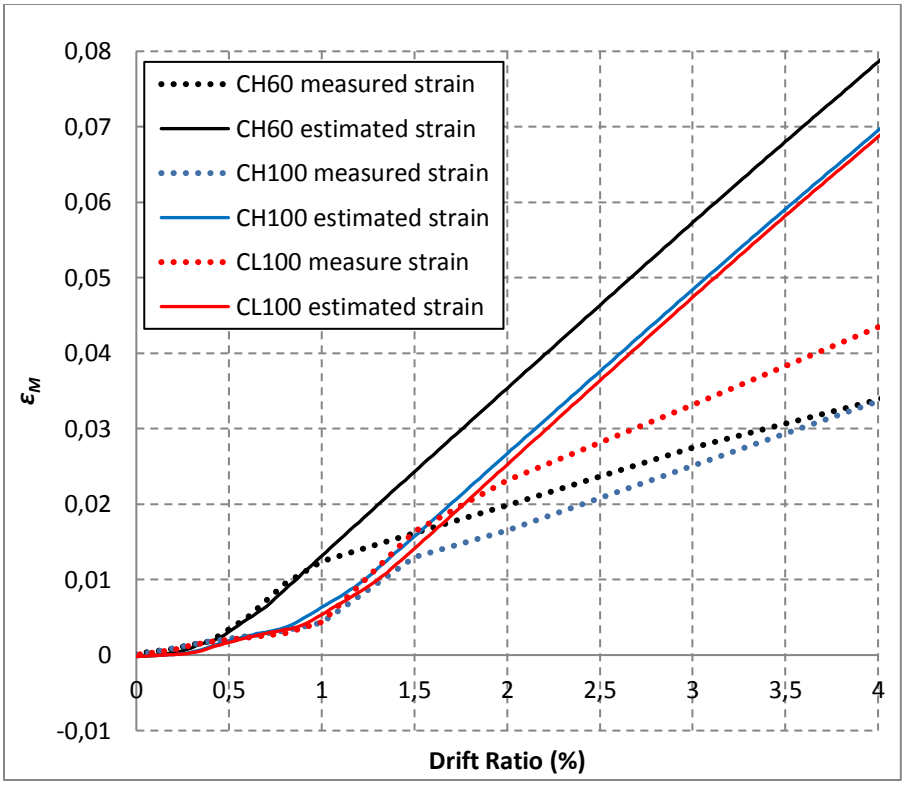

Figure 4.35 Effect of hardening ratio (b) and yield strength (f_y)

4.8 Scaling Factor for Longitudinal Bar Strains

4.8.1 Extracting Scaling Factors

A simple procedure is presented to obtain an objective prediction of the strain demand in longitudinal bars of concrete columns at the critical moment section. From the trends discussed in the previous sections and highlighted in Figure 4.31, strains obtained from the calibrated computational model are reasonably accurate prior to spalling damage and debonding, but are always larger than experimental strains after debonding occurred. These strains past debonding need to be scaled down.

The scaling form adopted in this study is given as:

$$\varepsilon_{i\,estimated} = \varepsilon_{i\,raw} \;\; for\; DR \leq DR_{debond}$$

$$\varepsilon_{i\,estimated} = \varepsilon_{debond} + (SF)\Delta\varepsilon_i \;\; for\; DR > DR_{debond} \qquad (4\text{-}10)$$

$$\Delta\varepsilon_i = \varepsilon_{i\,raw} - \varepsilon_{debond}$$

With,

$\varepsilon_{i\,raw}$ = raw computational strain output at the drift ratio corresponding to loading step i

ε_{debond} = raw computational strain at the drift ratio at which debonding occurs, DR_{debond}

from Eq. 4-8

SF = proposed scale factor

The scale factors calculated from Eq. 4-10 are plotted for each column in Figure 4-36 for drifts greater than DR_{debond}. The bar-slip rotational spring values used to obtain the computational strain used in Eq. 4-10 were based on the individual bond stress values for each column presented in Table 4-4. Column CM100 was excluded from this analysis because it was believed that the behavior is very different (Section 4.7.3).

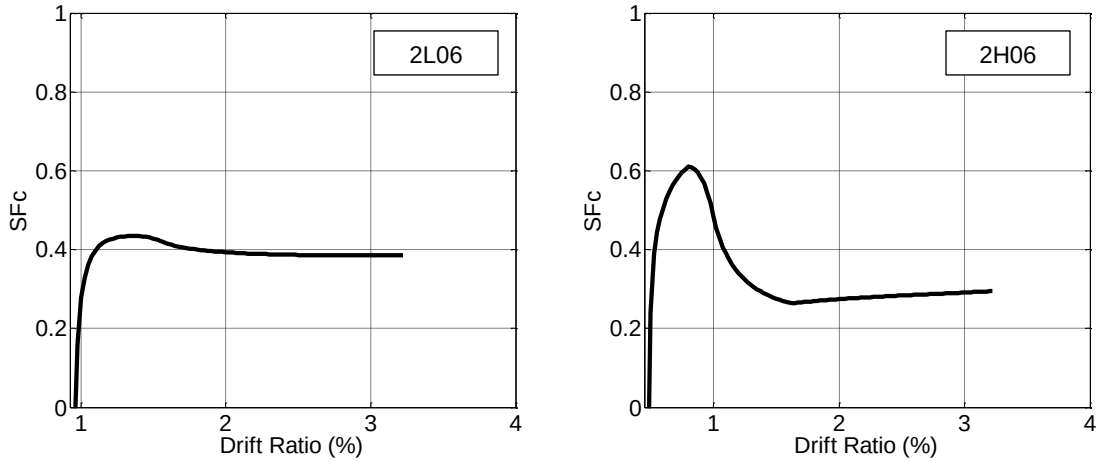

Figure 4.36: continued next page.

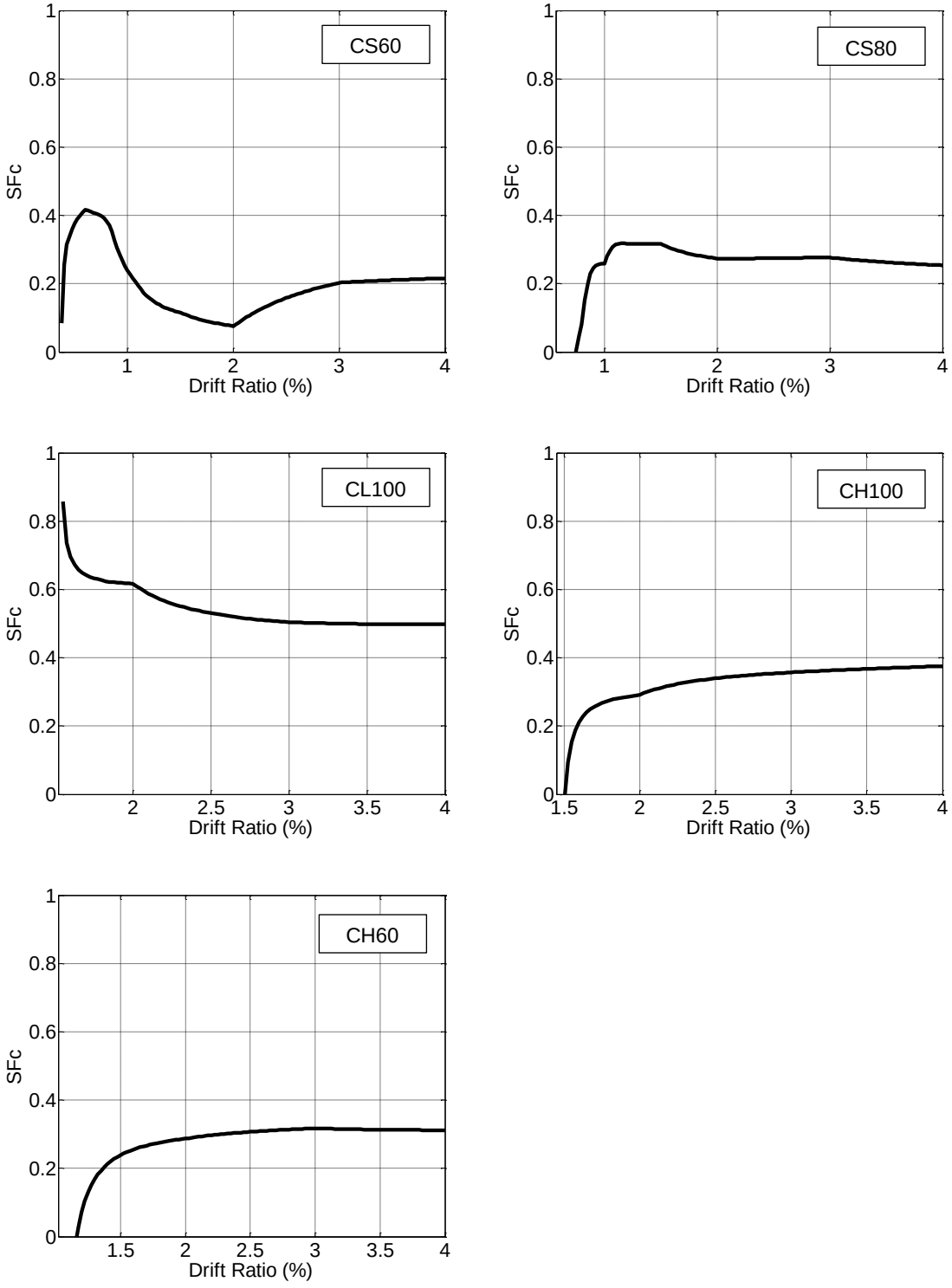

Figure 4.36 Scale factor versus drift Ratio after bar debonding drift ratio

The study objective is to predict the strain value in longitudinal bars accurately over the range of strains most critical for low-cycle fatigue failures of bars, but below the allowable design limits on member deformations. From the low cycle fatigue point of view, larger strain values are most critical to fatigue fractures, as the relation between strain amplitude and cycles to fracture is exponential (Brown and Kunnath, 2004 and Slavin and Ghannoum, 2015). Furthermore, ASCE 7-10 limits the story drifts to a maximum ranging from a drift ratio of 1.5% to 2.5% (2.25% to 3.75% for risk-targeted maximum considered earthquake) based on risk category of the structure for special moment frame concrete structure without shear wall. For these reasons, the scaling factor is selected to achieve the highest accuracy in strain estimates in the drift ratio range of 2.0% to 3.0%. To this end the scale factor values plotted in Figure 4.36 were averaged for each column over the drift ratio range of 2.0% to 3.0%. These average values (*SFc*) are presented in Table 4-10.

Table 4-9 Average scale factor in the drift ratio range of 2% to 3%

Column	$\boldsymbol{SF_c}$
2L06	0.39
2H06	0.28
CS60	0.15
CS80	0.27
CL100	0.54
CH100	0.33
CM100	N/A
CH60	0.31

4.8.2 TRENDS IN SCALING FACTORS

Trends between possible influential parameters and the derived strain scaling factors are illustrated in Figure 4.37. In figure 4.37, ρ_L is longitudinal bar ratio, l_d was obtained from Eq.

25.4.2.3a per ACI 318-14 without limiting the $\frac{c_b+K_{tr}}{d_b}$ term to 2.5, l_b is available development length, d_b is longitudinal bar diameter, a is shear span, s is hoops spacing.

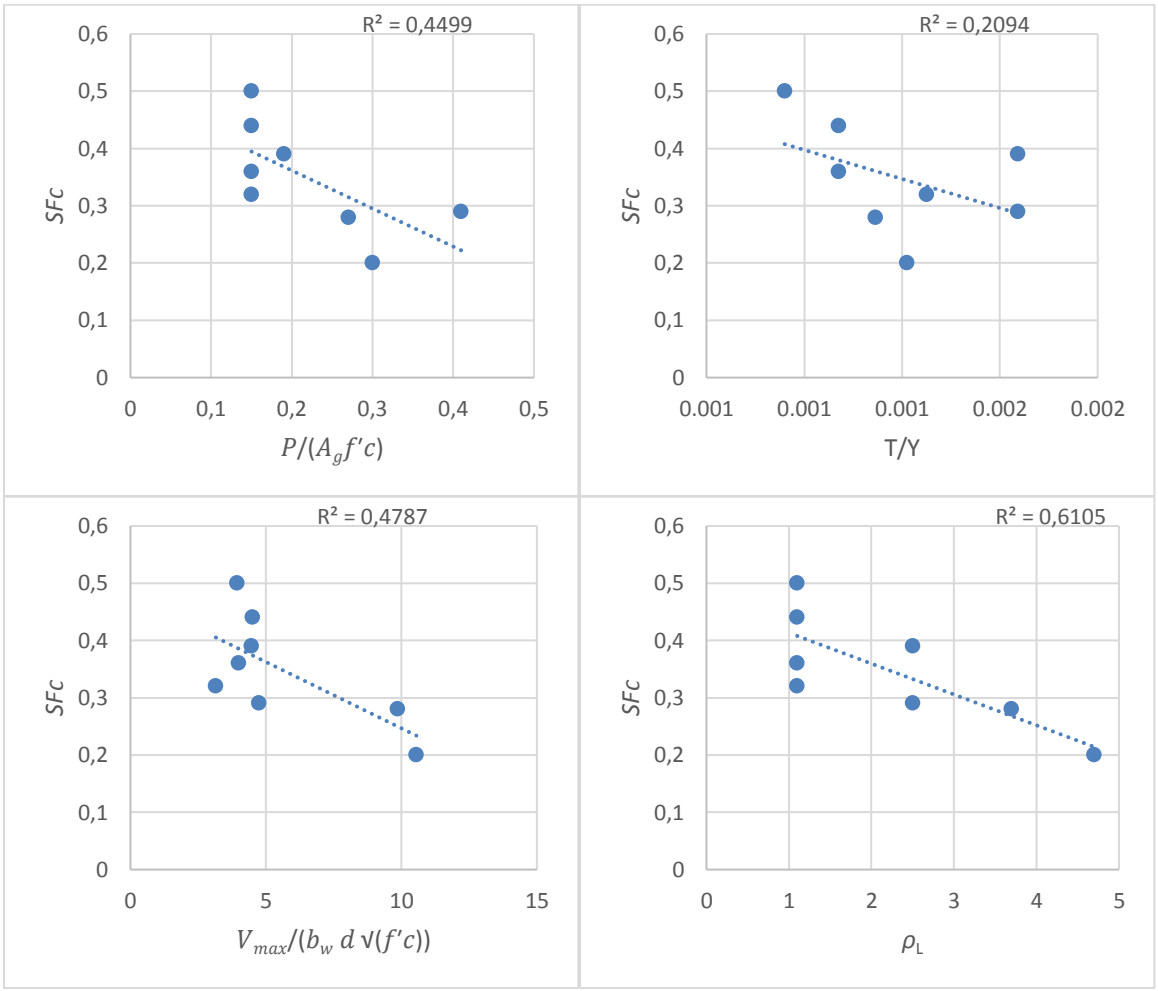

Figure 4.37: continued next page.

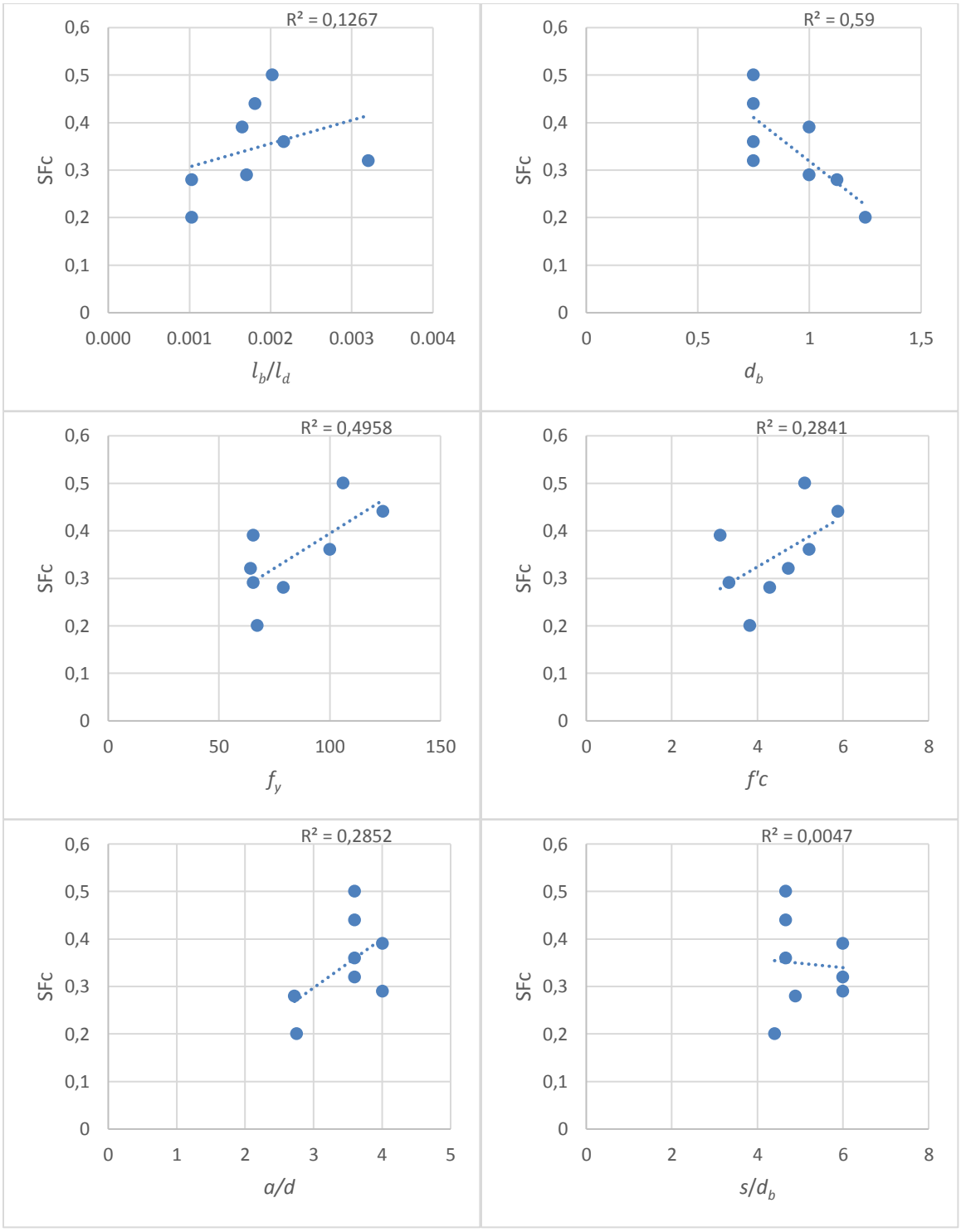

Figure 4.37 Scale Factor (SF_c) relationship with design parameters

From Figure 4.37, it can be seen that several terms appear to be correlated with the scaling factors (SF_c). The statistical analysis of best subset based on linear regression was performed to obtain the best subset of influential parameters. The details of the regression analyses are included in Appendix D. The derived empirical equation to predict the strain scaling factor is given as:

$$SF_E = 1.1 - 0.5\left(\frac{T}{Y} - 1\right) - 0.06\left(\frac{V_{max}}{b_w\, d\sqrt{f'c}}\right) - 0.08\left(\frac{l_b}{l_d}\right) \quad (4\text{-}11)$$

$\frac{T}{Y}$ = tensile to yield ratio

$\frac{V_{max}}{b_w\, d\sqrt{f'c}}$ = normalized maximum shear stress (psi units)

l_b = available development length = half the column clear span for the experimental columns

l_d = required development length per Eq. 25.4.2.3a in ACI 318-14 without limiting $\frac{c_b+K_{tr}}{d_b}$ term to 2.5

From Eq. 4-11, it can be concluded that lower values of tensile to yield (T/Y) ratio tend to reduce the scaling factor which increases the strains in the bars. This indicates that lower T/Y ratios concentrate strains in longitudinal bar at the critical flexural section. This behavior was also seen in the experimental observations presented in Chapter 3. Higher shear stresses are seen to increase the scaling factor, or decrease the bar strains, which can be attributed to the increased damage caused by the shear and the associated increase in bar debonding, as well as the effects of tension shift (illustrated in Figure 4.38). The ratio of available to required development length represents the bond demand to capacity of the longitudinal bars. The lower of the ratio $\left(\frac{l_b}{l_d}\right)$ is, the lower the bond demand which could translate into increased strain concentrations at the critical flexural crack.

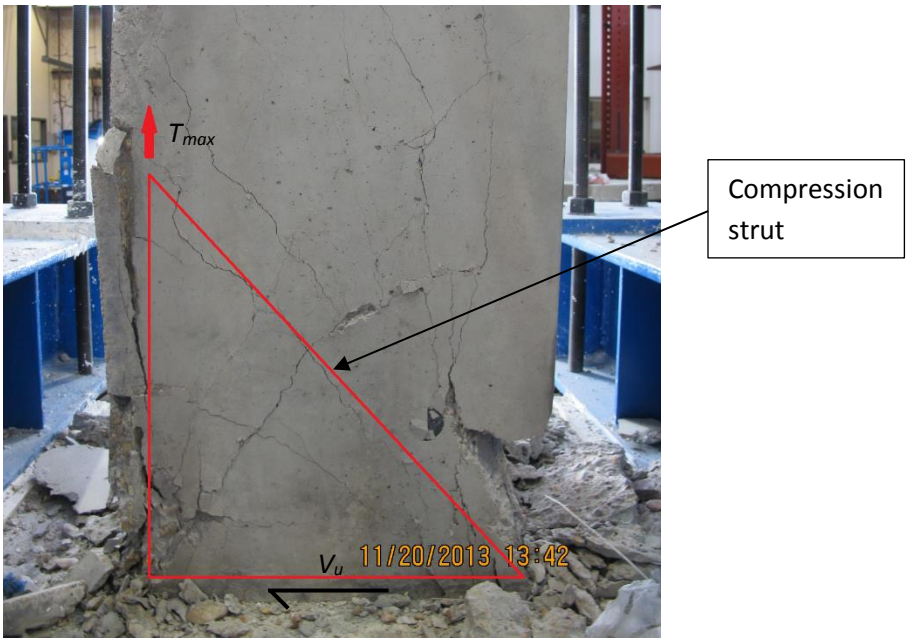

Figure 4.38 Illustration of tension shift phenomena on high shear stresses column (CS60)

4.8.3 ERRORS IN STRAIN ESTIMATES

The errors in strain estimates derived using the proposed computational model with the experimentally derived bond stress parameters (Table 4-11), coupled with strain scaling factor relation (Eq. 4-11) are presented in this section. The estimated scaling factors (SF_e) using Eq. 4-11 are summarized along with the experimentally derived scaling factors (SF_c) in Table 4-10 for each column.

Table 4-10 Scale factor estimation

Column	SF_c	SF_e
2L06	0.39	0.33
2H06	0.28	0.31
CS60	0.15	0.15
CS80	0.27	0.24
CL100	0.54	0.47
CH100	0.33	0.39

CM100	N/A	0.42
CH60	0.31	0.26

The longitudinal bar strain estimates versus column lateral drifts are plotted in Figure 4.39. These strain-drift relations were calculated using Eq. 4-10. Details for this process are presented in Appendix E.

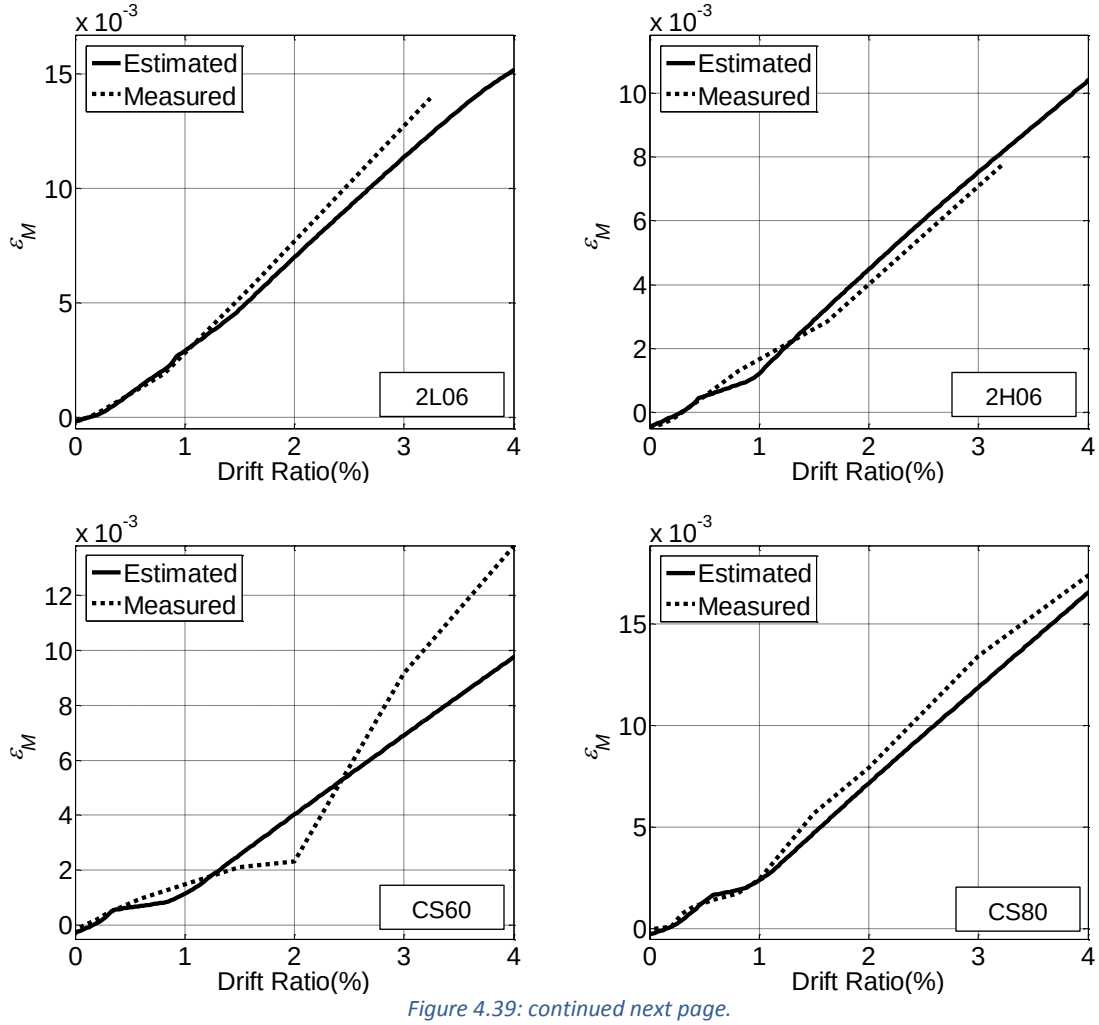

Figure 4.39: continued next page.

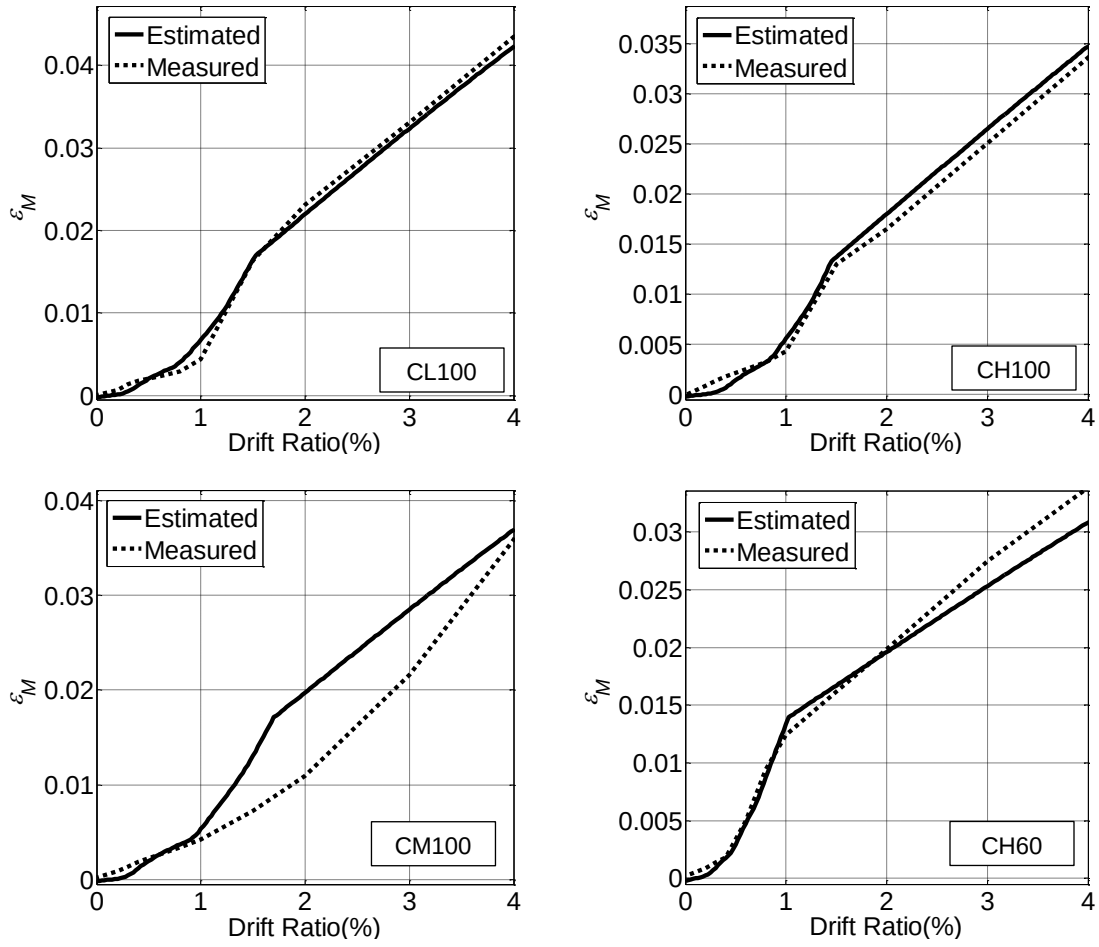

Figure 4.39 Measured versus estimated longitudinal bar strains obtained by scaling the computational model strains

The error ratio calculated as the measured strains divided by the estimated strains are presented in Table 4-11 for the drift ratios of 1.5%, 2.0%, 3.0%. The mean and lognormal standard deviations of the error ratio are also presented in the table. As can be seen in Table 4-11, the proposed procedure for estimating longitudinal bar strains in columns achieves close to mean estimate of the experimental strains with relatively low errors. The procedure does result is higher errors for column CM100, reinforced with A1035 steel. This column was not used in the calibration of the procedure as its behavior differed significantly from other column that contain steel with a well-defined yield plateau.

Table 4-11 Evaluation of strain estimation

Measured Strain/Estimated Strain			
Column	Drift Ratio		
	1.50%	2.00%	3.00%
2L06	1.11	1.10	1.12
2H06	0.90	0.89	0.94
CS60	0.82	0.58	1.33
CS80	1.20	1.11	1.13
CL100	1.00	1.05	1.02
CH100	0.95	0.92	0.95
CM100*	0.56	0.56	0.76
CH60	0.97	1.01	1.09
Mean**	**0.99**	**0.96**	**1.08**
Std Dev**	**0.13**	**0.22**	**0.13**

*Excluded from Mean and Std Dev calculation

**Based on 7 columns (without CM100)

4.9 Limits

The proposed model results were post-processed (Section 4.8.1) and adjusted using by the correction formulae (Eq. 4-8 and Eq. 4-11) based on the database of 7 columns shown in Table 4-12. No result verification with the data outside of the data used in calibrating the correction formulae were considered. Users of the proposed model for bar strain demands should be cautious when using the model out of the range of parameters in the database (Table 4-12). The proposed model may also not be appropriate for modeling longitudinal bar without yield plateau (such as A1035 bars) which has different strain progression behavior (Section 4.7.3).

Table 4-12 Column database for calibrating Eq. 4-8 and 4-11

Column	$\frac{P}{A_g f'c}$	T/Y	d_b (in.)	f_y (ksi)	ρ_L (%)	$f'c$ (ksi)	$\frac{V_{max}}{b_w\, d\sqrt{f'c}}$ (psi)	a/d	s/d_b
2L06	0.19	1.64	1.000	65.5	2.50	3.13	4.46	4.00	6.00
2H06	0.41	1.64	1.000	65.5	2.50	3.34	4.74	4.00	6.00
CS60	0.30	1.41	1.250	67.3	4.70	3.83	10.55	2.75	4.40
CS80	0.27	1.35	1.125	79.1	3.70	4.29	9.86	2.72	4.90
CL100	0.15	1.16	0.750	106	1.10	5.11	3.93	3.60	4.70
CH100	0.15	1.27	0.750	100	1.10	5.21	4.00	3.60	4.70
CH60	0.15	1.45	0.750	64.4	1.10	4.57	3.15	3.60	6.00

5 SUMMARY AND CONCLUSIONS

5.1 Objective

The primary objective of this work was to develop an analytical model capable of estimating the global deformation behavior of reinforced concrete columns, while delivering reliable strain demands on longitudinal bars through the full range of expected inelastic deformations during seismic demands. The model was calibrated based on seven cyclic experimental tests conducted on columns pushed to large damage states and monitored using a high-resolution optical strain measurement system (Sokoli et al., 2014). Parameters extracted from those tests were scrutinized for trends between strain demands on reinforcing bars and influential parameters. The proposed model utilizes a force-formulation fiber-section element to which a scaling relation is applied to correct steel fiber strains to match experimental results.

5.2 Summary of Work

The proposed model for column members is a force-formulation distributed plasticity, line-element with a Gauss-Lobatto integration scheme. This type of element was selected because it provides an estimate of longitudinal bar strains that intrinsically captures much of the effects of member geometry, reinforcing details, material properties, and the interactions between flexure and axial load. The element was calibrated to cyclic experimental tests to determine the optimal number of fibers and integration points for simulating the flexural deformations. As a result, five integration points are recommended to be used in force-based line element for double curvature rectangular columns.

To capture the column deformation due to shear which was relatively small for most columns, the shear deformation was modeled through shear springs at the ends of the columns with elastic

stiffness. The shear deformation is modeled according to elastic theory and idealized as homogenous, isotropic material with a constant, reduced shear modulus. Furthermore, column deformations due to bar slip were modeled through elastic rotational bar slip springs at the ends of the columns. Assuming a uniform bond stress between bars and adjacent concrete, and that bar slip rotation occur around the flexural neutral axis of the section, the rotational bar slip stiffness was calibrated by modifying the constant bond stress value for each column to match the experimental bar slip deformations at first yield.

After satisfying column global deformations, satisfying the longitudinal bar strain demand was the next step. The proposed model with five integration points estimated reliable strains in longitudinal bars prior to the initiation of spalling cracks and associated bar debonding. A scaling factor is proposed to modify the strains obtained from five integration point computational model after bar debonding occurs. The bar debonding drift ratio was estimated by a proposed relation. The bar debonding drift ratio as found to vary as a function of the axial load ratio, shear stresses, and the yield strength of longitudinal bars. The longitudinal strain scaling factor for each column was found to be governed by the tensile to yield strength ratio of the longitudinal bars, shear stresses, and the bond demand to capacity of the longitudinal bars.

5.3 Summary of the Proposed Model

The proposed analytical model includes a computational distributed plasticity model coupled with a strain scaling relation that can be used post analyses to adjust the strains obtained from the computational model. Details of each of the model elements and material models are summarized next:

1. *Flexural element. The* flexural element uses a force-based fiber-section beam column element with 5 Gauss-Lobatto integration points. The element fibersection are recommended to be subdivided into a minimum of 10 core concrete fiber, 10 side cover concrete fiber, and 2 extreme cover concrete fibers. A Gauss-Lobatto integration scheme with 5 integration points must be used in the force-based beam column element as it produces strains values that are compatible with the proposed strain scaling relation.

2. *Cover concrete material model.* The recommended concrete cover material model is Kent-Park (1971) concrete stress-strain model with regularized softening response (Coleman and Spacone, 2001). The regularization of the cover concrete stress-strain model is mandatory. Recommended value of fracture energy used in regularization method is 0.342 k/in. The tension stiffening model is also recommended to be included with peak tension stress selected as the modulus of rupture per ACI 318-14. The Kent-Park stress-strain model with tension stiffening is available through the concrete02 material in the OpenSees material library.

3. *Core concrete material model.* The recommended core concrete material model is based on the Mander confined concrete model (Mander et al., 1988) with maximum strain as proposed by Qi and Moehle (Qi and Moehle, 1991). The tension stiffening model is also recommended to be included with peak tension stress as modulus of rupture per ACI 318-14. The Mander confined concrete model with tension stiffening is available through the concrete04 material in the OpenSees material library.

4. *Steel reinforcement material model.* The recommended steel reinforcement material model is the Giuffre-Menegotto-Pinto (1972) model with isotropic strain hardening. The strain hardening ratio is recommended to be calculated with Eq. 4-2 described in Section 4.1.2 based on actual bar hardening properties.

5. *Shear spring elements.* Shear springs elements use a reduced elastic shear spring with stiffness as expressed in Eq. 4-6.

6. *Bar slip rotational spring elements.* Bar slip rotational spring elements use elastic rotational spring with stiffness as expressed in Eq. 4-6. No attempts were made to provide a relation for bar slip rotations as any relation would be highly dependent on the boundary conditions of the column being considered (e.g., framing into a joint or a footing). The constant bond stress value between reinforcement and concrete that is associated with the rotational spring stiffness should be determined by the user based on column end connections. The consequences and sensitivity of various constant bond stress value are described in Section 4.7.4.

7. *Strain calibration.* Longitudinal bar strains output from the analysis software are required to be processed according to post-processing procedure in Chapter 4.8.1 with bar debonding drift ratio and scale factor as expressed in Eq. 4-8 and 4-11 respectively.

5.4 Conclusions

5.4.1 Influential Parameters for Damage Spread

- From the horizontal surface strain measurement in Section 3.4, it was concluded that columns with longitudinal bars having a lower T/Y ratio experienced more concentrated spalling damage at their ends than those with bars having higher T/Y ratios.

- The spalling damage of columns under high axial loads and high shear stresses also appeared to be more spread away from column ends. These trends were demonstrated using horizontal surface strain measurements presented in Chapter 3.4.

5.4.2 INFLUENTIAL PARAMETERS ON STRAIN DEMANDS IN LONGITUDINAL BARS

- Bar debonding has a big influence on strain demands in reinforced concrete columns. The strain increase with increasing lateral drift decreases when the longitudinal bars loose bond with the concrete after spalling cracks occur.

- High shear stresses, high axial load ratios, and low longitudinal bar yield strengths resulted in bar debonding at lower drift ratios which decreases the strain demand significantly at the same drift level compared to columns with low shear stresses, low axial load and high longitudinal bar yield strength (Figure 3.34).

- Longitudinal bar strains increase more rapidly with increasing drifts when the damage is concentrated near the end of the column. A lower longitudinal bar T/Y ratio was found to increase strain concentrations due to the concentration of spalling damage at column ends. Higher shear stresses increased damage at the compression toe and generated increased bar debonding, while high shear stresses also increased the bar train spreading effects of the tension shift phenomenon. A lower bond demand to capacity ratio on longitudinal bars translated into higher strain concentrations.

- The existence of a distinct yield plateau in the longitudinal bars resulted in a sudden and significant jump in bar strains right after yielding. By contrast, the absence of a yield plateau in the longitudinal reinforcement resulted in a much more gradual increase in bar strains with increasing column lateral drift.

- The strength of the longitudinal reinforcement defines when the significant increase in strain progression with column drift occurs. Columns with lower strength of steel and associated lower yield strain, experience bar yielding at lower drifts compared with columns having simialr details but bars with a higher yield strength.

5.4.3 PROPOSED MODEL

- A five integration point Gauss-Lobatto distributed plasticity force-based beam column element could accurately estimates global deformation and strain demands prior to bar debonding.

5.5 Recommendation for Future Work

The proposed model was calibrated based on a limited subset of tests and should be verified using a larger data set and extended to wider range of column parameters. Alternative modeling parameters or procedures that do not require post-processing procedure to capture bar strains need to be developed. Developing additional element that can model the degrading bond of concrete and steel reinforcement may help the model to capture bar strains. Further investigation about compression strains of longitudinal bar and the modeling strategy to estimate the compression strains still need to be developed. Additional tests need to be conducted to fully understand the effects of bar strength and T/Y ratio, shear stresses, and bond demand or capacity on the strain demands on other reinforced concrete members such as beams and walls. Additional tests of column reinforced with A1035 longitudinal bars are needed to fully understand their strain progression behavior. Since bar slip deformation influence stain estimates in bars significantly, relations are needed to best estimate such deformations with various connecting elements, such a beam-column joints.

APPENDIX A: MEAN STRAIN MEASUREMENTS

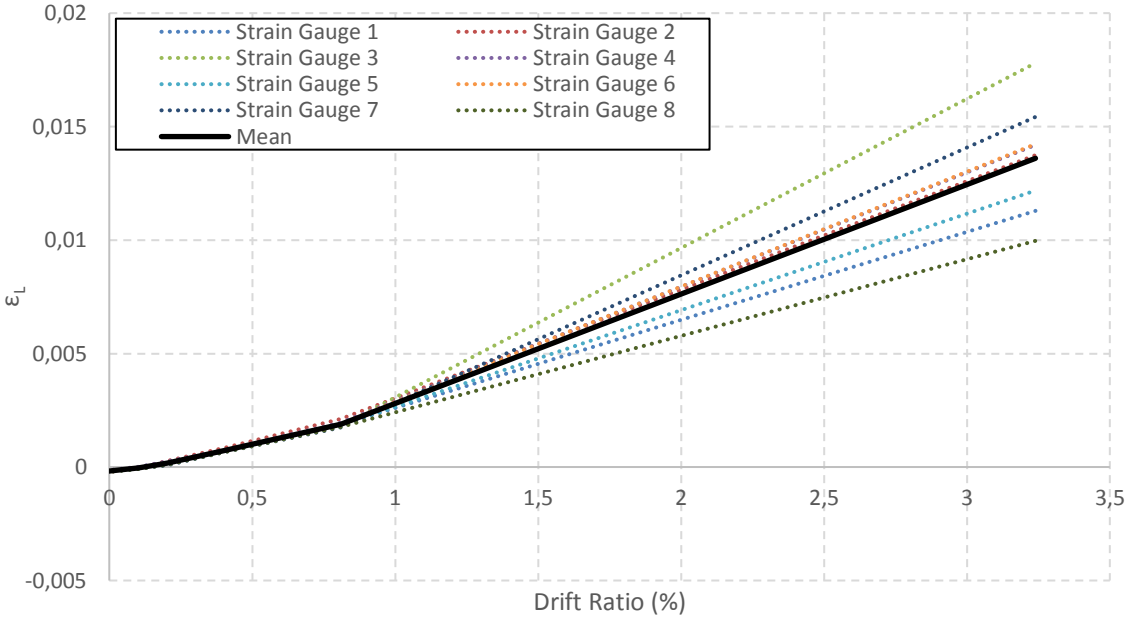

Figure A.1 Measured strain of column 2L06

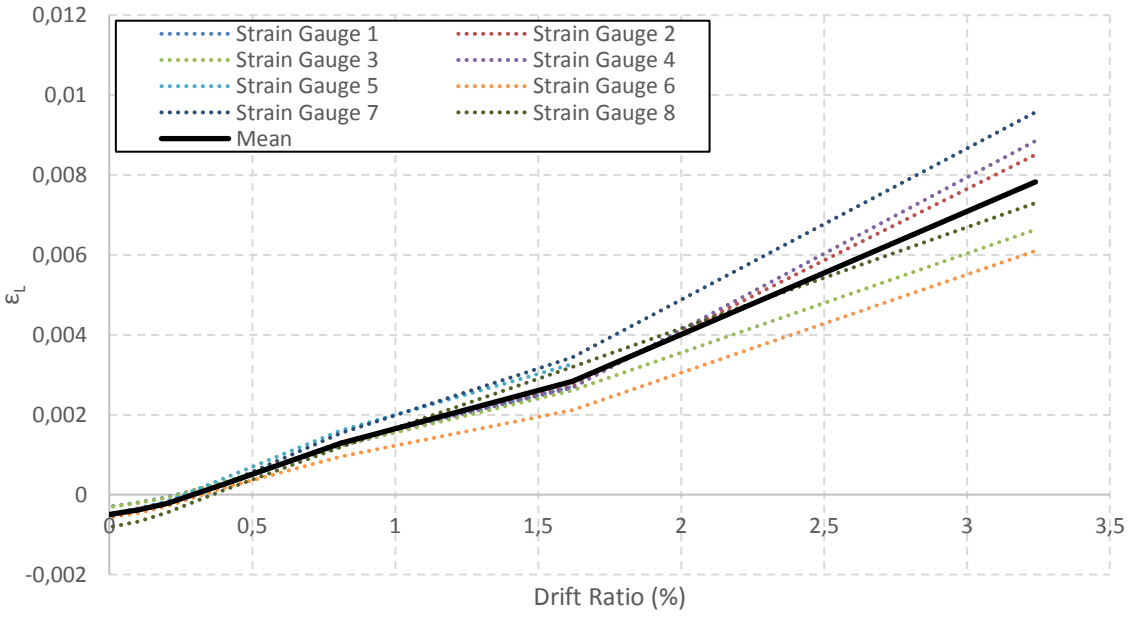

Figure A.2 Measured strain of column 2H06

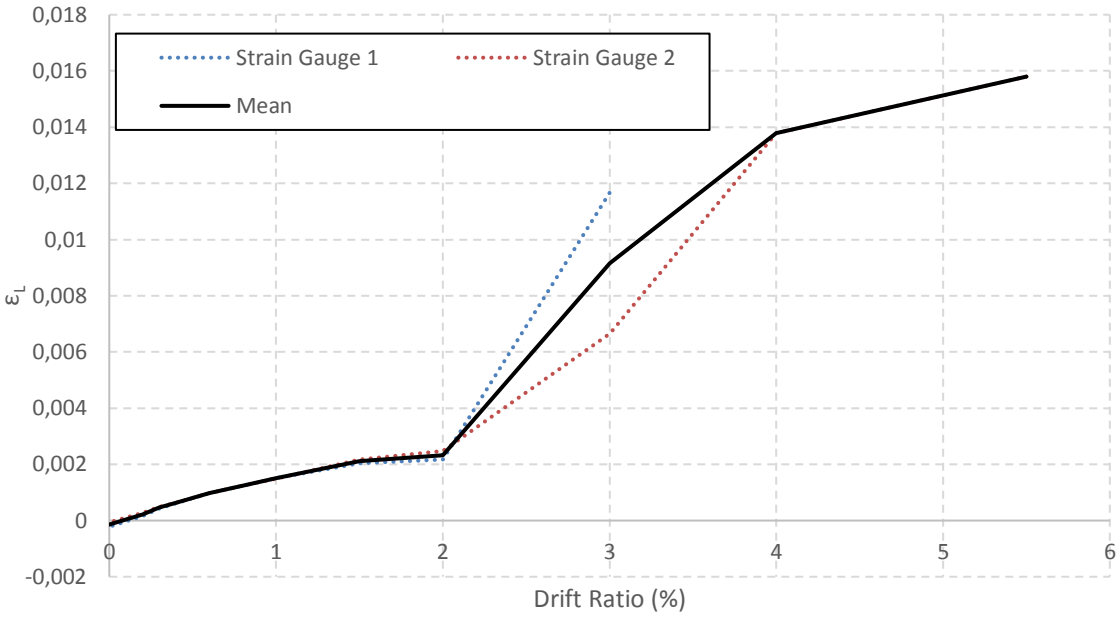

Figure A.3 Measured strain of column CS60

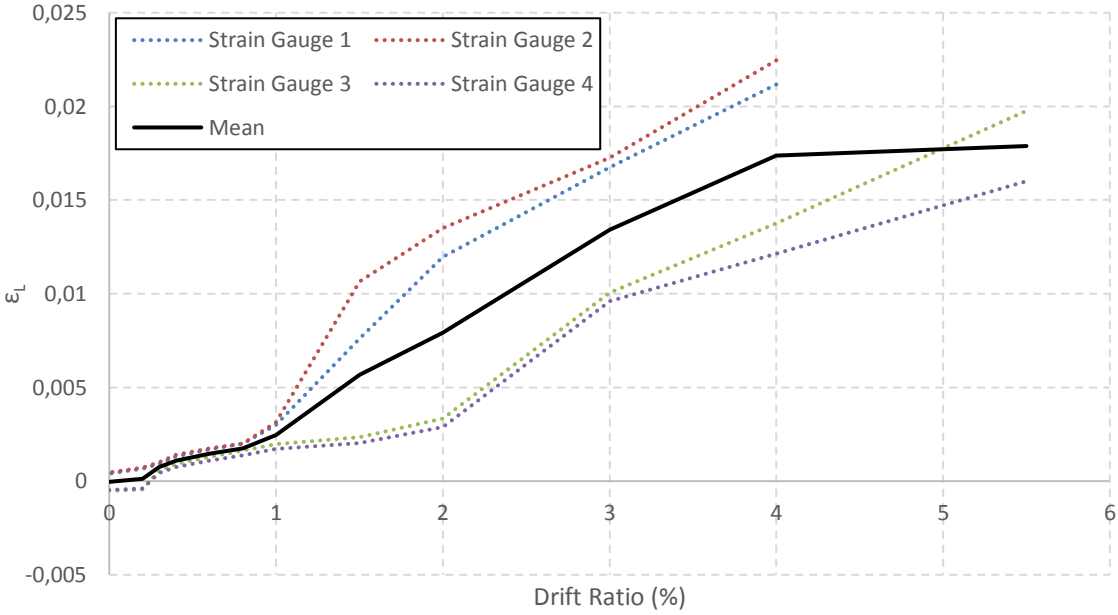

Figure A.4 Measured strain of column CS80

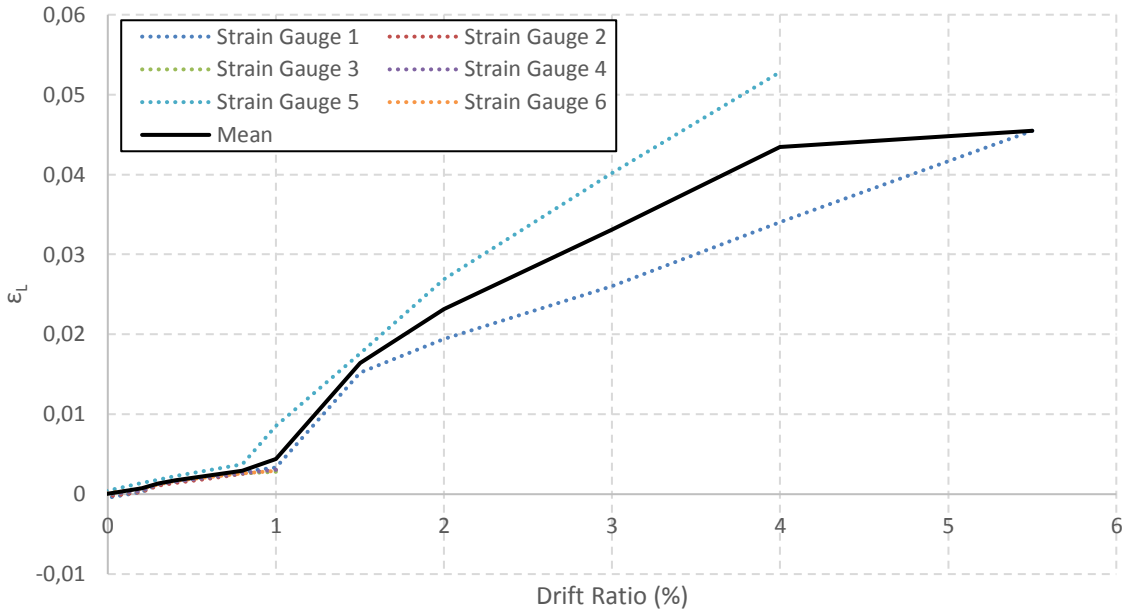

Figure A.5 Measured strain of column CL100

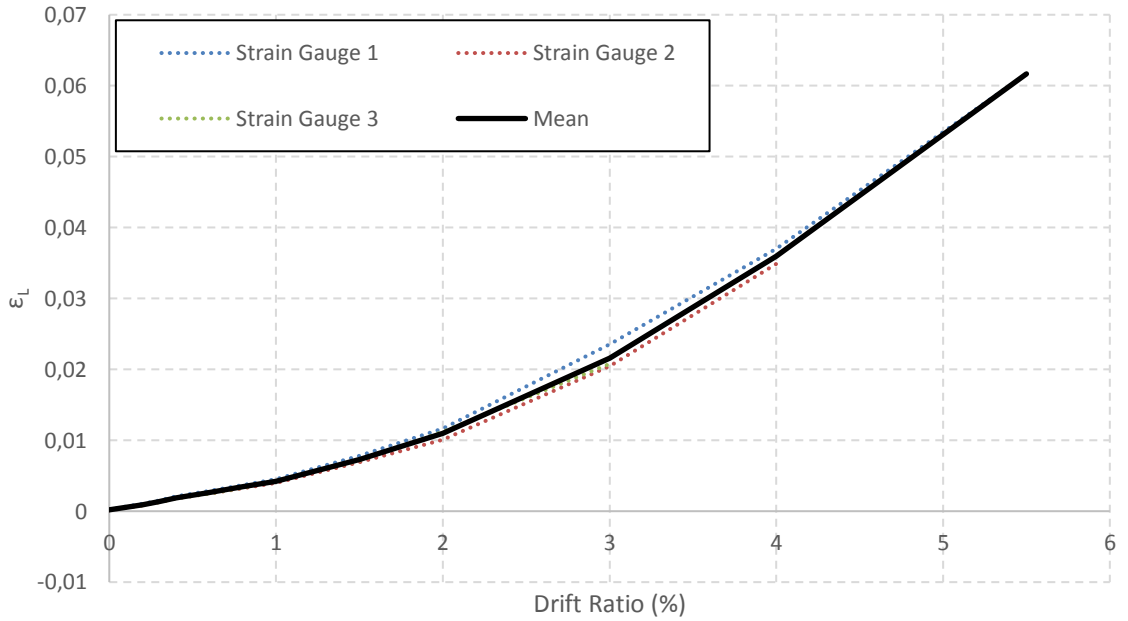

Figure A.6 Measured strain of column CM100

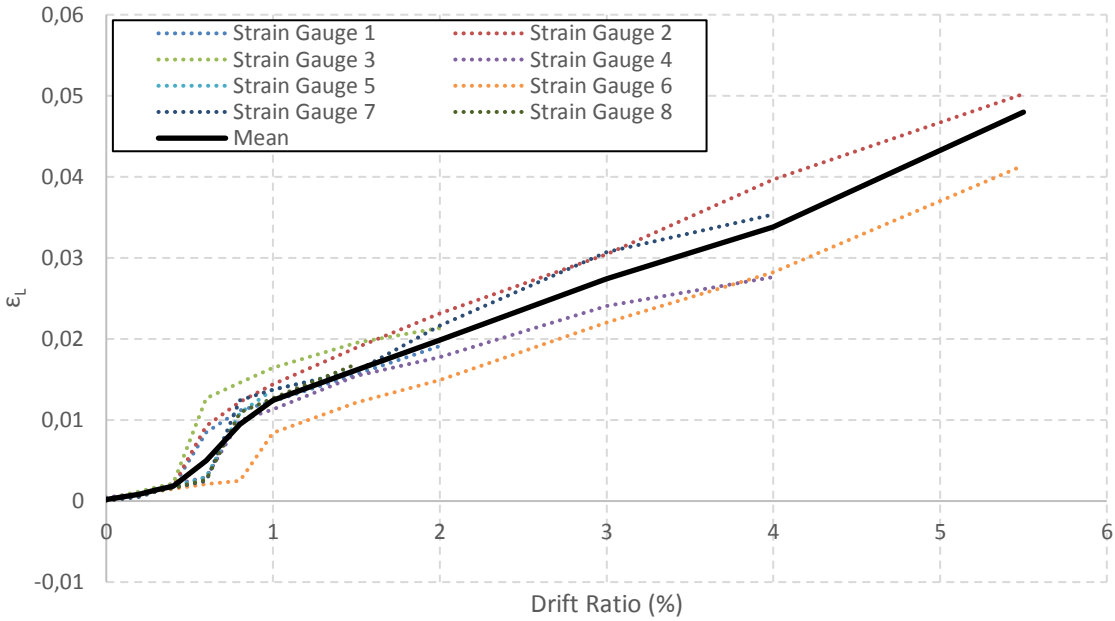

Figure A.7 Measured strain of column CH60

APPENDIX B: COLUMN GLOBAL DEFORMATION

B.1 Total Deformation

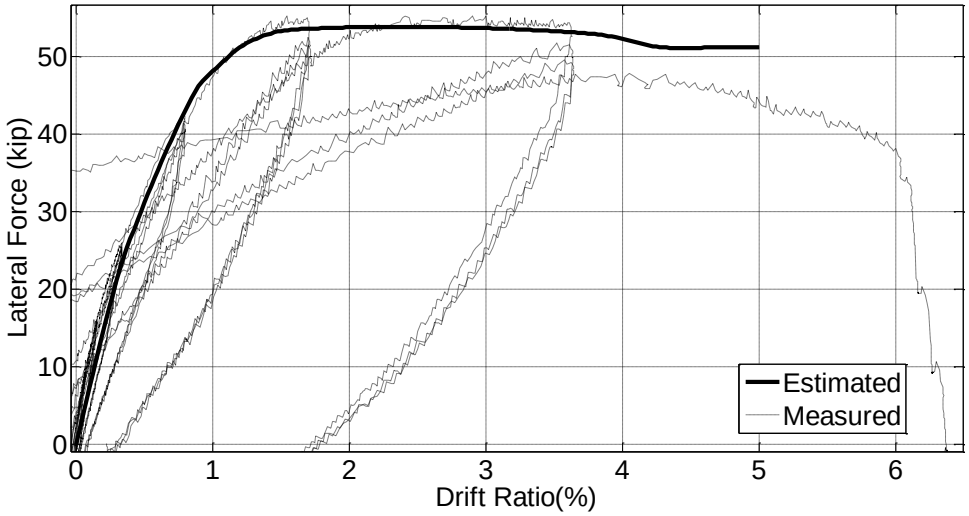

Figure B.1 2L06 total deformation

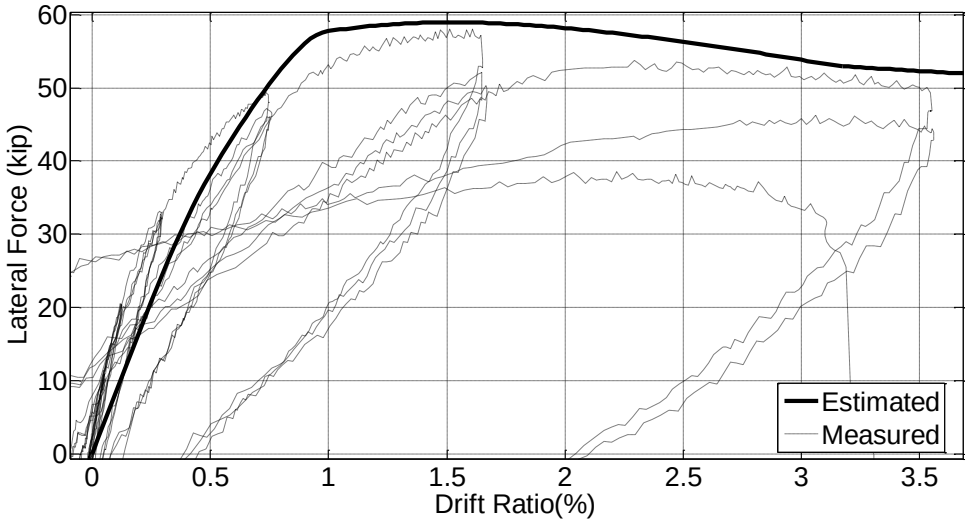

Figure B.2 2H06 total deformation

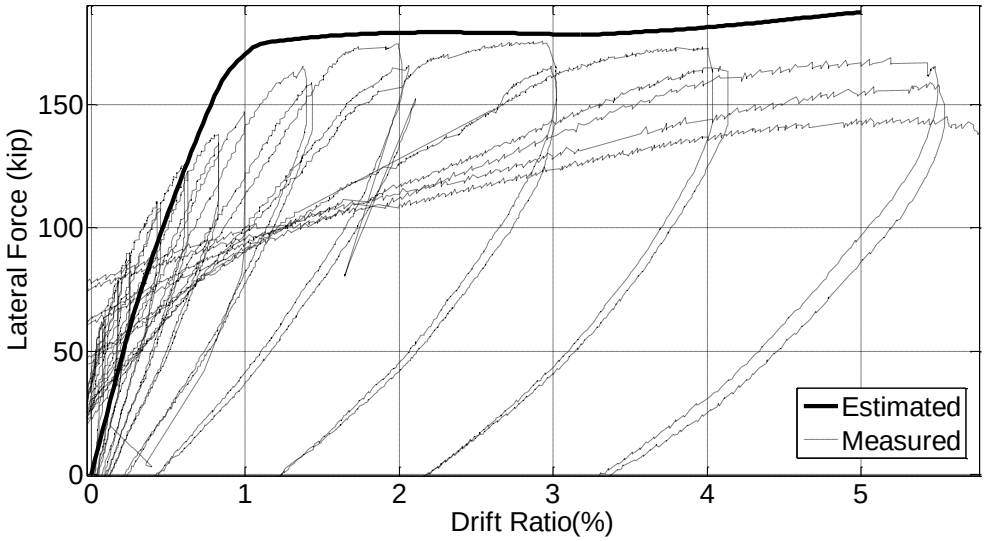

Figure B.3 CS60 total deformation

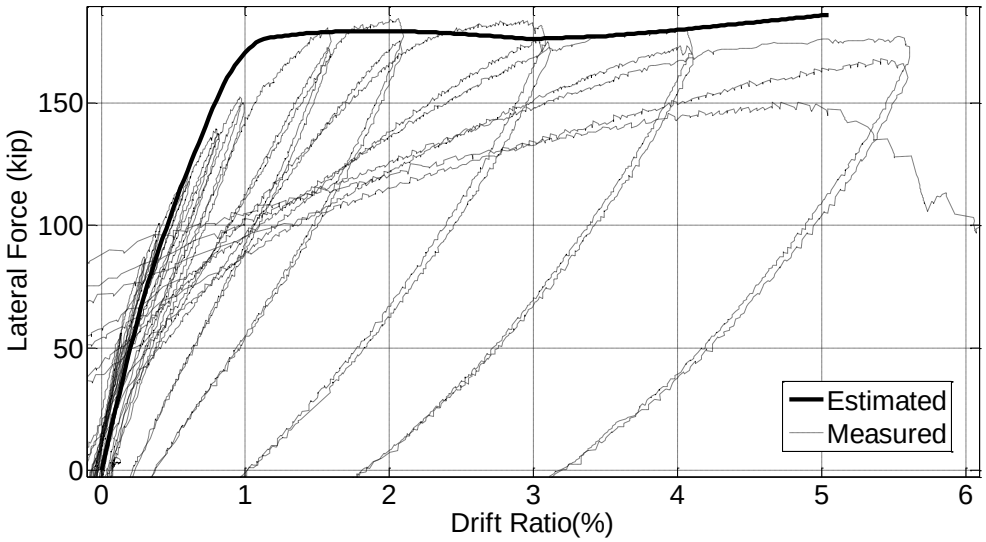

Figure B.4 CS80 total deformation

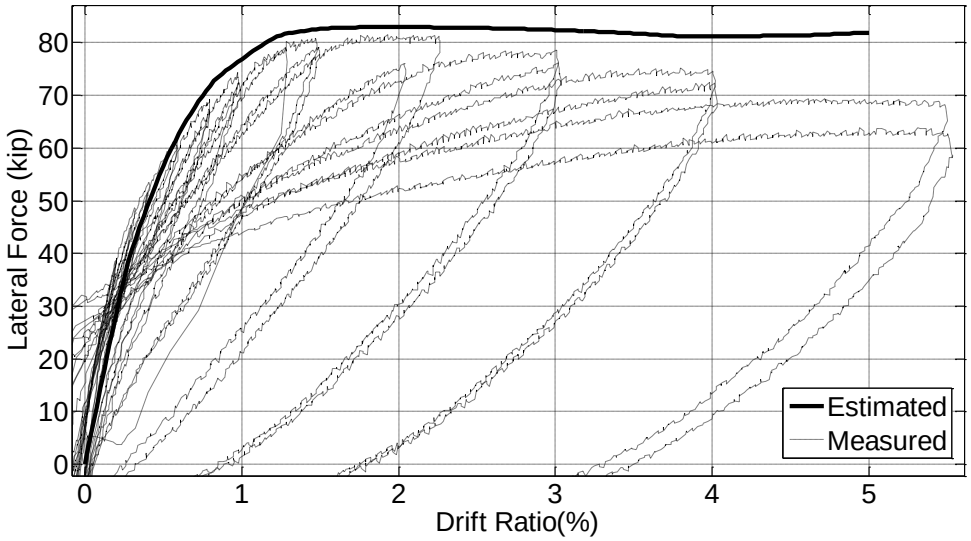

Figure B.5 CL100 total deformation

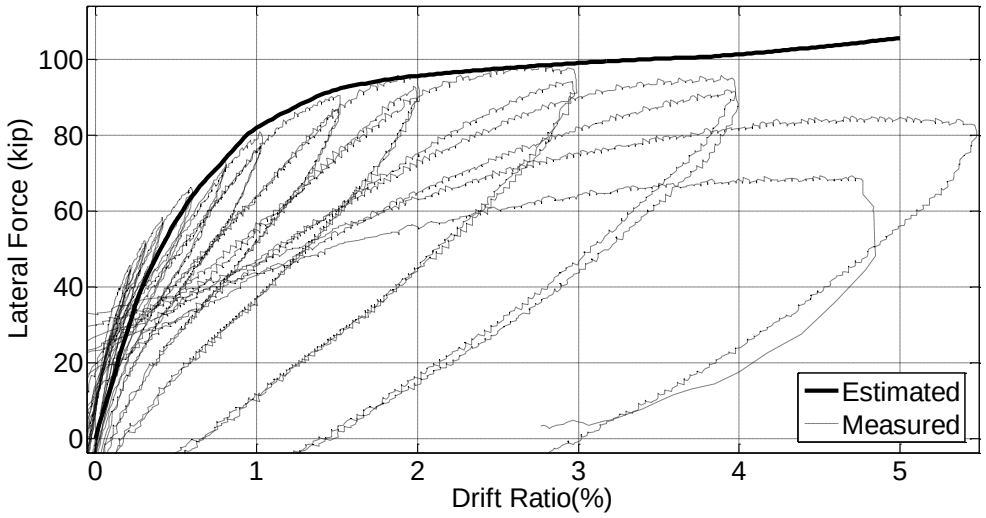

Figure B.6 CM100 total deformation

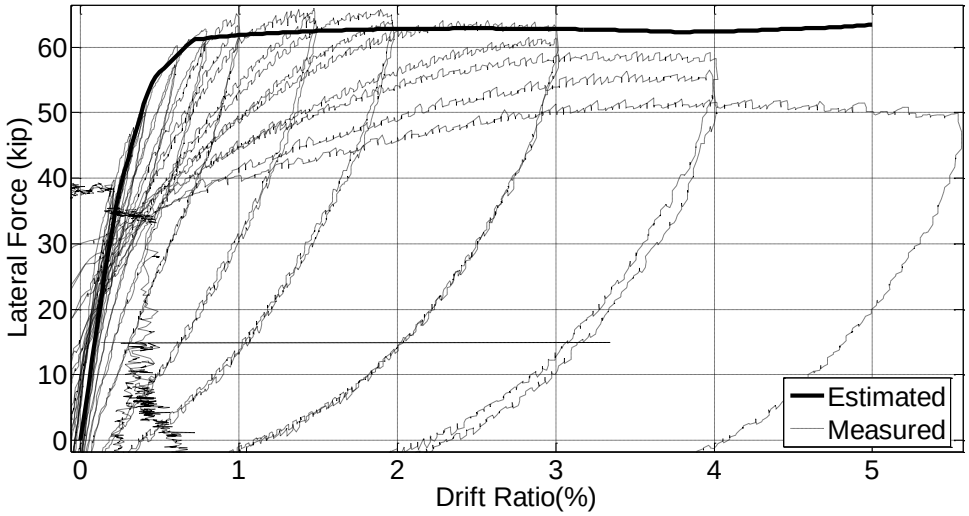

Figure B.7 CH60 total deformation

B.2 Flexural Deformation

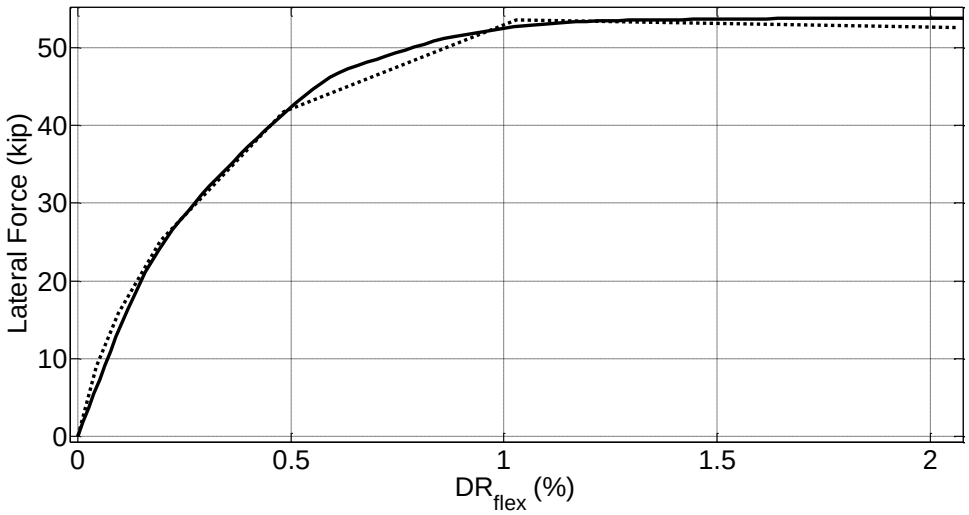

Figure B.8 2L06 flexural deformation

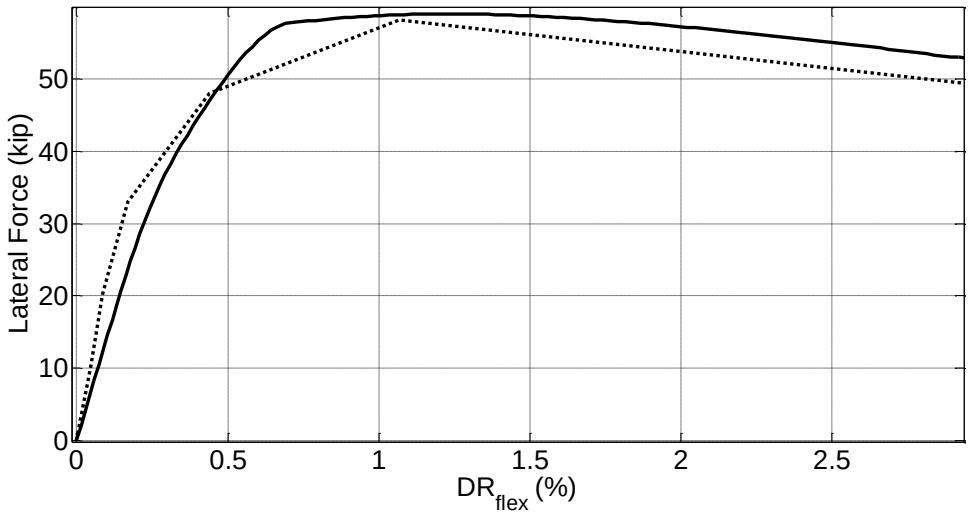

Figure B.9 2H06 flexural deformation

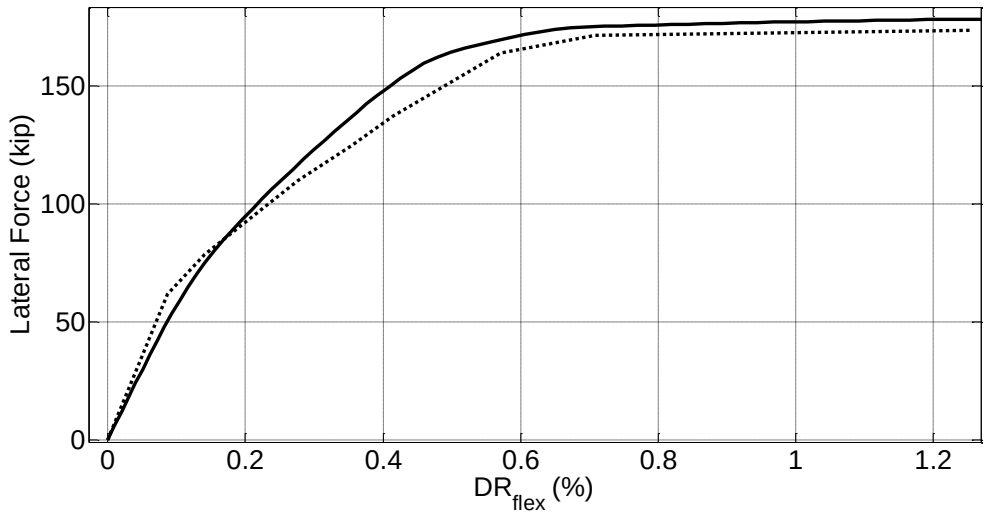

Figure B.10 CS60 flexural deformation

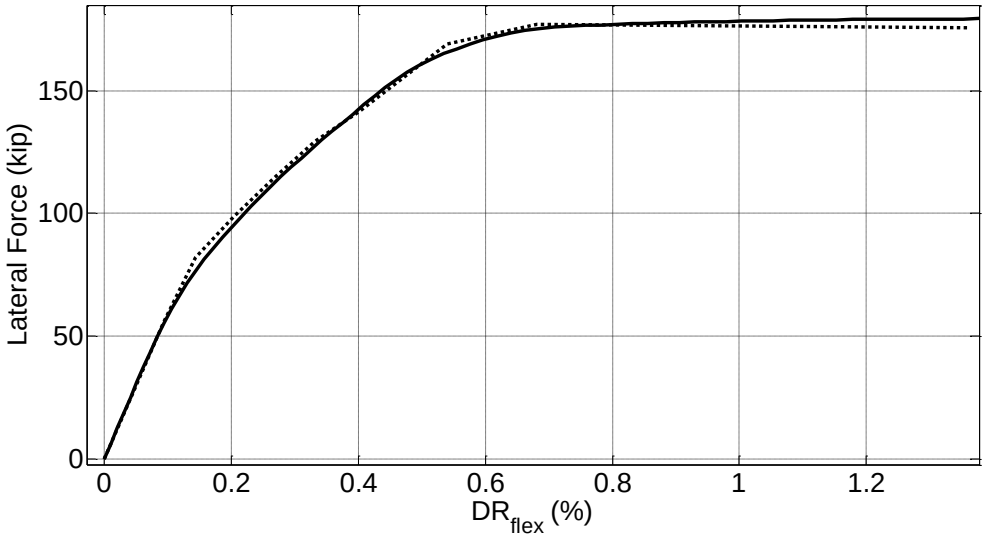

Figure B.11 CS80 flexural deformation

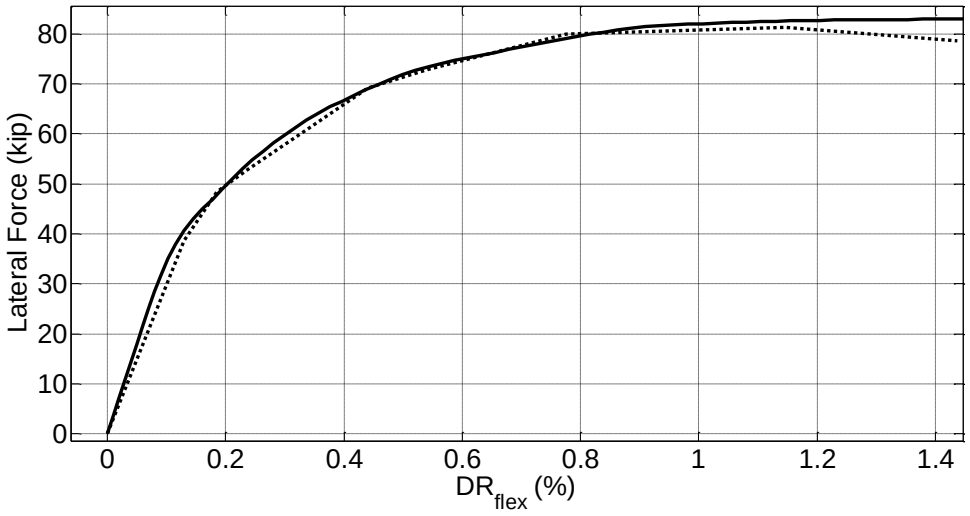

Figure B.12 CH100 flexural deformation

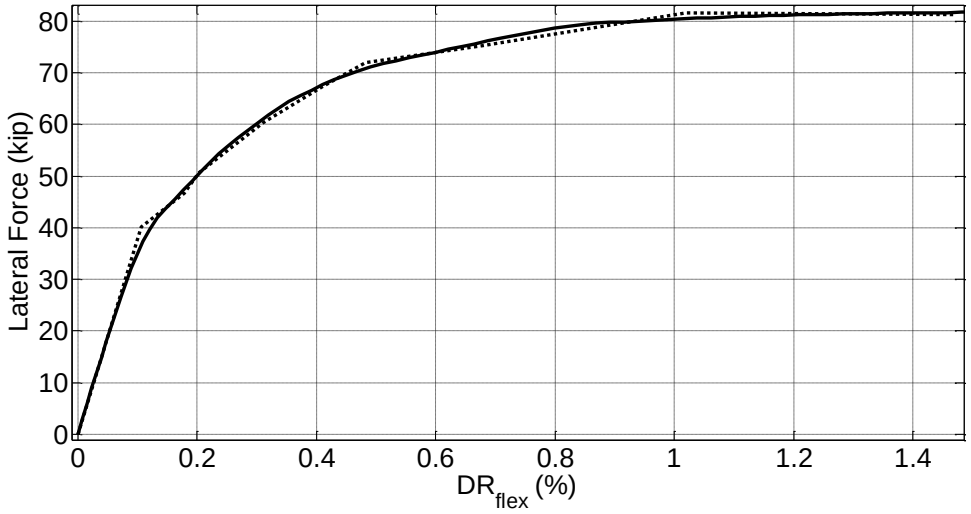

Figure B.13 CL100 flexural deformation

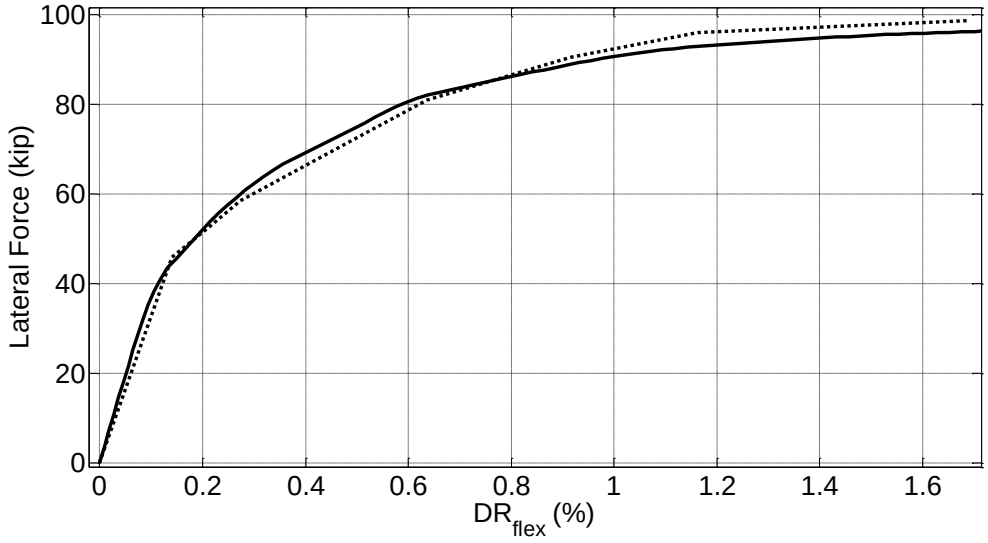

Figure B.14 CM100 flexural deformation

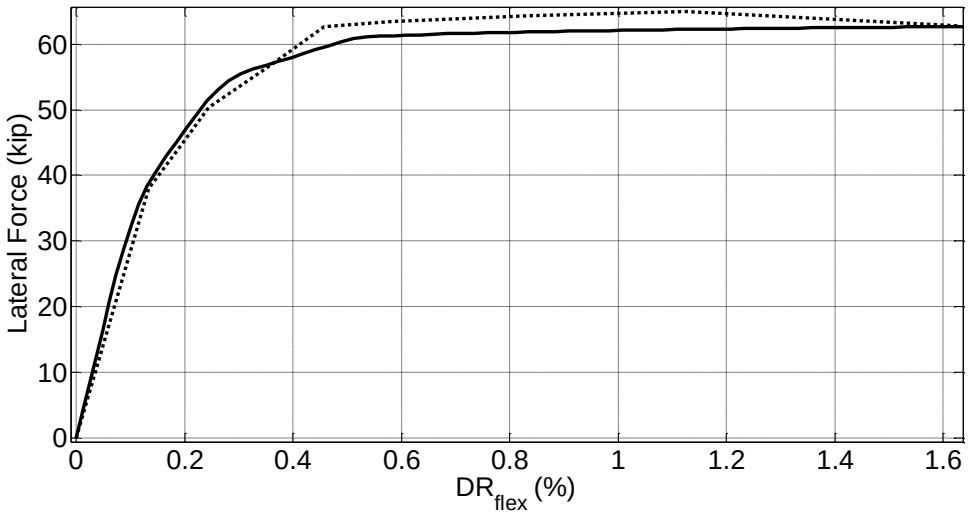

Figure B.15 CH60 flexural deformation

B.3 Barslip Deformation

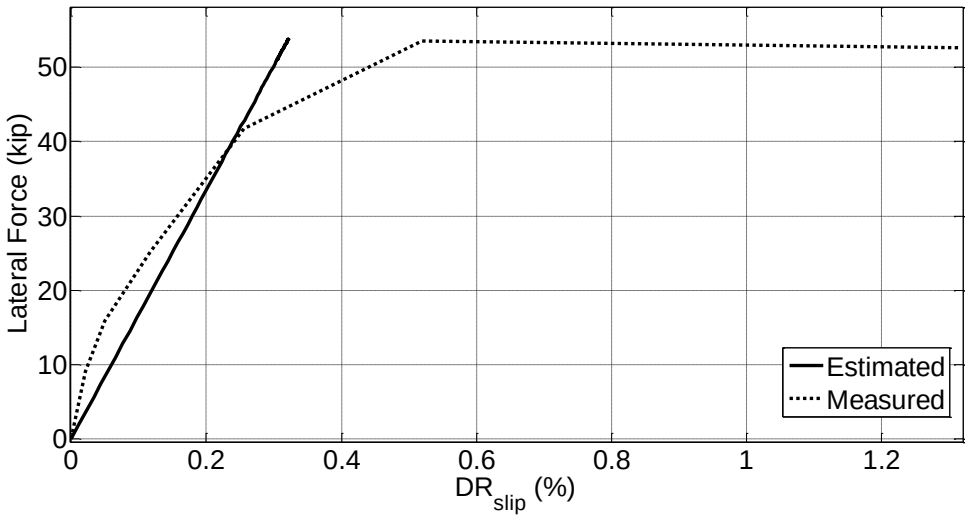

Figure B.16 2L06 barslip deformation

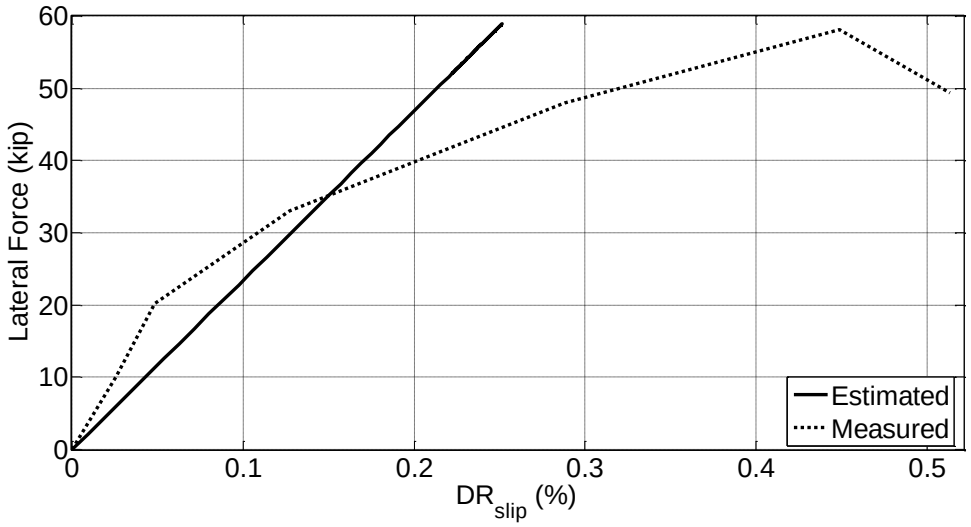

Figure B.17 2H06 barslip deformation

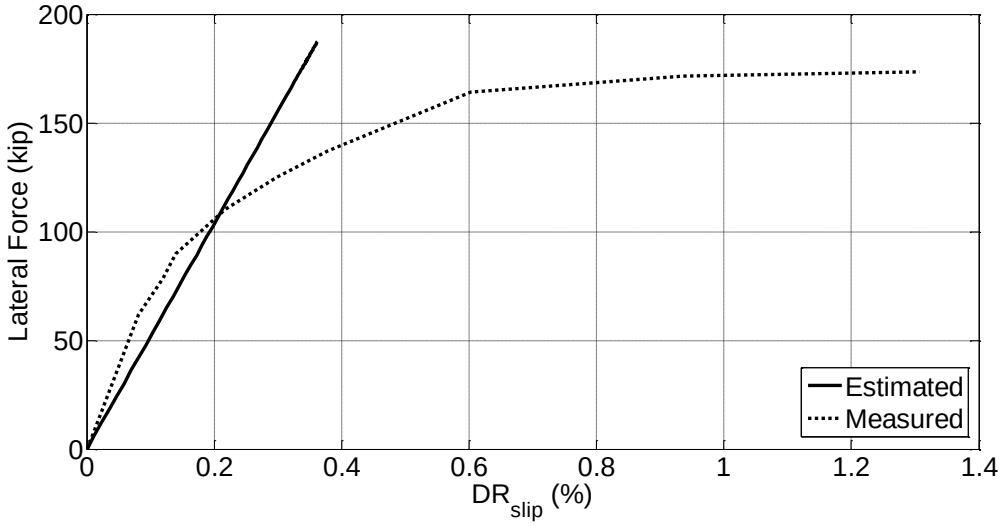

Figure B.18 CS60 barslip deformation

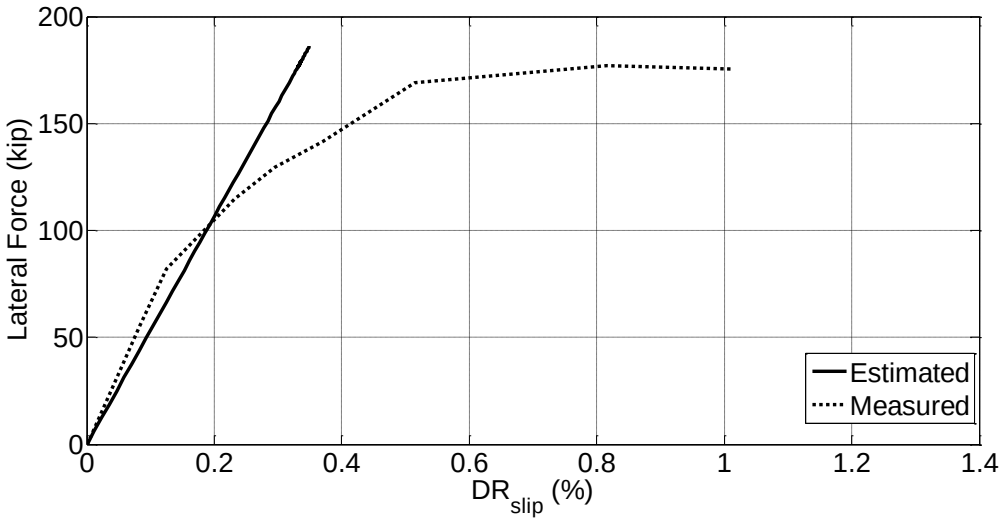

Figure B.19 CS80 barslip deformation

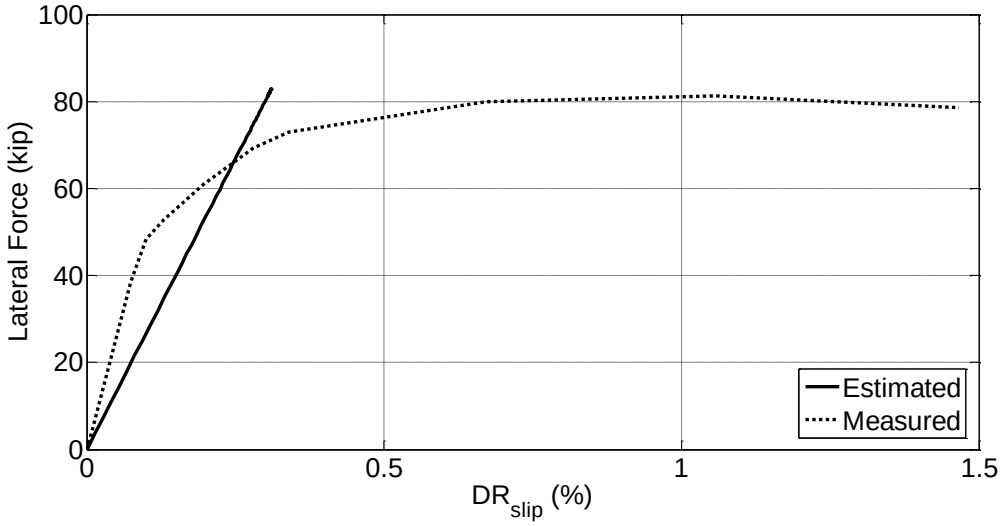

Figure B.20 CL100 barslip deformation

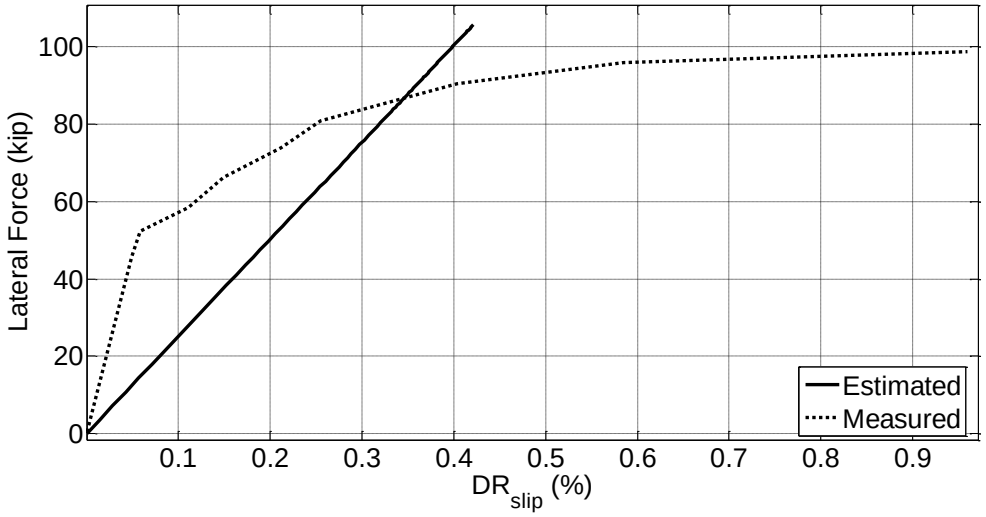

Figure B.21 CM100 barslip deformation

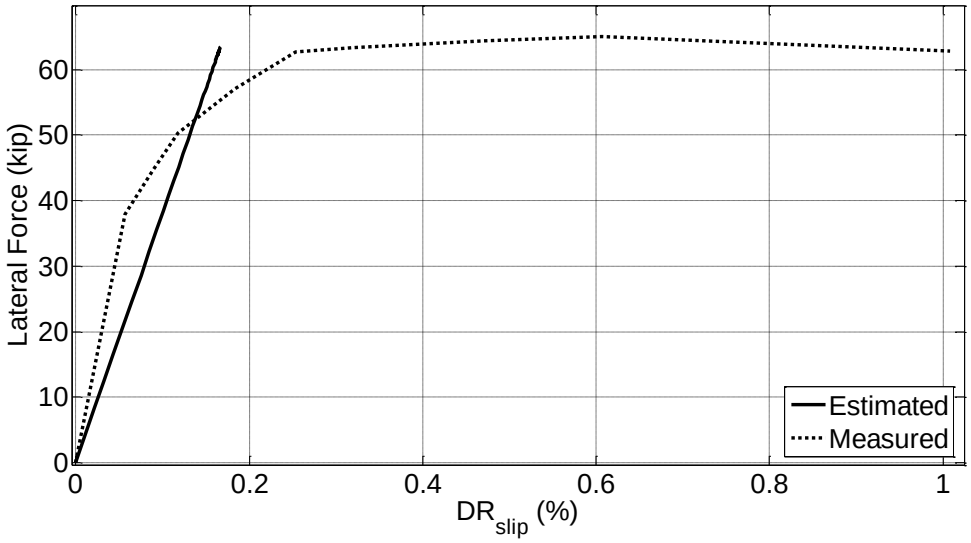

Figure B.22 CH60 barslip deformation

B.4 Shear Deformation

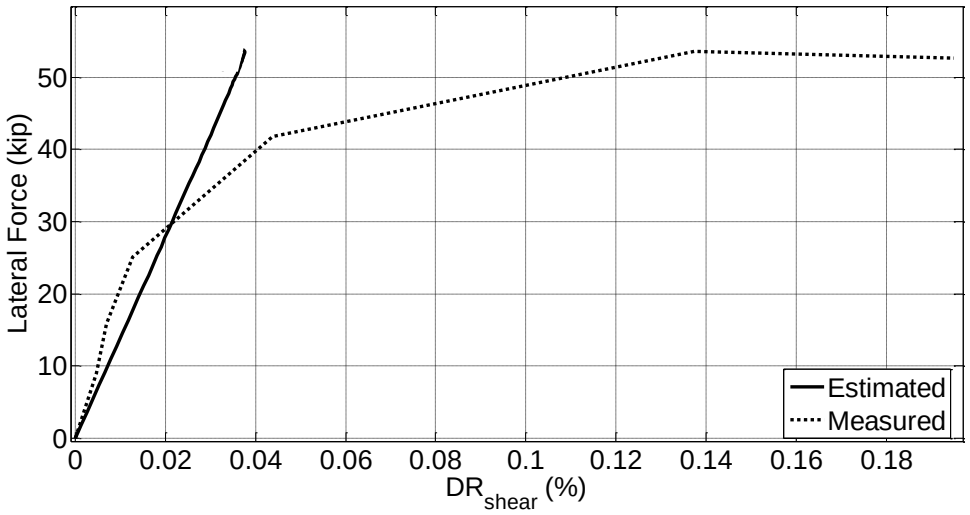

Figure B.23 2L06 shear deformation

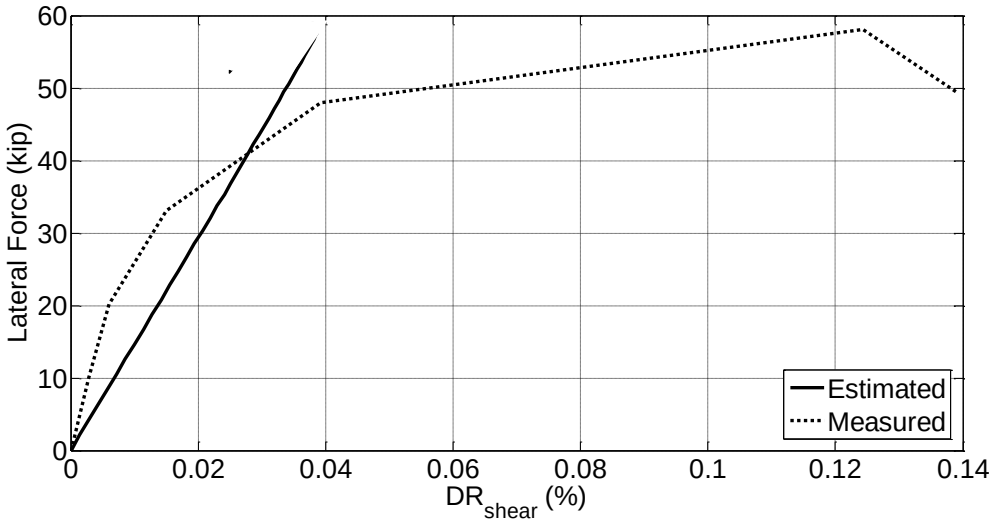

Figure B.24 2H06 shear deformation

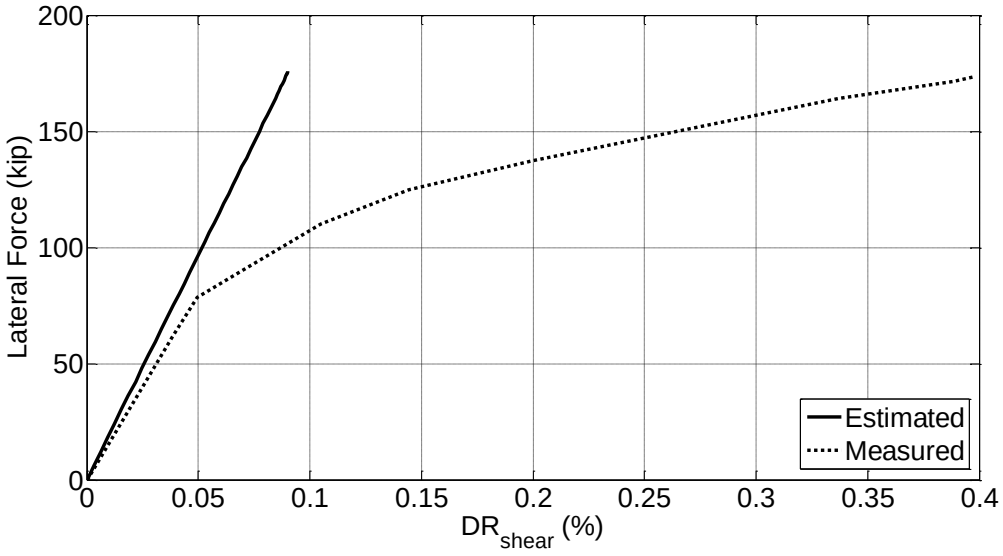

Figure B.25 CS60 shear deformation

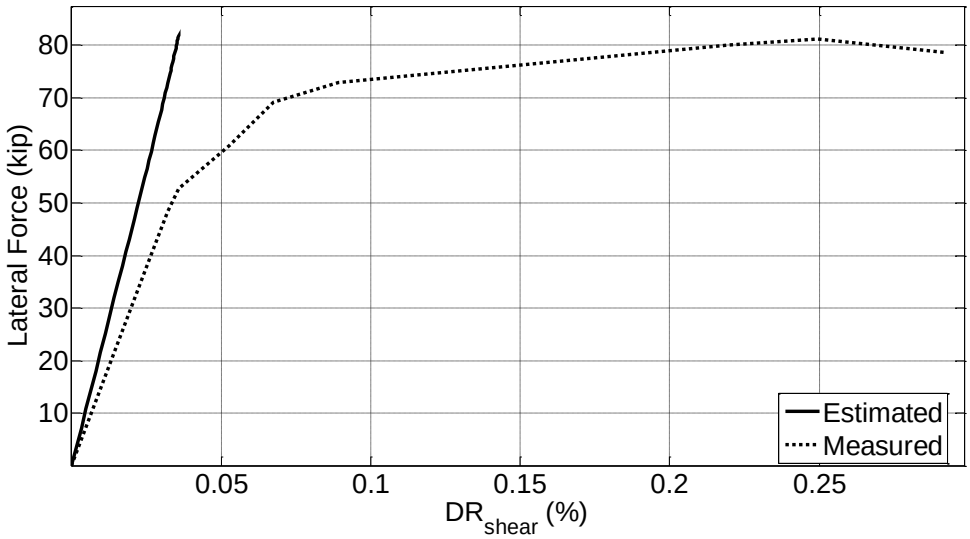

Figure B.26 CL100 shear deformation

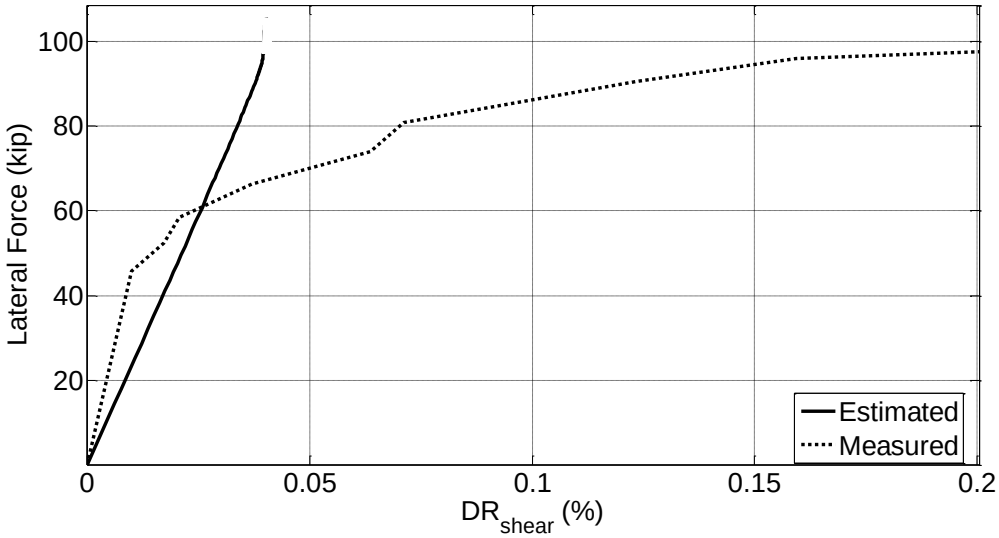

Figure B.27 CM100 shear deformation

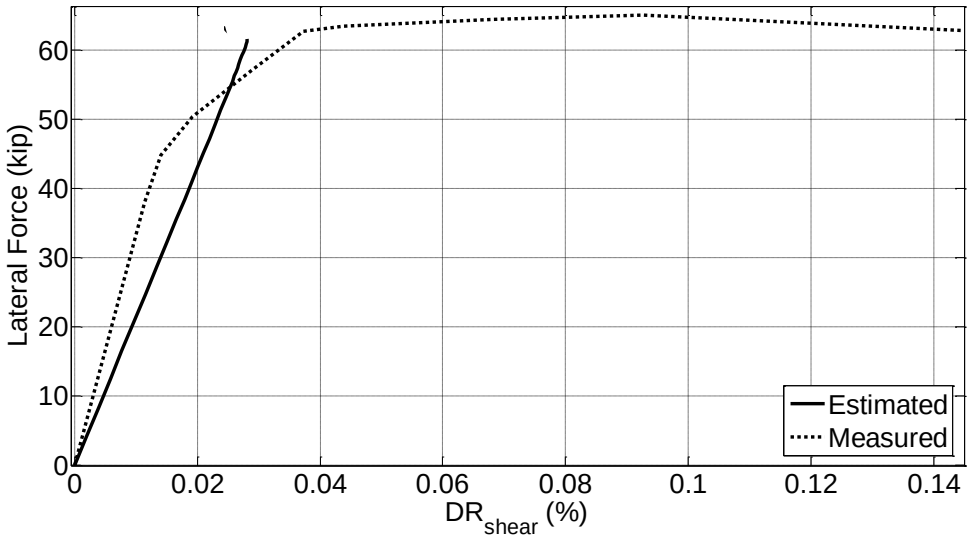

Figure B.28 CH60 shear deformation

APPENDIX C: REGRESSION ANALYSIS OF DEBONDING DRIFT

Best Subsets Regression: DRs/d versus AXR; fy/(fc)^0.5; v; s/db

Response is DRs/d

Vars	R-Sq	R-Sq (adj)	R-Sq (pred)	Mallows Cp	S	AXR	fy/(fc)^0.5	v	s/db
1	67,7	61,3	0,0	47,1	0,017634	X			
1	53,7	44,5	28,8	68,9	0,021109			X	
2	88,0	82,0	68,5	17,6	0,012006			X	X
2	84,1	76,2	24,4	23,7	0,013836	X	X		
3	98,7	97,4	90,9	3,0	0,0045466	X	X	X	
3	95,5	91,0	53,9	8,0	0,0085184	X	X		X
4	98,7	96,1	0,0	5,0	0,0055682	X	X	X	X

Regression Analysis: DRs/d versus AXR; fy/(fc)^0.5; v; s/db

Stepwise Selection of Terms

α to enter = 0,15; α to remove = 0,15

Analysis of Variance

Source	DF	Adj SS	Adj MS	F-Value	P-Value
Regression	3	0,004755	0,001585	76,68	0,002
AXR	1	0,000813	0,000813	39,32	0,008
fy/(fc)^0.5	1	0,000760	0,000760	36,76	0,009
v	1	0,000704	0,000704	34,05	0,010
Error	3	0,000062	0,000021		
Total	6	0,004817			

Model Summary

S	R-sq	R-sq(adj)	R-sq(pred)
0,0045466	98,71%	97,43%	90,85%

Coefficients

Term	Coef	SE Coef	T-Value	P-Value	VIF

Constant	0,0358	0,0151	2,37	0,099	
AXR	-0,1377	0,0220	-6,27	0,008	1,39
fy/(fc)^0.5	0,000065	0,000011	6,06	0,009	1,11
v	-0,004035	0,000692	-5,83	0,010	1,29

Regression Equation

DRs/d = 0,0358 - 0,1377 AXR + 0,000065 fy/(fc)^0.5 - 0,004035 v

Fits and Diagnostics for Unusual Observations

Obs	DRs/d	Fit	Resid	Std Resid	
2	0,03341	0,03351	-0,00011	-0,26	X

X Unusual X

APPENDIX D: REGRESSION ANALYSIS OF SCALE FACTOR

Best Subsets Regression: SFc versus P/Po; T/Y; rhoL; v/sqrt(fc); (lb/ld)

Response is SFc

Vars	R-Sq	R-Sq (adj)	R-Sq (pred)	Mallows Cp	S	P/Po	T/Y	rho	v/sqrt(fc)	(lb/ld)
1	54,7	47,2	22,6	2,9	0,082566			X		
1	44,2	34,9	1,3	4,5	0,091662				X	
2	70,7	59,0	47,9	2,4	0,072731			X		X
2	62,2	47,1	0,0	3,7	0,082586		X		X	
3	83,4	70,9	0,0	2,5	0,061266		X		X	X
3	76,7	59,3	25,7	3,5	0,072494	X		X		X
4	86,1	67,6	0,0	4,1	0,064633	X	X		X	X
4	84,0	62,6	0,0	4,4	0,069509		X	X	X	X
5	86,8	53,8	0,0	6,0	0,077189	X	X	X	X	X

Regression Analysis: SFc versus (T/Y-1); v/sqrt(fc); (lb/ld)

Analysis of Variance

Source	DF	Adj SS	Adj MS	F-Value	P-Value
Regression	3	0,07530	0,025099	6,69	0,049
(T/Y-1)	1	0,03395	0,033952	9,05	0,040
v/sqrt(fc)	1	0,04776	0,047764	12,73	0,023
(lb/ld)	1	0,01909	0,019088	5,09	0,087
Error	4	0,01501	0,003753		
Total	7	0,09031			

Model Summary

S	R-sq	R-sq(adj)	R-sq(pred)
0,0612656	83,38%	70,91%	0,00%

Coefficients

Term	Coef	SE Coef	T-Value	P-Value	VIF
Constant	1,105	0,238	4,65	0,010	
(T/Y-1)	-0,492	0,164	-3,01	0,040	1,51
v/sqrt(fc)	-0,0590	0,0165	-3,57	0,023	4,18
(lb/ld)	-0,0792	0,0351	-2,26	0,087	4,68

Regression Equation

SFc = 1,105 - 0,492 (T/Y-1) - 0,0590 v/sqrt(fc) - 0,0792 (lb/ld)

APPENDIX E: OPENSEES SCRIPT

```
wipe
model BasicBuilder -ndm 2 -ndf 3
node 1 0 0
node 2 0 0
node 3 0 108
node 4 0 108

fix 1 1 1 1
fix 2 0 0 0
fix 3 0 0 0
fix 4 0 0 1

equalDOF 1 2 2
equalDOF 4 3 2

set ft 0.51581
set Et 473
set et 0.002181
set rs 87.7863
set Cr 1
set Ct 1
set fcc -7.4734
set ec0c -0.011
set ecuc -0.034
set Ec 3503.7037
set fc -4.73
set ec0 -0.0027
set fcu -0.946
set ecu -0.023936

uniaxialMaterial Concrete04 1 $fcc $ec0c $ecuc $Ec $ft $et 0.1
uniaxialMaterial Concrete02 2 $fc $ec0 $fcu $ecu 0.3 $ft $Et

set fy 64.4
set E 29000
set b 0.0086

uniaxialMaterial Steel02 3 $fy $E [expr $b]

set Kr 2055500.9808
set Kv 3920.1747

uniaxialMaterial Elastic 4 $Kr
uniaxialMaterial Elastic 5 $Kv

set colWidth 18
set colDepth 18
set cover 1.875
set As 0.44179
```

```
set spacing 7.125
set y1 9
set z1 9

section Fiber 1 {
patch rect 1 10 1 [expr $cover-$y1] [expr $cover-$z1] [expr $y1-$cover]
[expr $z1-$cover]
patch rect 2 10 1  [expr -$y1] [expr $z1-$cover] $y1 $z1
patch rect 2 10 1  [expr -$y1] [expr -$z1] $y1 [expr $cover-$z1]
patch rect 2 2 1  [expr -$y1] [expr $cover-$z1] [expr $cover-$y1] [expr
$z1-$cover]
patch rect 2 2 1  [expr $y1-$cover] [expr $cover-$z1] $y1 [expr $z1-
$cover]
layer straight 3 3 $As [expr $cover-$y1] [expr $z1-$cover] [expr
$cover-$y1] [expr $cover-$z1]
layer straight 3 2 $As 0.0 [expr $z1-$cover] 0.0 [expr $cover-$z1]
layer straight 3 3 $As [expr $y1-$cover] [expr $z1-$cover] [expr $y1-
$cover] [expr $cover-$z1]
}

geomTransf PDelta 1

element forceBeamColumn 1 2 3 5 1 1
element zeroLength 2 1 2 -mat 5 4 -dir 1 3
element zeroLength 3 4 3 -mat 5 4 -dir 1 3


pattern Plain 1 Linear {
load 4 0 -230 0
}
constraints Plain
numberer Plain
system BandGeneral
test NormUnbalance 1e-05 100
algorithm Newton
integrator LoadControl 1
analysis Static
analyze 1
loadConst -time 0.0
puts "DoneAxialLoad"
set IDctrlNode  4
set IDctrlDOF 1
set Dmax 5.4
set Dincr 0.027
pattern Plain 2 Linear {
load 4 100 0.0 0.0
}
constraints Plain
numberer Plain
system BandGeneral
set Tol  1e-05
set maxNumIter 1000
```

```
set printFlag 0
set TestType EnergyIncr
test $TestType $Tol $maxNumIter $printFlag
set algorithmType Newton
algorithm $algorithmType
integrator DisplacementControl $IDctrlNode   $IDctrlDOF $Dincr
analysis Static
set Nsteps  200
set ok [analyze $Nsteps]
if {$ok != 0} {
puts "start logical function"
set ok 0
set controlDisp 0.0
set D0 0.0
set Dstep [expr ($controlDisp-$D0)/($Dmax-$D0)]
while {$Dstep < 1.0 && $ok == 0} {
set controlDisp [nodeDisp $IDctrlNode $IDctrlDOF ]
set Dstep [expr ($controlDisp-$D0)/($Dmax-$D0)]
set ok [analyze 1 ]
if {$ok != 0} {
puts "Trying Newton with Initial Tangent .."
test NormDispIncr   $Tol 2000  0
algorithm Newton -initial
set ok [analyze 1 ]
algorithm $algorithmType
}
if {$ok != 0} {
puts "Trying Broyden .."
algorithm Broyden 8
set ok [analyze 1 ]
algorithm $algorithmType
}
if {$ok != 0} {
puts "Trying NewtonWithLineSearch .."
algorithm NewtonLineSearch .8
set ok [analyze 1 ]
algorithm $algorithmType
}
}
}
puts "DonePushover"
```

APPENDIX F: COMPARISON OF PUSHOVER AND CYCLIC ANALYSIS

Global lateral responses and longitudinal bar tension strain responses are compared for pushover and cyclic analyses. As can be seen in Figure F.1 to Figure F.3, differences in global response and strain demands obtained from cyclic and pushover analyses were insignificant. Thus, the pushover analyses were preferred and their results presented in the thesis.

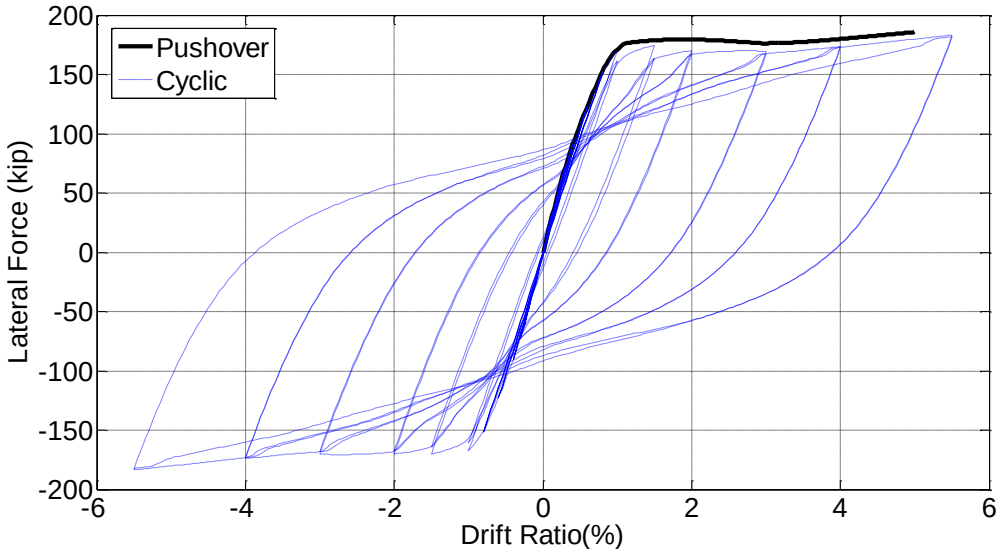

Figure F.1 CS80 pushover and cyclic global lateral response

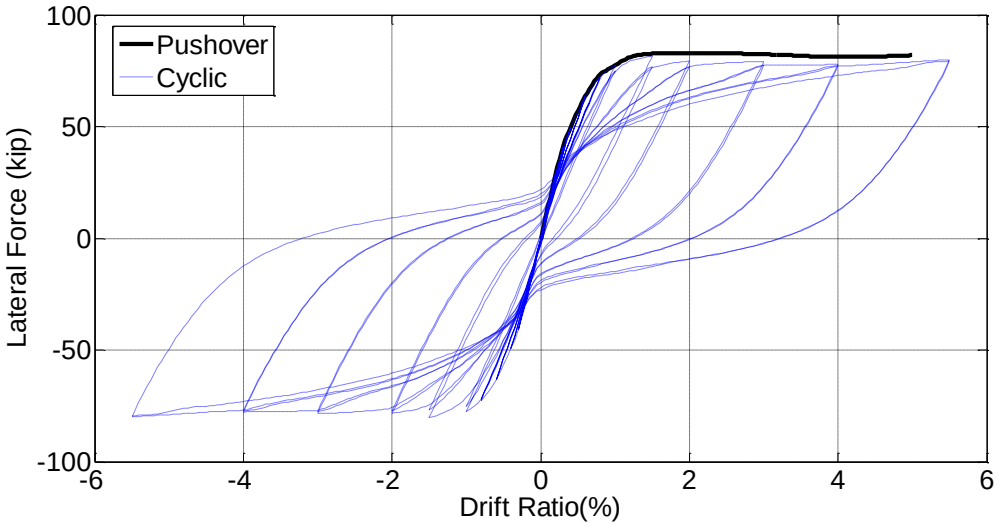

Figure F.2 CL100 pushover and cyclic global lateral response

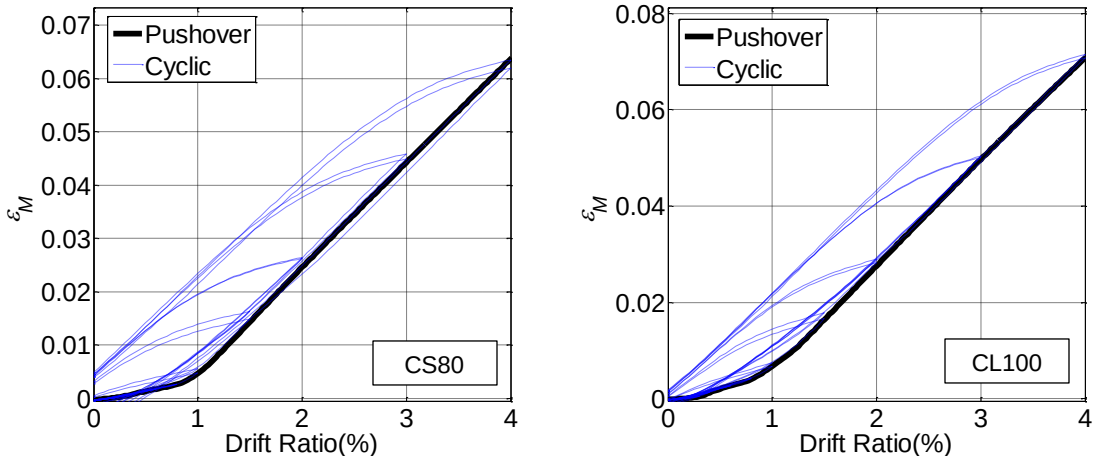

Figure F.3 Comparison of pushover and cyclic analyses in longitudinal bar tension strain response

APPENDIX G: COMPARISON BETWEEN STEEL02 AND REINFORCING STEEL MATERIAL MODELS

The comparison of Steel02 and Reinforcing Steel material models demonstrated insignificant response differences for both high shear – high axial load columns (e.g., CS80) and low shear – low axial load columns (e.g., CL100) in Figure G.1. The Steel02 material model was preferred because the model is commonly used in both commercial and research software.

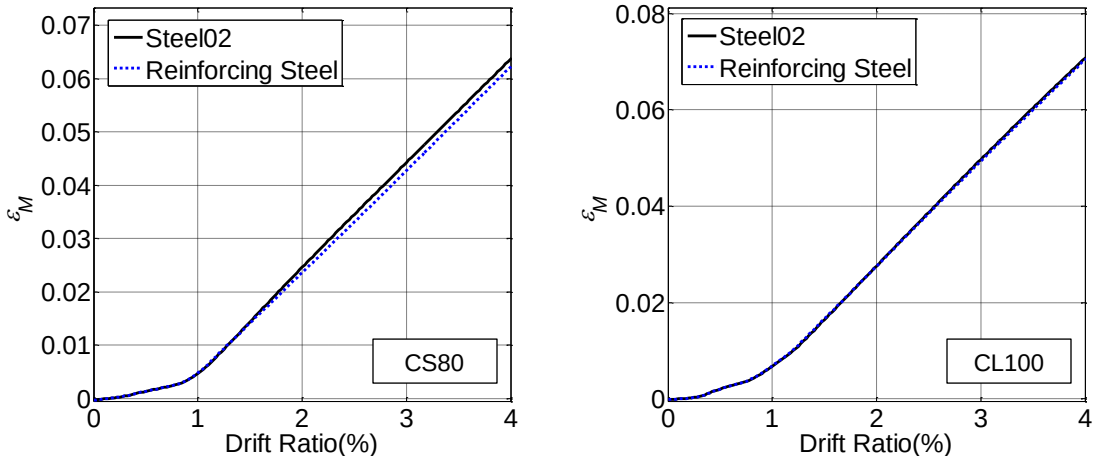

Figure G.1 Tension strain comparison of Steel02 and Reinforcing Steel

REFERENCES

ACI (American Concrete Institute) Committee 318, “Building code requirement for structural concrete (ACI 318-56),” American Concrete Institute, Detroit, MI, 1956.

ACI Committee 318, “Building code requirement for structural concrete (ACI 318-71),” American Concrete Institute, Detroit, MI, 1971.

ACI Committee 318, “Building Code Requirements for Structural Concrete (ACI 318-14) and Commentary (ACI 318R-14),” American Concrete Institute, Farmington Hills, MI, 2014, 519 pp.

ACI Committee 408, “Suggested Development, Splice, and Standard Hook Provisions for Deformed Bars,” *Concrete International,* V. 1, No. 7, July 1979, pp. 44-46.

Addessi, D and Ciampi, V., “A regularized force-based beam element with a damage-plastic section constitutive law,” *International Journal for Numerical Methods in Engineering,* V. 70, No. 5, 2007, pp. 610–629.

Alsiwat, J. M., and Saatcioglu, M., “Reinforcement Anchorage Slip under Monotonic Loading,” *Journal of Structural Engineering*, ASCE, V. 118, No. 9, Sept 1992, pp. 2421-2438.

Aoyama, H., “Design of Modern High-rise Reinforced Concrete Structures,” *Imperial College Press*, London, United Kingdom, 2001.

ASCE (American Society of Civil Engineers), *Minimum Design Loads for Buildings and Other Structures*, ASCE 7-10, ASCE, Reston, VA, 2010.

ASTM A370-16, “Standard Test Methods and Definitions for Mechanical Testing of Steel Products,” ASTM International, West Conshohocken, PA, 2016.

ASTM A615 / A615M-16, “Standard Specification for Deformed and Plain Carbon-Steel Bars for Concrete Reinforcement,” ASTM International, West Conshohocken, PA, 2016.

ASTM A706 / A706M-16, “Standard Specification for Deformed and Plain Low-Alloy Steel Bars for Concrete Reinforcement,” ASTM International, West Conshohocken, PA, 2016.

ASTM A1035 / A1035M-16a, “Standard Specification for Deformed and Plain, Low-Carbon, Chromium, Steel Bars for Concrete Reinforcement,” ASTM International, West Conshohocken, PA, 2016.

ASTM C39 / C39M-16a, “Standard Test Method for Compressive Strength of Cylindrical Concrete Specimens,” ASTM International, West Conshohocken, PA, 2016.

ASTM E8 / E8M-15a, “Standard Test Methods for Tension Testing of Metallic Materials,” ASTM International, West Conshohocken, PA, 2015.

Baker, A., and Amarakone, A., “Inelastic hyperstatic frames analysis,” *ACI Special Publication*, No. 12, 1965, pp. 85-142.

Benzoni, G.; Ohtaki, T.; Priestley, M. J. N.; and Seible, F., “Seismic Performance of Circular Reinforced Concrete Columns under Varying Axial Load,” SSRP 96/04, Structural Systems Research, University of California-San Diego, La Jolla, CA, 1996.

Berry, M. P., and Eberhard, M. O., “Performance Modeling Strategies for Modern Reinforced Concrete Bridge Columns,” PEER-2007/07, Pacific Earthquake Engineering Research Center, University of California-Berkeley, Berkeley, CA, 2007, 213 pp.

Berry, M.P., D.E. Lehman and L.N. Lowes. “Lumped-Plasticity Models for Performance Simulation of Bridge Columns.” *ACI Structural Journal*, V. 105, No. 3, 2008, pp. 270-279.

Brown, Jeff, Kunnath, Sashi K., “Low-Cycle Fatigue Failure of Reinforcing Steel Bars,” *ACI Materials Journal* 6.110, 2004, pp. 457-65.

Caifu, Y., “Development of high strength construction rebars,” Proceedings, International Seminar on Production and Application of High Strength Seismic Grade Rebar Containing Vanadium, Central Iron & Steel Research Institute, Beijing, China, 2010.

Coleman, J., and Spacone, E., “Localization issues in force-based frame elements.” *J. Struct. Eng.*, V. 127, No. 11, 2001, pp. 1257–1265.

Corley, W. G., “Rotational capacity of reinforced concrete beams,” *Proceedings of the American Society of Civil Engineers*, ST 5, 1966, pp. 121-146.

El-Bahy, A., Kunnath, S.K., Stone, W.C. and Taylor, A.W., “Cumulative Seismic Damage of Circular Bridge Columns: Benchmark and Low-Cycle Fatigue Tests,” *ACI Structural Journal*, Vol.96, No.4, 1999, pp. 633-641.

Elwood, K. J., and Eberhard, M. O., “Effective stiffness of reinforced concrete columns”, *ACI Structural Journal*, Vo. 106, No. 4, 2009, pp. 476-484.

Erasmus, L., and Pussegoda, N., “Safe bend radii for deformed reinforcing bar to avoid failure by strain age embrittlement,” *New Zealand Engineering*, Vol. 33, No. 8, 1978, pp. 170-177.

Ghannoum, W. M., and Moehle, J. P., “Shake-Table Tests of a Concrete Frame Sustaining Column Axial Failures,” *ACI Structural Journal*, V. 109, No. 3, May-June 2012, pp. 393-402.

Ghannoum, W. M and Moehle, J. P., "Dynamic collapse analysis of a concrete frame sustaining column axial failures", *ACI Structural Journal*, Vol. 109, No. 3, 2012, pp. 403-412.

Ghannoum, W.M., Moehle, J.P., Bozorgnia, Y., "Analytical Collapse Study of Lightly Confined Reinforced Concrete Frames Subjected to Northridge Earthquake Ground Motions," *Journal of Earthquake Engineering*, V. 12, No. 7, October 2008, pp. 1105-1119.

Gladman, T., "The physical metallurgy of microalloyed steels" London, Institute of Materials, 1997.

Harajli, M, "Bond Stress-Slip Model for Steel Bars in Unconfined or Steel, FRC, or FRP Confined Concrete under Cyclic Loading," *Journal of Structural Engineering*, Vol. 135, No. 5, 2009, pp. 509-518.

Jansen, D. C., and Shah, S. P, ''Effect of length on compressive strain-softening of concrete,'' *J. Engrg. Mech.*, ASCE, V. 123, No. 1, 1997, pp. 25–35.

Kaba, S. and Mahin, S. A., "Refined Modeling of Reinforced Concrete Columns for Seismic Analysis," *EERC Report 84-03*, Earthquake Engineering Research Center, University of California, Berkeley, 1984.

Kent, D. C., and Park, R., "Flexural members with confined concrete," *J. Struct. Div. ASCE*, V. 97, No. 7, 1971, pp. 1969–1990.

Kwon, Jinhan, "Strength, Stiffness, and Damage of Reinforced Concrete Buildings Subjected to Seismic Motions," Ph.D. Dissertation, The University of Texas at Austin, Austin, Texas, May 2016.

LeBorgne, M.R., "Modeling The Post Shear Failure Behavior of Reinforced Concrete Columns," Ph.D. Dissertation, The University of Texas at Austin, Austin, Texas, May 2012.

Lehman, D. E., and Moehle, J. P., "Seismic Performance of Well-Confined Concrete Bridge Columns," PEER-1998/01, Pacific Earthquake Engineering Research Center, University of California-Berkeley, Berkeley, CA, 1998, 316 pp.

Lowes, L. N., Mitra, N., and Altoontash, A., "A Beam-Column Joint Model for Simulating the Earthquake Response of Reinforced Concrete Frames," 2003/10, UCB/PEER, University of California, Berkeley, CA, 2003, 59 pp.

Macchi, G., Pinto, P. E., and Sanpaolesi, L., "Ductility requirements for reinforcement under Eurocodes," Structural Engineering International, Vol. 6 No. 4, 1996, pp. 249-254.

Mander. J. B., Priestley, M. J. N., Park, R., "Theoretical stress-strain model for confined concrete," *Journal of Structural Engineering*, Vol. 114, No. 8, 1988, pp. 1804-1826.

Menegotto M., Pinto P.E., "Method of analysis for cyclically loaded R.C. frames including changes in geometry and non-elastic behavior of elements under combined normal force and bending," Istituto di Scienza e Tecnica delle Costruzioni, University of Rome, Report 32, October 1972.

Mendis, P., "Plastic Hinge Lengths of Normal and High-Strength Concrete in Flexure," Advances in Structural Engineering, Vol. 4, No. 4, 2001, 189-195.

MMFX Technologies Corporation, "Material Properties and Design Considerations MMFX$_2$ (ASTM A1035/AASHTO MP18)," MMFX Product Information, December 2012, 36 pp.

Neuenhofer, A., and Filippou, F. C., "Evaluation of nonlinear frame finite-element models." *J. Struct. Eng.*, 123(7), 1997, pp. 958–966.

OpenSees, Version 2.4.5, http://opensees.berkeley.edu, accessed May. 13, 2015.

Otani, S., and Sozen, M. A., "Behavior of Multistory Reinforced Concrete Frames during Earthquakes," *Structural Research Series* No. 392, University of Illinois at Urbana-Champaign, Urbana, IL, 1972, 551 pp.

Park, R. and Paulay, T., *Reinforced Concrete Structures*. New York: John Wiley and Sons, Inc, 1975, 744 pp.

Priestley, M. J. N., Seible, F., and Calvi, G. M., *Seismic Design and Retrofit of Bridges*, John Wiley and Sons, Inc., New York, 1996, 101 pp.

Rautenberg, J.M., "Drift Capacity of Concrete Columns Reinforced with High Strength Steel," Ph.D. Thesis, Purdue University, West Lafayette, Indiana, 2011.

Rautenberg, J.M., Pujol, S., Tavallali, H., Lepage, A., "Reconsidering the use of high-strength reinforcement in concrete columns," *Engineering Structures*, No. 37, 2012, pp. 135-142.

Rautenberg, J.M., Pujol, S., Tavallali, H., Lepage, A., "Drift Capacity of Concrete Columns Reinforced with High Strength Steel," *ACI Structural Journal*, Vol. 110, No. 2, 2013, pp. 307-318.

Restrepo-Posada, J.I., "Seismic Behaviour of Connections Between Precast Concrete Elements," Ph.D. Thesis, University of Canterbury, Christchurch, New Zealand, 1992.

Scott, M. H., and Fenves G. L., "Plastic hinge integration methods for force-based beam–column elements. *Journal of Structural Engineering*," V. 132, No. 2, 2006, pp. 244–252.

Slavin, C.M., Ghannoum, W.M., “Defining Structurally Acceptable Properties of High-Strength Steel Bars through Material and Column Testing, PART I: MATERIAL TESTING REPORT,” (05-14), Charles Pankow Foundation, August 2015, pp. 135.

Sokoli, D., Shekarchi, W., Buenrostro, E., Ghannoum, W. M., “Advancing Behavioral Understanding and Damage Evaluation of Concrete Members Using High-Resolution Digital Image Correlation Data,” *Earthquakes and Structures*, 7(5), 2014.

Sokoli, D., “Seismic Performance of Concrete Columns Reinforced with High Strength Steel,” Master’s Thesis, The University of Texas at Austin, Austin, Texas, December 2014.

Sokoli, D., and Ghannoum, W. M., “High-Strength Reinforcement in Columns under High Shear Stresses,” ACI Structural Journal, V.113, No. 3, May-June. 2016, pp. 605-614.

Sozen, M. A.; Monteiro, P.; Moehle, J. P.; and Tang, H. T., “Effects of Cracking and Age on Stiffness of Reinforced Concrete Walls Resisting In-Plane Shear,” *Proceedings of the 4th Symposium on Current Issues Related to Nuclear Power Plant Structures, Equipment and Piping*, Orlando, FL, 1992.

Spacone, E., Filippou, F. C., and Taucer, F. F. ‘‘Fibre beamcolumn model for nonlinear analysis of R/C frames. I: Formulation,’’ *Earthquake Engrg. and Struct. Dyn.*, V. 25, No. 7, 1996, pp. 711–725.

Tavallali, H., Lepage, A., Rautenberg, J. M., Pujol, S., “Concrete beams reinforced with high-strength steel subjected to displacement reversals,” *ACI Structural Journal*, Vol. 111, No. 5, 2014, pp. 1037-1047.

Wight, J. K., *Reinforced Concrete Mechanics and Design 7th Edition*, Pearson Education, Inc, 2016.

Qi, X. and Moehle, J. P. “Displacement Design Approach for Reinforced Concrete Structures Subjected to Earthquakes,” Earthquake Engineering Research Center, University of California, Berkeley, CA, UCB/EERC-91/02, January 1991, 186 pp.

VITA

Albert Aquvannoa Limantono was born in Surabaya, Indonesia to Hadi Widjaja Limantono and Ayuda Soetopo. He graduated from Institut Teknologi Bandung in Bandung, Indonesia receiving his Bachelor in Civil Engineering in June, 2014. In August 2014, he started his Master of Science at The University of Texas at Austin. During these years, he worked as a Graduate Research Assistant at the Phil M. Ferguson Structural Engineering Laboratory, He received his Master of Science in Structural Engineering in August 2016. The author is the recipient of Indonesia Endowment Fund for Education Scholarship (LPDP PK-14).

Email address: albert_aqvan@yahoo.com or albert_aqvan@utexas.edu